THREE-DIMENSIONAL DESIGN AND ANALYSIS OF A COMPRESSOR ROTOR BLADE

A THESIS SUBMITTED TO
THE GRADUATE SCHOOL OF NATURAL AND APPLIED SCIENCES
OF
MIDDLE EAST TECHNICAL UNIVERSITY

BY

CUMHUR ÖZGÜR

IN PARTIAL FULFILLMENT OF THE REQUIREMENTS
FOR
THE DEGREE OF MASTER OF SCIENCE
IN
AEROSPACE ENGINEERING

JULY 2005

Approval of the Graduate School Natural and Applied Sciences

_____

Prof. Dr. Canan ÖZGEN
Director

I certify that this thesis satisfies all the requirements as a thesis for the degree of Master of Science.

_____

Prof. Dr. Nafiz ALEMDAROĞLU
Head of Department

This is to certify that we have read this thesis and that in our opinion it is fully adequate, in scope and quality, as a thesis for the degree of Master of Science.

_____	_____
Dr. A. Ruhşen ÇETE Co-Supervisor	Prof. Dr. İ. Sinan AKMANDOR Supervisor

Examining Committee Members

Prof. Dr. M. Cevdet ÇELENLİGİL	(METU,AEE)	_____
Prof. Dr. İ. Sinan AKMANDOR	(METU,AEE)	_____
Prof. Dr. İsmail Hakkı TUNCER	(METU,AEE)	_____
Prof. Dr. Ünver KAYNAK	(ETU,ME)	_____
Dr. A. Ruhşen ÇETE	(TAI)	_____

I hereby declare that all information in this document has been obtained and presented in accordance with academic rules and ethical conduct. I also declare that, as required by these rules and conduct, I have fully cited and referenced all material and results that are not original to this work.

Name, Last name: Cumhur ÖZGÜR

Signature :

ABSTRACT

THREE-DIMENSIONAL DESIGN AND ANALYSIS OF A COMPRESSOR ROTOR BLADE

Özgür, Cumhur

M. Sc., Department of Aerospace Engineering

Supervisor: Prof. Dr. İ. Sinan AKMANDOR

Co-Supervisor: Dr. A. Ruhşen ÇETE

July 2005, 135 pages

Three-dimensional design and three-dimensional CFD analysis of a compressor rotor stage are performed. The design methodology followed is based on a mean line analysis and a radial equilibrium phase. The radial equilibrium is established at a selected number of radii. NACA 65 series airfoils are selected and stacked according to the experimental data available. The CFD methodology applied is based on a three-dimensional, finite difference, compressible flow Euler solver that includes the source

terms belonging to rotational motion. The accuracy of the solver is shown by making use of two different test cases. The CFD solution of the designed geometry predicts the static pressure rises and flow turning angles to a good degree of accuracy.

Keywords: Compressor Rotor Blade Design, 3D Euler Solver, Source Terms Due to Rotational Motion, Radial Equilibrium.

ÖZ

KOMPRESÖR ROTOR PALESİNİN ÜÇ BOYUTLU TASARIMI VE ANALİZİ

Özgür, Cumhur

Yüksek Lisans, Havacılık ve Uzay Mühendisliği Bölümü

Tez Yöneticisi: Prof. Dr. İ. Sinan AKMANDOR

Ortak Tez Yöneticisi: Dr. A. Ruhşen ÇETE

Temmuz 2005, 135 sayfa

Bir kompresör rotor palesinin üç-boyutlu dizaynı ve dizayn edilen bu palenin üç-boyutlu HAM (Hesaplamalı Akışkanlar Mekaniği) analizi gerçekleştirilmiştir. Dizayn metodu, ortalama çizgi analizi ve radyal denge aşamalarından oluşmaktadır. Radyal denge, belirlenen beş yarıçapta uygulanmıştır. Bu yarıçaplarda NACA 65 serisi profiler seçilmiş ve daha sonra eldeki deneysel sonuçlara göre üst üste yığılmıştır. Uygulanan HAM metodu, üç-boyutlu, sonlu farklar yöntemi kullanan, sıkışabilir bir Euler çözücüsüne dayanmaktadır. Çözücü, dönme hareketine dayanan kaynak

terimlerini de içermektedir. Çözücünün hassasiyeti iki farklı deneme durumu ile sınanmıştır. Dizayn edilen geometriye ait HAM çözümü, statik basınç artışı ve akış dönme açılarının oldukça hassas şekilde hesaplanabildiğini göstermiştir.

Anahtar Kelimeler: Kompresör Rotor Pale Dizaynı, 3B Euler Çözücüsü, Dönme Hareketine Dayanan Kaynak Terimleri, Radyal Denge.

To My Parents

ACKNOWLEDGMENTS

I'd like to express my ultimate sincere appreciation to Prof. Dr. İ. Sinan Akmandor for his invaluable guidance, encouragement and generosity in sharing his experience throughout this research. He showed me the way not only in professional perspective but also in everyday life in many aspects.

The greatest thanks goes to my parents, Fatma and Muzaffer, who have always supported me in every step of my life. Also, I would like to thank to my dear love Müjde for her patience, love and friendship.

I would like to thank specially to Dr. A. Ruhşen Çete for his personal guidance, and teaching throughout this research. Also I like to express appreciation to friends and colleagues from TAI Flight Sciences Department for their invisible inevitable presence, support and patience.

Last, but not least my special thanks goes to Prof. Dr. M. Haluk Aksel for his non-obligatory but lifesaving support during one stage of this research.

TABLE OF CONTENTS

LIST OF TABLES

TABLES

LIST OF FIGURES

FIGURES

LIST OF SYMBOLS

SYMBOLS

$\vec{a}$	Acceleration Vector of the Fluid Element
C_L	Lift Coefficient
D	Diffusion Factor
dm	Mass of the Fluid Element
$d\vec{F}$	Resultant of All External Forces Applied on the Fluid Element
$d\vec{F}_{body}$	Net Body Force Acting on the Fluid Element
$d\vec{F}_{surface}$	Net Surface Force Acting on the Fluid Element
$d\vec{F}_{line}$	Net Line Force Acting on the Fluid Element
E	Matrix of Inviscid Fluxes in x Direction
e	Internal Energy of the Fluid Element
E_v	Matrix of Viscous Fluxes in x Direction
ΔE	Change in Total Energy of the Fluid Element
F	Matrix of Inviscid Fluxes in y Direction
F_v	Matrix of Viscous Fluxes in y Direction
G	Matrix of Inviscid Fluxes in z Direction
G_v	Matrix of Viscous Fluxes in z Direction
$\vec{g}$	Gravitational Acceleration Vector
gh	Potential Energy of the Fluid Element

H	Matrix of Source Terms
$\vec{i}$	Unit Vector in x Direction
$\vec{j}$	Unit Vector in y Direction
$\vec{k}$	Unit Vector in z Direction
P	Static Pressure
P_t	Total Pressure
Q	Matrix of Independent Variables
ΔQ	Heat Added to the Fluid Element
q	Net Heat Flux trough the Faces of the Fluid Element
$\dot{q}$	Heat Generated Inside the Fluid Element
R_n	Reaction Number, Degree of Reaction
r	Radius
$\vec{r}$	Position Vector of the Fluid Element
u	x Component of the Velocity Vector of the Fluid Element
V	Absolute Velocity
$\vec{V}$	Velocity Vector of the Fluid Element
v	y Component of the Velocity Vector of the Fluid Element
W	Relative Velocity
w	z Component of the Velocity Vector of the Fluid Element
ΔW	Work Done on the Fluid Element
x_l	x Coordinate of the NACA Airfoil Lower Surface
x_C	x Coordinate of the Center of the Fluid Element
x_u	x Coordinate of the NACA Airfoil Upper Surface

y_C	y Coordinate of the Center of the Fluid Element
y_c	y Coordinate of the NACA Airfoil Camber Line
y_u	y Coordinate of the NACA Airfoil Upper Surface
y_l	y Coordinate of the NACA Airfoil Lower Surface
y_t	y of the NACA Airfoil Thickness
z_C	z Coordinate of the Center of the Fluid Element
Ω	x Component of the Rotational Velocity Vector
α	Abslotue Flow Angle
β	Relative Flow Angle
ρ	Density of the Fluid Element
ϕ	Flow Coefficient
γ	Stagger (Setting) Angle
σ	Solidity
λ	First Viscosity Constant
μ	Second Viscosity Constant
τ	Stress
ω	Rotational Speed
$\bar{\omega}$	Total Pressure Loss Coefficient
$\vec{\omega}$	Rotational Velocity Vector
ψ	Loading Coefficient
$\vec{\nabla}$	Gradient Operator
$\times$	Curl Operator

SUBSCRIPTS

ax	Axial
θ	Tangential
0	Rotor Inlet
1	Rotor Exit

ABBREVIATIONS

CAD	Computer Aided Design
CFD	Computational Fluid Dynamics
IGV	Inlet Guide Vane
RPM	Revolution per Minute

CHAPTER 1

INTRODUCTION

In this chapter, the work done in the present study is summarized.

First, a motivation is given. Then the historical background of both the gas turbine engine and its design methodologies are given. Objectives of the present study are given at the end of this chapter.

1.1 Motivation

Gas turbine engine is one of the important technological achievements of 20^{th} century. It had many major contributions to human life as it is known today. Gas turbine has not only given the meaning to transportation, but also become one of the most important factors in both energy and defense industries.

In fact, gas turbine has solely evolved into an industry itself. Today, some of the largest companies in the world (i.e. General Electric, Rolls – Royce, Pratt & Whitney, Siemens, Kawasaki, etc.) are all in the gas turbine industry. These companies produce gas turbine engines which are used as power plants for power stations, large ships and strategically the most important ones, i.e. aircraft.

A gas turbine engine is a machine that produces mechanical energy that is a combination of different components. For most current designs these components are; a diffuser, a compressor (usually multi–stage), a combustion chamber, a turbine (usually multi–stage) and an exit nozzle. The components compressor and turbine are themselves combinations of

several rows of rotating and stationary blades. Each pair of one rotating and one succeeding stationary blade row is called a “stage”.

Design of a gas turbine engine consists of the aerodynamic, thermodynamic and structural design and integration of these different and relatively complex components.

Up to the end of 70’s, most of the design and optimization process relied on an empirical approach, which meant a very large number of tests. The all-experimental optimization strategy was very time and cost consuming for at least two reasons. Firstly, each iteration implied all the phases from design to manufacturing, instrumentation and testing needed to be reproduced. Secondly, determining the variables which had to be improved in the design required heavy instrumentation on each component, in order to identify the critical locations (Vuillez C. et al., 1994).

So, later CFD started to be used as the flow simulator at different levels. Analytical methods followed by potential solutions and then Quasi 3D methods. Today, it is possible to use full 3D CFD codes in turbomachinery design as in the present study.

1.2 Historical Background

1.2.1 Gas Turbine Engines

The basic development of the jet engine took place during the period of World War II, with parallel development being carried out by Whittle in England and von Ohain in Germany; because of wartime secrecy neither was aware of each other’s work. A Heinkel experimental aircraft powered by a von Ohain engine made the first flight of a jet-propelled aircraft on 27 August 1939. The Gloster-Whittle aircraft powered by a Whittle engine made its first flight on 15 May 1941. Since then mainly three companies dominated aircraft engine industry. These are Pratt & Whitney from Canada, Rolls-Royce from England and General Electric from United States.

In 1950's Pratt & Whitney developed the J57 engine. It proved to be a revolutionary advance in axial flow turbojet technology. J57 produced 10,000 pounds of thrust (i.e. 44.5 kN) and twice the fuel efficiency of the best German WWII engine. Using the J57 model, Pratt & Whitney incorporated more exotic high temperature materials to produce greater thrust. Later, Pratt & Whitney modified the J57 with a larger front-end compressor/fan leading to a high-efficiency low-bypass turbojet engine which is known as TF33. TF33 was able to generate 18000 pounds of thrust (i.e. 80.1 kN).

During the same period GE developed a successful version of the fanjet using the "aft fan" concept. In 1957 they produced CJ-805 and later in order to solve compressor stalls, GE made a revolutionary technology breakthrough. They developed the variable-geometry compressor stators. GE used this new technology to develop the J79 engine producing 17000 lbs of thrust (i.e. 75.6 kN) and leading the way for the modern very-high-bypass engine J85. Mach 2 flight was then possible.

In 1970's Pratt & Whitney's introduced F100 engine producing 23800 pounds of thrust (i.e. 105.9 kN) and powering initially F-15 and later F-16 aircraft.

During the same period GE developed F101 engine. It was designed to power the North American B-1 bomber and being a possible alternative to the Pratt & Whitney F100 engine.

In the early 1980's the United States Air Force and Navy formally began developing requirements for next generation fighter to replace F-15 and F-14. GE introduced the F110 engine as an alternate power source for F-16 aircraft. GE F110 was to produce 28600 pounds of thrust (later, in 1990's the engine performance is increased and the thrust level was raised to 29700 pounds, i.e. 132.1 kN). Navy procured the F/A-18E/F aircraft powered by the GE F414, a derivative of the F404. Air Force pursued the Advance Tactical Fighter. Program matured into the Lockheed Martin F/A-22

powered by the Pratt & Whitney F119 engine. Focus for the F119 was to improve technology for supersonic cruise and stealthy turbojets. P&W F119 engine was to produce 22000 pounds of thrust (i.e. 97.9 kN).

Also in the early 1980's, the Department of Defense issued the request for proposals for the new Cargo Aircraft Program. Boeing, Lockheed, and McDonnell Douglas submitted proposals. McDonnell Douglas Corporation, (now Boeing) was announced as the winner of the competition in August 1981. Pratt & Whitney was selected to provide the F117-PW-100 turbofan engines. This engine had a maximum thrust level of 41700 pounds (i.e. 185.5 kN). The commercial PW2040 series is currently used on the Boeing 757 producing 40440 pounds of thrust (i.e. 179.8 kN).

1.2.2 Gas Turbine Engine Design Methodologies

Preliminary design methods tend to be based on elementary one-dimensional mean-line methods of analysis. These are able to predict the performance of a turbomachine from basic design information to an accuracy of a few percent. They are thus sufficiently accurate to allow the main geometric and aerodynamic parameters to be selected before a refined design is attempted.

However since the early days of turbomachinery, designers were always interested in simulating or guessing the flowfield through the blade passages of any designed engine.

First solid work in understanding the flowfield through the blade passages came as early as 1952. C. H. Wu recognized the truly three-dimensional nature of the flow in his classic paper (Wu C. H., 1952) and proposed the remarkably sophisticated computational scheme illustrated in Figure 1. The fully three-dimensional flow was treated by the superposition of a number of two-dimensional flows, located on the so-called .S-1 and S-2 stream surfaces. S-2 surfaces follow the primary fluid deflection caused by the blade profile curvature and its associated aerodynamic loading. Due to

the variation of static pressure between the convex surface of blade No. 1 and the concave surface of the blade No. 2 the curvature of each S-2 stream surface will differ, calling for the introduction of several surfaces for adequate modeling. The S-1 surfaces are allowed to twist to accommodate the fluid movements caused by the variations of S-2 surfaces. The S-1 and S-2 surfaces in fact represent a selection of the true stream surfaces passing true the blade row. By solving the equations of motion for the fluid flows on these surfaces, successively improved estimates of the S-1 and S-2 surfaces may be obtained, allowing also for the fluid dynamic coupling between them. An iterative approach to achieve a good estimate of the fully three-dimensional flow was fairly comprehensively laid out by Wu in 1952. Usually the flow in any S-2 plane is called *"through*-flow" and the one in the S-1 plane is called *"blade-to-blade"* flow in the literature since then (Lewis R. I., 1996).

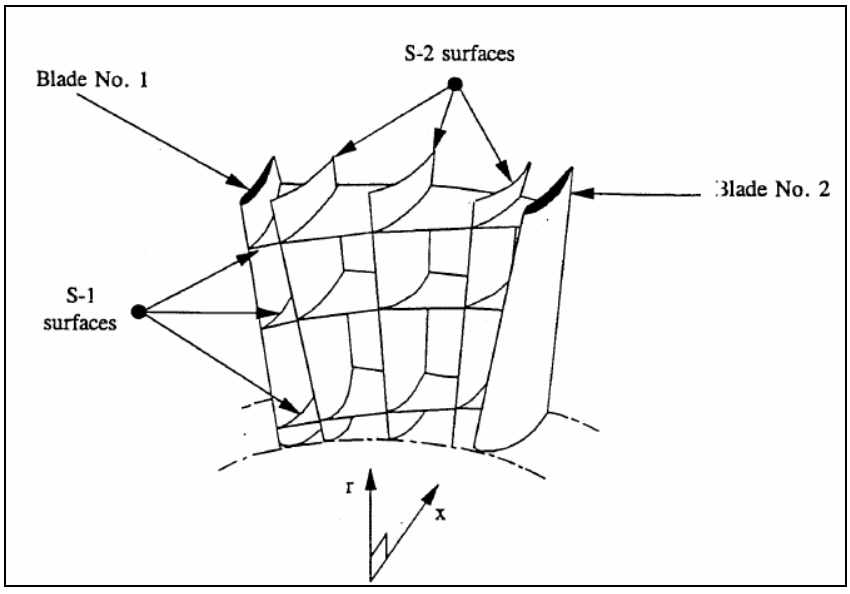

Figure 1 Wu's description of the flowfield

This kind of assumption of the true three-dimensional flow as being the superposition of two two-dimensional flows is known as "*Quasi Three-Dimensional"* (or Q3D) approach and has been widely used in turbomachinery area after the work of Wu.

"Streamline Curvature Method" (Novak R. A., 1967) was successfully used on S-1 and S-2 surfaces of Wu. The streamline curvature method become instrumental in the development of through-flow codes. (Smith L. H., 1966) developed the performance prediction capability using through-flow analysis code. Later finite difference solutions of through-flow model were reported by (Davis W. R., Millar D. A. J., 1975), (Smith D. J. L.,1974) and (Bosman C. et al. ,1977). Finite element methods applied during 70's by (Hirsh Ch., Warzee G., 1979). The above listed codes used through-flow solutions and a number of correlation factors to simulate real flow effects. Solution of Euler equations was initially performed in two dimensions by (McDonald P.,1971).

Later, Euler/boundary layer coupled flow analysis methodology of (Giles M. B., Drela M., 1987) is successfully applied to blade-to-blade flows by (Uzol O., 1995), (Ekici K., 1997).

With the increase of computing power, full three-dimensional Euler solutions in the blade passages was computed by (Denton J. D., 1982), (Holmes D.G., 1989). Later full three-dimensional Navier-Stokes solutions are computed and used as a design tool by (Denton J.D., 1990).

1.3 Objectives of the Present Study

The present study focuses mainly two major objectives:

i. Designing a compressor rotor stage.

ii. 3D CFD analysis of the designed rotor geometry.

The first objective is achieved by following mostly the method described in (Wilson D. G., 1984). It starts with a mean line analysis,

continuing with radial equilibrium and hence obtaining the famous "*velocity triangles*" at selected number of radial sections.

Next, is the selection of the appropriate airfoils for the velocity triangles obtained in the previous step. At this point (Horlock J. H., 1958) is followed. NACA 65 series airfoils were used because of the availability of the information regarding them.

Next is the determination of the characteristics (like static pressure rise, total pressure loss, etc.) of the airfoils selected in the previous step. This is done using the above mentioned widespread data. At this point (Emery J. C. et al., 1958), (Lieblein S. et al., 1953) and (Cumpsty N. A., 1989) are followed.

The first objective is completed by 3D geometry generation using a CAD software.

The second objective needed a 3D CFD code first of all. To do that an existing, validated, external flow solver was modified (namely TAINS). The modification process is started by deriving the equations of motion suitable for the rotational motion in the relative frame of reference of the rotor. At this point (Çıray C., 2000), (Batchelor G. K., 1967), (Aksel M. H., 2003) and (Grietzer E. M. et al., 2004) are followed.

After insertion of the rotational terms derived in the previous step, the solver was transformed into an internal flow solver by making use of periodic boundary condition (which was an existing capability of the code) and by generating a characteristic based outflow boundary condition. At this point (Hirsch Ch., 1990) is followed.

By the completion of the previous step, the solver was ready. The next step was the validation of the newly generated code. This is done by making use of a structured grid generation program.

The second objective is completed by generating a number of 3D structured grids around the geometry created with the CAD geometry

before. Each grid had a different size and all were solved using the solver generated. All solutions converged. The results are compared and the one corresponding to the finest grid is presented.

Through the achievement of the second objective, general directions given by (Denton J. D., 1994) and (Holmes D.G., 1989) were followed extensively.

CHAPTER 2

DESIGN METHODOLOGY

2.1 Introduction

In this chapter the design objectives and methodology are explained. Results are tabulated and a flowchart is included.

2.2 Design Objectives

The objective of the present study is to design a 1st or 2nd stage compressor rotor blade having:

- An outer diameter of 38 cm and an inner diameter of 22 cm;
- Rotational speed of 14000 RPM;
- Total pressure ratio of 1.25 and flow turning of 23° at the mean radius.

2.3 Design Method

The design of a compressor rotor can be given briefly as follows:

i. Determining the inlet and exit velocity vectors and their orientation at one radial location (namely “the mean radius”).

ii. Determining the inlet and exit velocity vectors and their orientation at other radial locations starting from mean line and using radial equilibrium concept.

iii. Choosing appropriate cascade airfoils after having calculated all the velocities and flow turning angles at all radial locations.

iv. Determining the appropriate stagger angle in order to place the airfoils suitably.

v. Estimating the static pressure rise of the airfoils at each radial location using experimental data regarding the cascade airfoils.

vi. Estimating the total pressure rise at each radial location once the velocity vectors are known.

vii. Estimating the total pressure loss at each radial location using experimental correlations.

viii. Creating the 3D geometry.

ix. Simulating the flow field using CFD methodology.

The details of each step are given in the following sections.

2.4 Mean Radius

The aim of this section is to evaluate the inlet and exit absolute and relative velocities at the mean radius. Mean radius is usually the geometric mean of hub and tip radii. In the present study dimensions like hub and tip diameters are chosen to be similar to an already existing engine.

Velocities are determined as follows: Inlet absolute velocity (both axial $V_{ax,0}$ and tangential $V_{\theta,0}$ components) and direction is specified. Also the rotational speed ωr is specified. Hence absolute and relative velocities at the inlet can be found using:

$$V_0 = \sqrt{{V_{ax,0}}^2 + {V_{\theta,0}}^2}$$

$$W_0 = \sqrt{{V_{ax,0}}^2 + (\omega r - V_{\theta,0})^2} \qquad (2\text{-}1)$$

Also the absolute and relative flow angles can be found using:

$$\alpha_0 = \tan^{-1}\left(\frac{V_{ax,0}}{V_{\theta,0}}\right)$$
$$\beta_0 = \tan^{-1}\left(\frac{V_{ax,0}}{\omega r - V_{\theta,0}}\right) \quad (2\text{-}2)$$

Having determined the absolute and relative velocity vectors and flow angles, the inlet condition at the mean radius is fixed.

The next step is to evaluate the velocities and angles at the exit. The exit is related to the inlet by the use of "*Reaction Number*". The definition of Reaction Number is the ratio of the change in static enthalpy in the rotor to the total enthalpy rise in the rotor and is given by (Wilson D. G., 1984):

$$R_n = 1 - \frac{V_{\theta,0} + V_{\theta,1}}{2\omega r} \quad (2\text{-}3)$$

This definition is used at all radial locations as the choice of reaction number variation along the blade span is an important factor in compressor/turbine design.

Once the reaction number (R_n), inlet tangential velocity ($V_{\theta,0}$) and rotational velocity (ωr) are known one can find exit tangential velocity ($V_{\theta,1}$). Also by knowing the exit axial velocity ($V_{ax,1}$) one can determine all vectors and angles in and out of the rotor.

It'll be apparent in the following section that the exit axial and tangential velocities will be related to the ones at inlet by the use of radial equilibrium at other radial locations. At the mean radius, exit axial velocity ($V_{ax,1}$) is taken to be the same as the inlet. This is because the mean line is the input of the whole design procedure.

The velocity vectors at the inlet and exit are called "velocity triangles" altogether. An example velocity triangle is given in Figure 2 below.

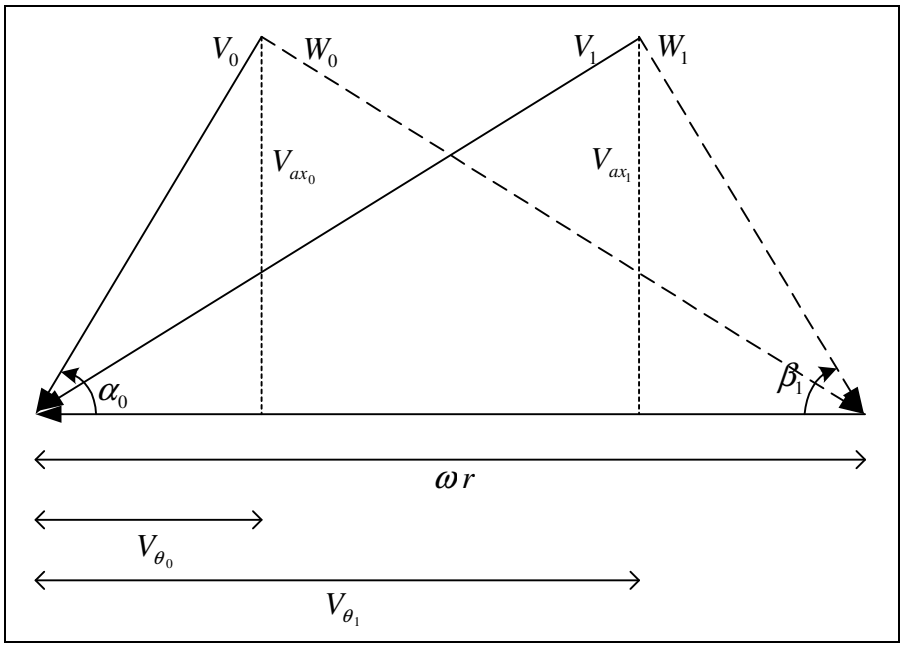

Figure 2 Velocity triangles with velocity and angle definitions

2.5 Other Radial Locations – Radial Equilibrium

The aim of this section is to obtain velocity triangles at radial locations other than the mean radius.

For axial flow compressors the flow is fully three dimensional which requires the flow at the various sections to be compatible and to satisfy the momentum equation in the radial direction. In essence this means that the performance of the blades at a given spanwise position is not determined by that section alone but by the same blade at other spanwise positions, by the annulus shape and by the compressor as a whole. So, the velocity triangles at different radial locations must be related to the ones at mean line by making use of the laws of nature. Random choice of velocity triangles may result in unrealistic designs. It's important to design the blades so that at every radial location the geometry must be compatible with what the flow is constrained to do.

The physical mechanism for the flow to adjust itself in the radial direction in response to the constraints imposed by the blades is the need of the flow to approach radial equilibrium. When the fluid flowing through a duct or annulus has a tangential component of velocity, a pressure gradient with radius is naturally set up. So the velocity vectors at each radius are affected by other radial locations through the momentum equation in the radial direction. The relation of the radial variation of static pressure, the variation of tangential velocity, and the variation of axial velocity is sought.

This is done by making use of simple radial equilibrium equation. The equation is called “simple” because of the assumptions made during the derivation (Wilson D. G., 1984):

$$\frac{1}{r^2}\frac{d}{dr}\left(r^2 {V_\theta}^2\right)+\frac{d}{dr}{V_{ax}}^2=0 \qquad \text{(2-4)}$$

The assumptions made during the derivation of equation (2-4) are (Wilson D.G, 1984):

$\frac{d(Total\ Enthalpy)}{dr}=0$, $\frac{d\left(RadialVelocity^2\right)}{dr}=0$ and $\frac{d(Entropy)}{dr}=0$.

One can relate tangential and axial velocities using equation (2-4). Note the rV_θ term in the equation. When a tangential velocity distribution having rV_θ constant is substituted into equation (2-4), it gives a constant axial velocity along the span. This configuration is called a “free vortex design” because of the tangential velocity distribution is that of a free vortex. Free vortex designs were used extensively in the early years of turbomachinery. Many different tangential velocity distributions are possible. In the present study Carmichael – Lewis tangential velocity distribution is used (Wilson D. G., 1984):

$$V_{\theta,0} = a(r)^n - \frac{b}{r}$$

$$V_{\theta,1} = a(r)^n + \frac{b}{r} \qquad (2\text{-}5)$$

Where a, b and n are constants to be determined below. Equation (2-5) is substituted into equation (2-4) and variation of axial velocity in radial direction is obtained.

In (Wilson D. G., 1984) this is done after non-dimentionalisation of the variables by mean line values as follows:

$$V'_\theta = \frac{V_\theta}{\omega r_{mean}},\ V'_{ax} = \frac{V_{ax}}{\omega r_{mean}} \text{ and } r' = \frac{r}{r_{mean}}$$

By doing this transformation simple radial equilibrium equation (2-4) becomes:

$$\frac{1}{(r')^2}\frac{d}{dr'}\left[(r')^2(V'_\theta)^2\right] + \frac{d}{dr'}\left[(V'_{ax})^2\right] = 0 \qquad (2\text{-}6)$$

Also transforming the aforementioned Carmichael – Lewis tangential velocity distribution, equation (2-5) becomes:

$$V'_{\theta,0} = a'(r')^n - \frac{b'}{r'}$$

$$V'_{\theta,1} = a'(r')^n + \frac{b'}{r'} \qquad (2\text{-}7)$$

Similarly the definition of reaction number equation (2-3) now becomes:

$$R'_n = 1 - \frac{1}{2r}\left(V'_{\theta,0} + V'_{\theta,1}\right) \qquad (2\text{-}8)$$

Substituting equation (2-7) into equation (2-6) and integrating yields (Wilson D. G., 1984):

$$\left(\frac{V_{ax,0}'}{\phi_m}\right)^2 = 1+\left(\frac{n+1}{n}\right)\left[\frac{1-R_{n,m}'}{\phi_m}\right]\left\{\left[1-(r')^{2n}\right]+\left(\frac{n}{n-1}\right)\left[\frac{\psi_m}{1-R_{n,m}'}\right]\left[1-(r')^{n-1}\right]\right\}$$

$$\left(\frac{V_{ax,1}'}{\phi_m}\right)^2 = 1+\left(\frac{n+1}{n}\right)\left[\frac{1-R_{n,m}'}{\phi_m}\right]\left\{\left[1-(r')^{2n}\right]-\left(\frac{n}{n-1}\right)\left[\frac{\psi_m}{1-R_{n,m}'}\right]\left[1-(r')^{n-1}\right]\right\} \quad (2\text{-}9)$$

In equation (2-9), subscript “m” stands for mean radius, ϕ and ψ are two other important variables. They are called “flow coefficient” and “loading coefficient” respectively. It is possible to represent velocity triangles by making use of flow coefficient, loading coefficient together with reaction number. The definitions of flow coefficient and loading coefficient are given below:

$$\phi = \frac{V_{ax}}{\omega r}$$

$$\psi = -\frac{\left(V_{\theta,1}-V_{\theta,0}\right)}{\omega r} \quad (2\text{-}10)$$

The flow coefficient ϕ is the ratio of axial velocity to rotational velocity. Usually axial velocity changes from inlet to exit of any stage so does the flow coefficient.

The loading coefficient ψ is positive for turbines, negative for compressors. A “highly” loaded compressor stage would have a loading coefficient of -0.5 and below, whereas a “lowly” loaded one would have a loading coefficient of -0.3 and above. These judgments of “high” and “low” are relative, and apply best to a stage of high hub to tip ratio. Stages with low hub to tip ratio (as in the present case), normally have very high loadings at the hub and light loadings at the tip.

Substituting the flow coefficient, loading coefficient and reaction number at mean radius into equation (2-9), axial velocities in and out of the stage ($V_{ax,0}$ and $V_{ax,1}$) at any radius can be found. Also tangential velocities

($V_{\theta,0}$ and $V_{\theta,1}$) can be found using equation (2-7). So the velocity triangles can be found this way at each radius.

Given below is the result of such a calculation. The velocity triangles are given in Figure 3 and the quantitative values of these triangles are given in Table 1 below. See Appendix A for detailed example calculations.

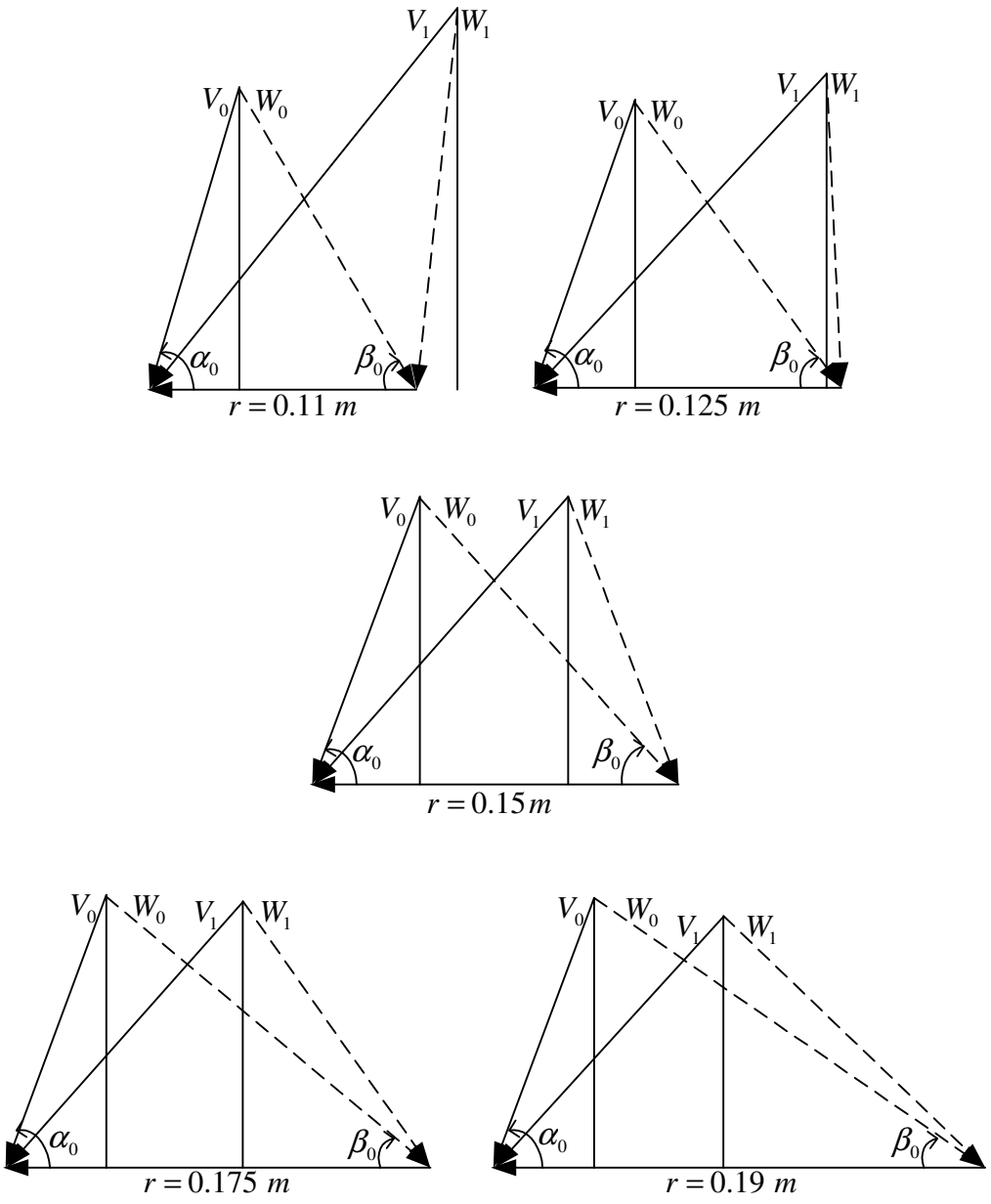

Figure 3 Velocity triangles at 5 radial locations after radial equilibrium

Table 1 Velocity components and angles at five radial locations after radial equilibrium

r(m)	$V_{ax,0}$ (m/s)	$V_{\theta,0}$ (m/s)	V_0 (m/s)	W_0 (m/s)	α_0	β_0
0.11	182.00	55.38	190.24	210.51	73.07	59.83
0.125	176.66	60.91	186.87	214.90	70.98	55.29
0.15	170	61.87	180.91	232.11	70	47.09
0.175	164.33	62.17	175.70	254.55	69.28	40.21
0.19	161.71	61.60	173.05	270.59	69.15	36.70
r(m)	$V_{ax,1}$ (m/s)	$V_{\theta,1}$ (m/s)	V_1 (m/s)	W_1 (m/s)	α_1	β_1
0.11	205.12	186.52	277.25	206.68	47.72	97.04
0.125	187.58	176.31	257.43	187.71	46.77	87.88
0.15	170	158.04	232.11	180.91	47.09	70
0.175	155.83	144.6	212.58	191.88	47.14	54.30
0.19	149.48	137.52	203.12	205.51	47.38	46.67

2.6 Cascade Airfoil Selection

It is possible to specify the blades of an axial compressor in many different ways. The traditional way is to base the design on existing families of profiles such as, NACA 65-series or double-circular-arc (DCA) series. The former is best suitable for subsonic applications while the later is for transonic applications (Song B., 2003).

In the present study NACA 65 series airfoils with 10% thickness are used. The reasons why NACA 65 series airfoils are chosen are because they are designed especially for turbomachinery applications and they are well documented.

The profile is obtained by adding a thickness distribution on top of a so-called *camber line*. The details of airfoil profile generation process are given below.

To choose appropriate airfoil at any radius so as to achieve:

i. Flow turning by an amount suitable with the velocity triangles.

ii. A suitable setting angle which will be used in both 3D geometry generation and static pressure rise calculations.

As stated above, NACA 65 series airfoils are subject to numerous experiments, hence the performance characteristics are available in many forms. One of them is so-called “NACA Mellor Charts” (Horlock J. H., 1958). NACA Mellor Charts are plots which give the desired setting angle when inlet and exit flow angles are specified for 65 series airfoils. See Figure 4 for an example NACA Mellor Chart.

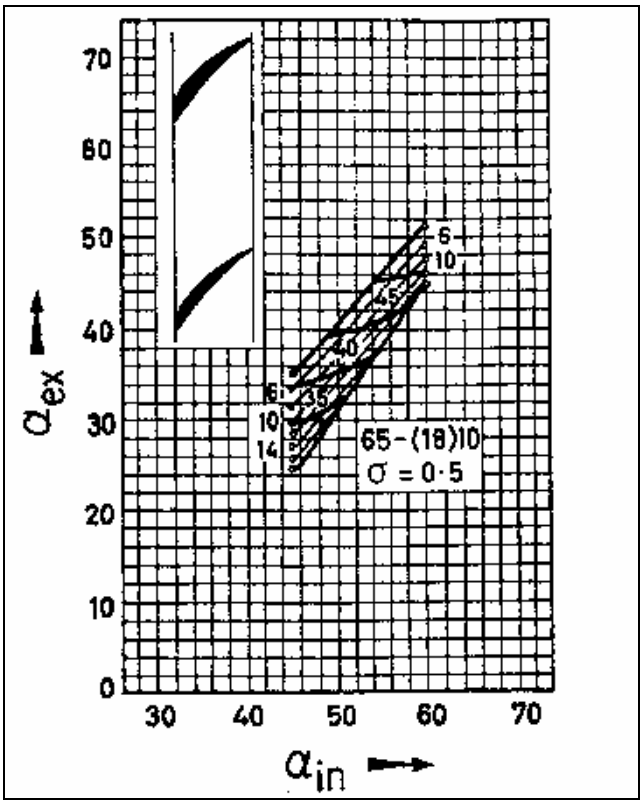

Figure 4 Example NACA Mellor Chart for NACA 65-(18)10 airfoil

To use NACA Mellor charts the necessary inputs are:

i. Inlet flow angle α_0 (measured from axial direction).

ii. Exit flow angle α_1 (measured from axial direction).

iii. Solidity ($\sigma = \frac{spacing}{chord}$)

Once these are known, one can enter into NACA Mellor Charts to find appropriate setting and incidence angles. The use of NACA Mellor Charts is illustrated in Figure 5:

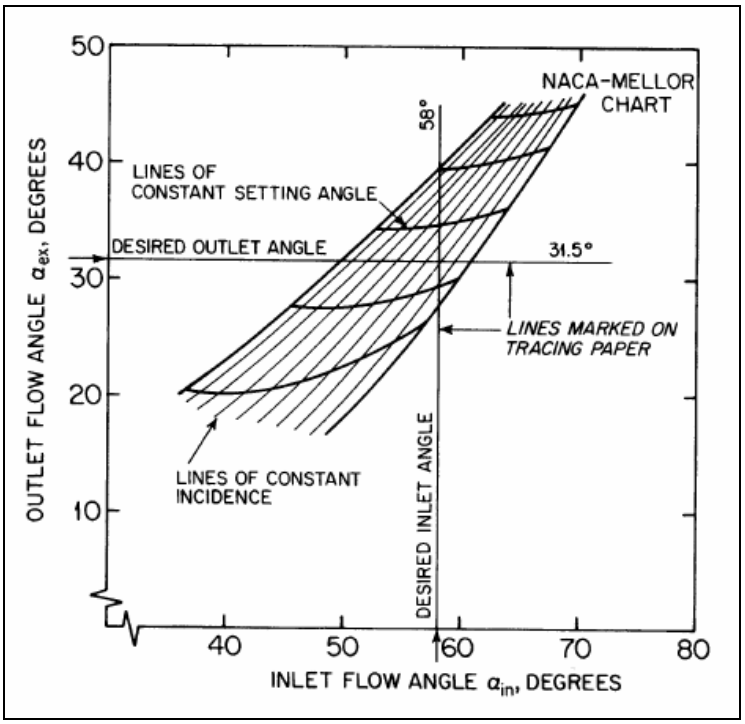

Figure 5 Illustration of the use of NACA Mellor Charts

All inlet and exit flow angles are provided in Table 1. However one has to be careful because in the velocity triangles given above, all *angles are measured from tangential direction*.

Another important point to consider is that, the inlet and exit angles are β_0 and β_1 (i.e. relative flow angles) respectively for ROTOR geometries. However they must be α_0 and α_1 (i.e. absolute flow angles) respectively for STATOR geometries.

Taking these into consideration, NACA Mellor charts are used and airfoil cascades are selected among suitable ones.

The results of such a selection procedure are given in Table 2 below. In these results, γ represents setting angle measured from tangential direction. So at the end, these must be converted to the present notation in which all the angles are measured from the tangential direction.

Table 2 Airfoil selection at five radial locations.

r(m)	Airfoil	Angle of Attack	Setting Angle (γ)	Δβ
0.11	NACA 65 – (18)10	21°	80.81°	37.21°
0.125	NACA 65 – (15)10	20°	75.29°	32.58°
0.15	NACA 65 – (15)10	13°	62.09°	22.91°
0.175	NACA 65 – (12)10	8°	54.21°	14.09°
0.19	NACA 65 – 810	6°	50.70°	9.97°

2.7 Static Pressure Rises

The next step is to obtain the static pressure rise of the selected airfoils. To do that two-dimensional experimental investigation of NACA 65 Series airfoils is used (Emery J. C. et al., 1958).

In the experimental results, static pressure distributions are given for each of the chosen NACA airfoils for three different inlet flow angles (i.e: 30°, 45° and 60°) and for four different solidities (i.e: 0.75, 1.0, 1.25 and 1.5). In each diagram static pressure distributions are given at five different angles of attack. So, linear interpolations are needed.

In (Emery J. C. et al., 1958), detailed blade-performance data for all cascade combinations tested are presented in the form of surface pressure distributions. In order to obtain the pressure rise, one needs the following:

i. NACA 65 Series airfoil name

ii. Inlet flow angle α_0 (measured from axial direction).

iii. Solidity ($\sigma = \frac{spacing}{chord}$)

iv. Angle of attack.

After linear interpolations for inlet flow angle and solidity values, static pressure rises between rotor inlet and exit are found. This is nothing but reading the static pressure rise of the cascade airfoil at the specified inlet flow angle and solidity from the numerous charts given in (Emery J. C. et al., 1958).

Once the static pressures are known, total pressure rises are found using absolute velocities and the static pressure values found above. Given below are the results of such a static pressure rise calculation together with the resulting total pressure rises in Table 3:

Table 3 Static and total pressure rise calculations at five radial locations.

r(m)	P_0 (Pascal)	P_1 (Pascal)	P_1/P_0	$P_{t,0}$ (Pal)	$P_{t,1}$ (Pa)	$P_{t,1}/P_{t,0}$
0.11	101325	111315.645	1.0986	123492.143	160397.027	1.2898
0.125	101325	114395.925	1.1290	122713.743	154986.425	1.2630
0.15	101325	118165.215	1.1662	121371.162	151163.684	1.2455
0.175	101325	120363.968	1.1879	120233.175	148043.001	1.2313
0.19	101325	120181.583	1.1861	119667.110	145451.945	1.2155

2.8 Total Pressure Loss Calculations

In this section total pressure losses of the airfoils are estimated.

According to (Lieblein S. et al., 1953), total pressure losses of NACA 65 series airfoils are related to diffusion factor for various inlet angles. The relation is given in Figure 6. One can estimate the non-dimensional total pressure loss coefficient ($\overline{\omega}$) knowing the inlet flow angle (β_0), solidity (σ) and diffusion factor (D). The definitions of non-dimensional total pressure loss coefficient ($\overline{\omega}$) and diffusion factor (D) are as follows:

$$\overline{\omega} = \frac{\Delta P_{t\,loss}}{\frac{1}{2}\rho {W_0}^2} \tag{2-11}$$

Diffusion factor:

$$D = \left(1 - \frac{W_1}{W_0}\right) + \frac{W_{\theta,1} - W_{\theta,0}}{2\sigma W_0} \tag{2-12}$$

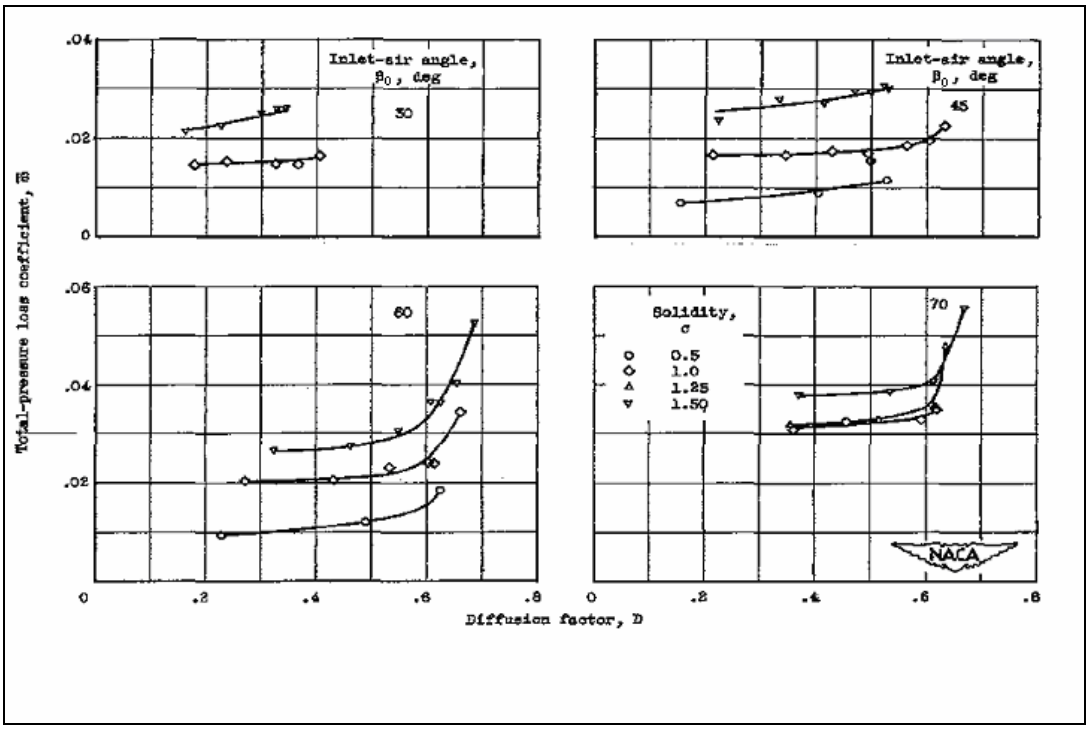

Figure 6 Total pressure loss coefficient vs. diffusion factor for NACA 65 Series.

The first term in equation (2-12) represents the diffusion due to one dimensional deceleration of the flow within the cascade diffuser while the second term represents the diffusion due to the flow turning around the cascade blade. According to (Cumpsty N.A., 1989), values of diffusion factor in excess of 0.6 are thought to indicate blade stall and a value of 0.45 would be a good design choice. The variables necessary to calculate the diffusion factors at five radial locations and the resulting diffusion factors are given in Table 4 below.

Using the diffusion factors (D) and solidities (σ) given in Table 4 and inlet flow angles given in Table 1, the non-dimensional total pressure loss coefficients ($\bar{\omega}$) and hence the total pressure loss at each radial location are found from Figure 6. The results are given in Table 5 below.

Table 4 Parameters required for loss calculations at five radial locations.

r(m)	W_1/W_0	ΔW_θ (m/s)	W_0 (m/s)	σ	D
0.11	0.9818	131.13	210.51	1.649	0.2078
0.125	0.8735	115.42	214.90	1.451	0.3121
0.15	0.7794	96.156	232.11	1.210	0.3922
0.175	0.7538	82.43	254.55	1.036	0.4023
0.19	0.7595	75.93	270.59	0.955	0.3879

Table 5 Total pressure losses.

r(m)	$P_{t,1}$ (ideal)	ϖ	$\Delta P_{t\,loss}$	$P_{t,1}$ (real)
0.11	160397.027	0.0244	662.2796	159734.7474
0.125	154986.425	0.0254	719.0420	154267.3838
0.15	151163.684	0.0221	726.2963	150437.3877
0.175	148043.001	0.0191	758.0287	147284.9723
0.19	145451.945	0.0189	849.8430	144602.1020

2.9 3D Geometry Generation

In the previous sections, suitable 65 series airfoil sections and the angles that the profiles to be set were chosen at each radius. As stated above, NACA 65 series cascade airfoils are well documented and much of these documents are freely available. See (Bogdonoff S. M., Bogdonoff H. E., 1945) for detailed information.

The profiles are generated adding a thickness distribution on top of a camber line. The designation of 65 series is best understood by an example: 65-(12)10. Here 65 designates the airfoil series; the number in the brackets is the design lift coefficient of the isolated airfoil at low Mach number expressed in tenths (i.e. C_L is 1.2 for this example); the final number is thickness to chord ratio in hundredths (i.e. t/c is 10% in this example). When the design lift coefficient is less then unity, the brackets may be omitted. Any desired airfoil may be obtained as follows:

Camber line and thickness distribution for design C_L = 1.0 is given in Table 6. The desired camber line is obtained by multiplying the ordinate and the slope of camber line of design C_L = 1.0 by the design C_L of the intended airfoil (i.e. 1.2 for the above example). Then using equation (2-13) the coordinates of the desired airfoil are obtained (Wallis R.A., 1983).

$$
\begin{aligned}
x_u &= x - y_t \sin\phi \\
y_u &= y_c + y_t \cos\phi \\
x_l &= x + y_t \sin\phi \\
y_l &= y_c - y_t \cos\phi \\
\phi &= \tan^{-1}\left(\frac{dy_c}{dx}\right)
\end{aligned}
\qquad \text{(2-13)}
$$

Here subscript "*u*" denotes *upper surface*, "*l*" denotes *lower surface*, "*c*" denotes *camber line* and "*t*" denotes *thickness*.

All necessary airfoils that are used in the design were obtained by the method described above. Some of the airfoils were already available in the literature. These were compared with the data obtained by the above procedure. One of the airfoils generated and its corresponding data in the literature are compared in Figure 7 below.

All airfoils used are given in Appendix B.

After having generated all necessary airfoils, the 3D geometry can now be created. This is sometimes called "*airfoil stacking*" in the literature. In the present study airfoil stacking is done using 3D Computer Aided Design (CAD) software. Each airfoil is put into the correct radius and the rotated around the quarter chord by an amount of the setting angle found above. Finally the blade geometry and the flow passage that will be used in the CFD analysis are obtained. The rotor stage and flow passage can be seen in Figure 8 and Figure 9 respectively below.

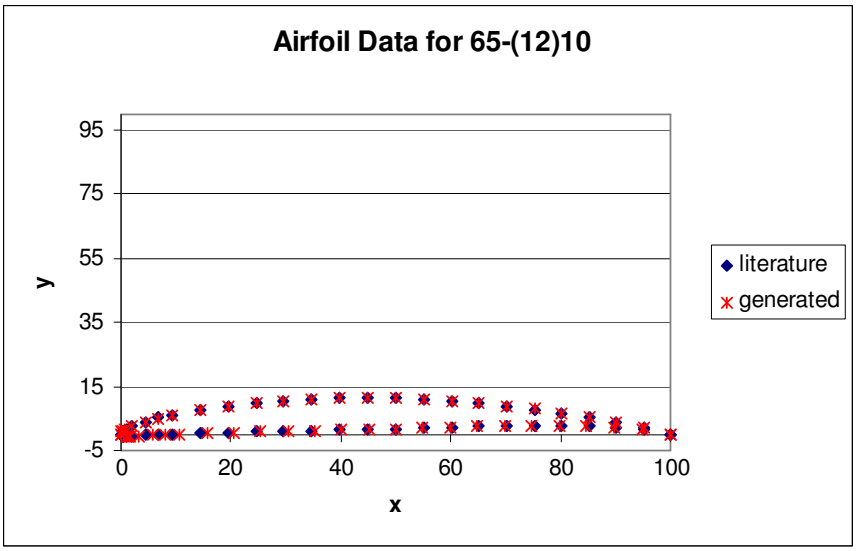

Figure 7 Airfoil data comparison for NACA 65-(12)10.

Table 6 NACA 65 Series airfoil data in percentage of chord for design C_L = 1.0

x	y_c	dy_c/dx	$\pm y_t$
0	0.000	–	0.000
0.5	0.250	0.42120	0.772
0.75	0.350	0.38875	0.932
1.25	0.535	0.34770	1.169
2.5	0.930	0.29155	1.574
5	1.580	0.23430	2.177
7.5	2.120	0.19995	2.647
10	2.585	0.17485	3.040
15	3.365	0.13805	3.666
20	3.980	0.11030	4.143
25	4.475	0.08745	4.503
30	4.860	0.06745	4.760
35	5.150	0.04925	4.924
40	5.355	0.03225	4.996
45	5.475	0.01595	4.963
50	5.515	0.00000	4.812
55	5.475	-0.01595	4.530
60	5.355	-0.03225	4.146
65	5.150	-0.04925	3.682
70	4.860	-0.06745	3.156
75	4.475	-0.08745	2.584
80	3.980	-0.11030	1.987
85	3.365	-0.13805	1.385
90	2.585	-0.17485	0.810
95	1.580	-0.23430	0.306
100	0.000	–	0.000

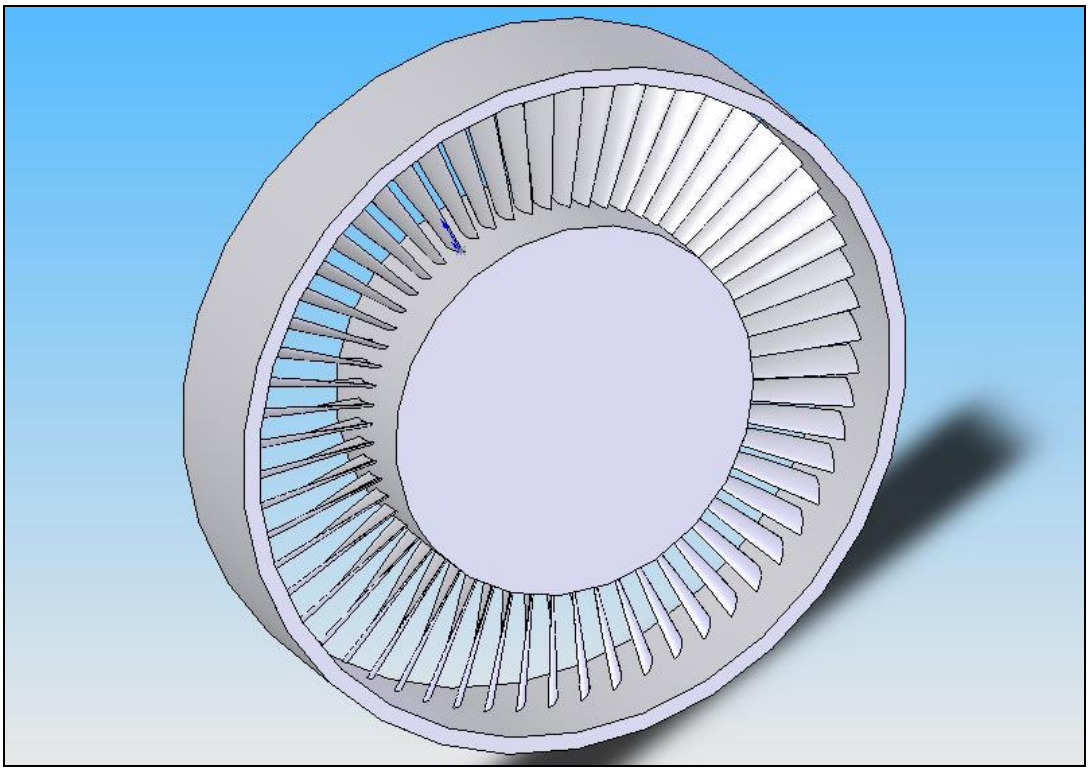

Figure 8 Overview of the designed rotor stage.

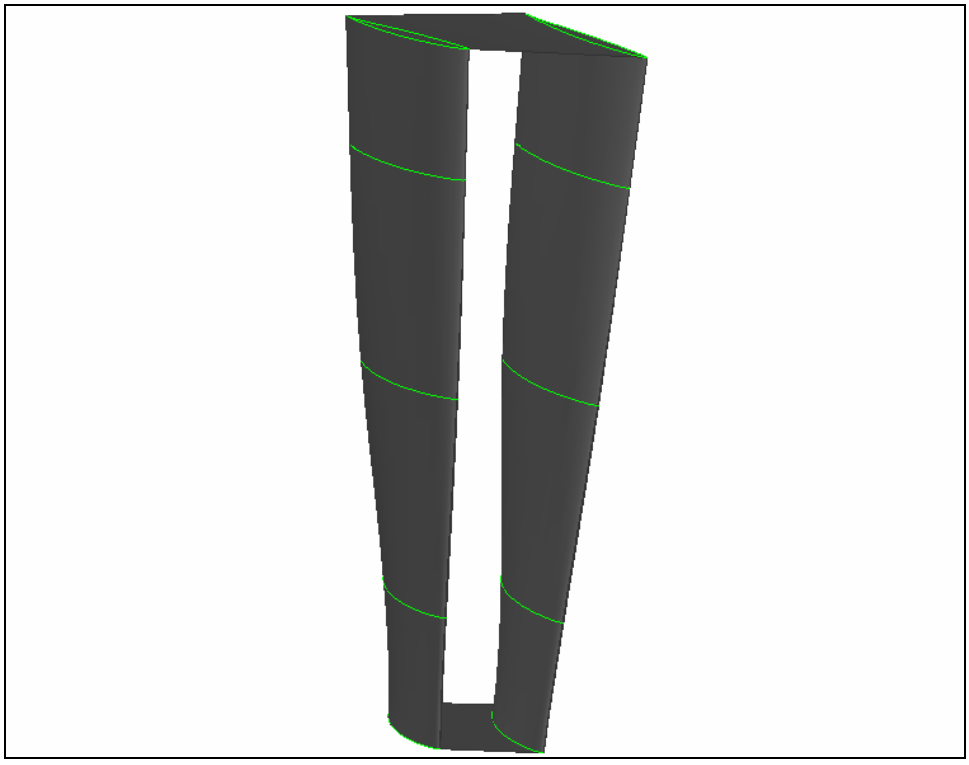

Figure 9 Flow passage that is going to be analyzed with CFD.

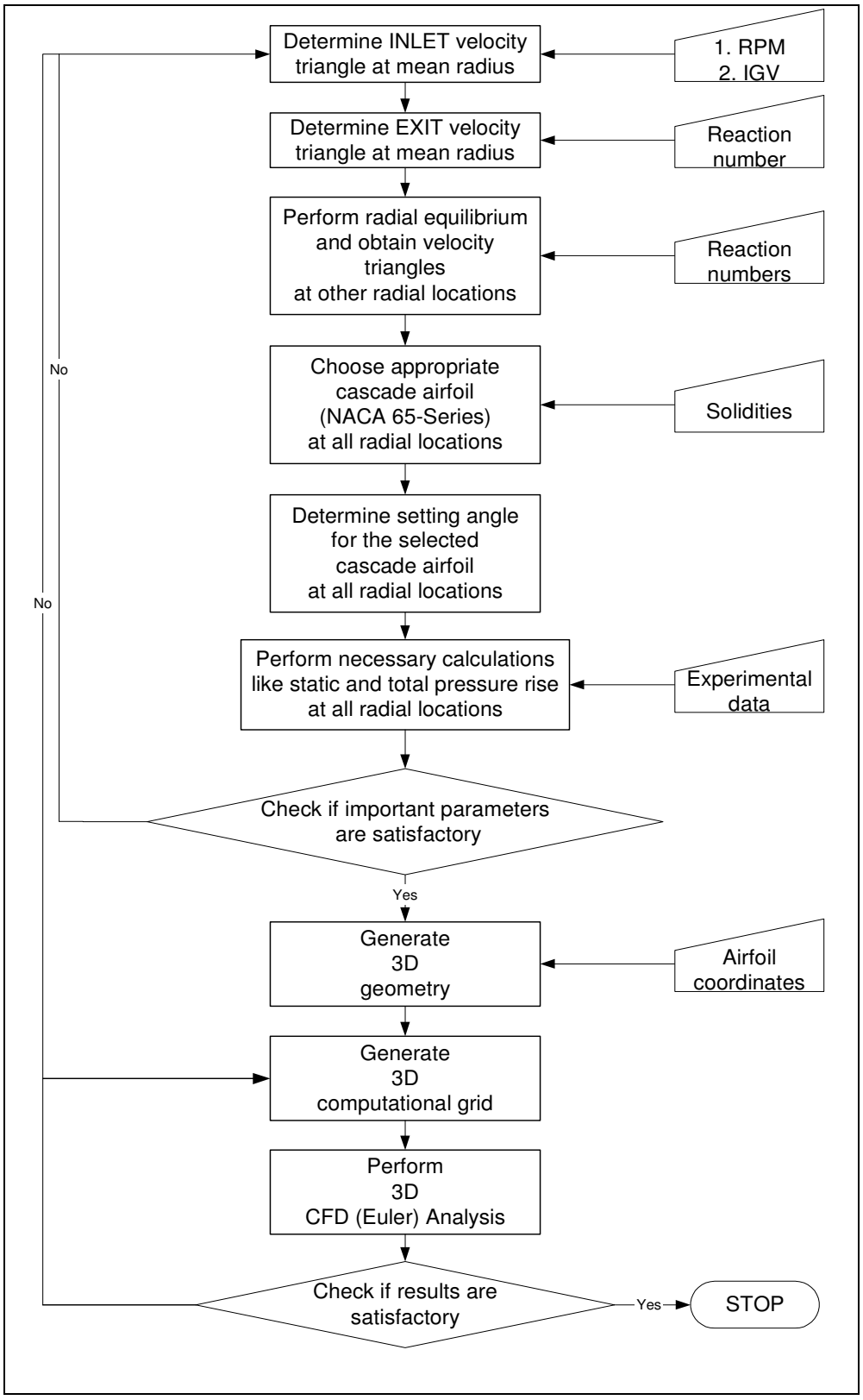

Figure 10 Flowchart of the design procedure.

CHAPTER 3

GOVERNING EQUATIONS

3.1 Introduction

In this chapter, the equations governing the fluid flow under rotational motion are derived. Following the derivation, general curvilinear coordinate transformation is explained.

3.2 Derivation of the Governing Equations

Fluid flow is governed by three basic laws. These are:

i. Conservation of Mass

ii. Conservation of Momentum – Newton's 2nd law

iii. Conservation of Energy

Rotation around a fixed axis creates centrifugal and Coriolis accelerations on the fluid element. These forces cannot be neglected and must be included in the momentum and energy equations. Conservation of mass is not affected by rotational motion and hence its derivation is not repeated here. One can find the derivation of conservation of mass in (Aksel H., 2003).

3.3 Conservation of Momentum – Newton's 2nd Law of Motion

Newton's second law of motion can in general be stated as follows:

$$\vec{F} = m\vec{a} \tag{3-1}$$

Here $\vec{F}$ is the resultant of all external forces that is acting on the fluid, m is the mass of fluid and $\vec{a}$ is the acceleration of the fluid.

Equation (3-1) is an expression given for the whole volume of fluid. The same equation can be written for an infinitesimal element of fluid as shown in Figure 11:

$$d\vec{F} = dm\,\vec{a} \tag{3-2}$$

Here $d\vec{F}$ is the net resultant force acting on the infinitesimal fluid element, dm is the mass of the infinitesimal fluid element and $\vec{a}$ is the acceleration of the infinitesimal fluid element. The aforementioned infinitesimal fluid element is shown in Figure 11 below. The mass of the element (dm) is equal to ρdxdydz where ρ being the density of the fluid.

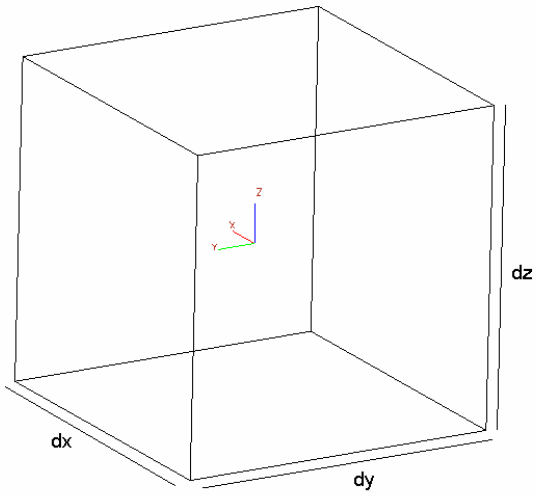

Figure 11 Infinitesimal fluid element

The external forces acting on the fluid element ($d\vec{F}$) can be stated as follows (Çıray C., 2000):

$$d\vec{F} = d\vec{F}_{body} + d\vec{F}_{surface} + d\vec{F}_{line} \tag{3-3}$$

Here $d\vec{F}_{body}$ is the net body force consisting of gravitational, centrifugal and Coriolis forces; $d\vec{F}_{surface}$ is the net surface force consisting of pressure and skin friction forces and finally $d\vec{F}_{line}$ is the net line force like cohesion force seen in capillary tubes. Gravitational and line force may be neglected for problems having air as the fluid.

The body and surface forces are investigated in detail below.

3.3.1 Body Forces

The aforementioned body forces can be written in more detail as follows:

$$d\vec{F}_{body} = d\vec{F}_{gravitational} + d\vec{F}_{centrifgal} + d\vec{F}_{Coriolis} \tag{3-4}$$

Equation (3-4) is written for an element as given in Figure 11. These forces are inertial forces and they to the center of the fluid element. Dividing both sides of equation (3-4) to the mass of the fluid element (dm), body "accelerations" are obtained.

$$d\vec{f}_{body} = d\vec{f}_{gravitational} + d\vec{f}_{centrifugal} + d\vec{f}_{Coriolis} \tag{3-5}$$

The gravitational, centrifugal and Coriolis accelerations given in equation (3-5) are stated as follows (Batchelor G.K., 1967):

$$d\vec{f}_{body} = \vec{g} - 2\vec{\omega}\times\vec{V} - \vec{\omega}\times(\vec{\omega}\times\vec{r}) \tag{3-6}$$

Here $\vec{g}$ is the gravitational acceleration, $-2\vec{\omega}\times\vec{V}$ is the Coriolis acceleration and $-\vec{\omega}\times(\vec{\omega}\times\vec{r})$ is the centrifugal acceleration where $\vec{\omega}$ is the rotational speed in vectorial form, $\vec{V}$ is the velocity vector and $\vec{r}$ is the position vector between the rotation axis and the center of the element. The general vectorial expressions for the Coriolis and centrifugal accelerations given above are investigated in more detail below:

3.3.2 Centrifugal Acceleration

The centrifugal acceleration $-\vec{\omega}\times(\vec{\omega}\times\vec{r})$, given in equation (3-6) is in vectorial form and will be expanded in this section. As stated above, $\vec{\omega}$ is the rotational velocity of the system and $\vec{r}$ is the position vector between the rotation axis and the center of the element. Decomposing both rotational velocity ($\vec{\omega}$) and position ($\vec{r}$) vectors into x, y and z components:

$$\vec{\omega}=\Omega\vec{i}$$
$$\vec{r}=(x-x_c)\vec{i}+(y-y_c)\vec{j}+(z-z_c)\vec{k} \qquad (3\text{-}7)$$

In equation (3-7), $\vec{i},\vec{j}$ and $\vec{k}$ are the unit vectors in x, y and z directions respectively; Ω is the x component of the rotational velocity; x_c, y_c and z_c are the coordinates of the axis of rotation and x, y and z are the coordinates of the center of the element. In the present turbomachinery problem the rotational axis is coincident with the machine axis and the rotational velocity vector is in $+\vec{i}$ direction.

First expanding the $(\vec{\omega}\times\vec{r})$ in equation (3-7):

$$\vec{\omega}\times\vec{r}=\begin{vmatrix}\vec{i} & \vec{j} & \vec{k}\\ \Omega & 0 & 0\\ (x-x_c) & (y-y_c) & (z-z_c)\end{vmatrix} \qquad (3\text{-}8)$$

$$\vec{\omega}\times\vec{r}=0\vec{i}-\Omega(z-z_c)\vec{j}+\Omega(y-y_c)\vec{k}$$

Similarly expanding $-\vec{\omega}\times(\vec{\omega}\times\vec{r})$ term in equation (3-7) using the expression equation (3-8), the centrifugal acceleration can be found to be:

$$-\vec{\omega}\times(\vec{\omega}\times\vec{r}) = -\begin{vmatrix} \vec{i} & \vec{j} & \vec{k} \\ \Omega & 0 & 0 \\ 0 & -\Omega(z-z_c) & \Omega(y-y_c) \end{vmatrix}$$

$$-\vec{\omega}\times(\vec{\omega}\times\vec{r}) = -\left[0\vec{i} - \Omega^2(y-y_c)\vec{j} - \Omega^2(z-z_c)\vec{k}\right] \tag{3-9}$$

$$d\vec{f}_{centrifugal} = 0\vec{i} + \Omega^2(y-y_c)\vec{j} + \Omega^2(z-z_c)\vec{k}$$

3.3.3 Coriolis Acceleration

The Coriolis acceleration ($-2\vec{\omega}\times\vec{V}$), given in equation (3-6) is in vectorial form and will be expanded in this section. As stated above, $\vec{\omega}$ is the rotational velocity of the system and $\vec{V}$ is the velocity vector of the element. Decomposing both rotational velocity ($\vec{\omega}$) and velocity ($\vec{V}$) vectors into x, y and z components:

$$\vec{\omega} = \Omega\vec{i}$$

$$\vec{V} = u\vec{i} + v\vec{j} + w\vec{k} \tag{3-10}$$

In equation (3-10), $\vec{i}, \vec{j}$ and $\vec{k}$ are the unit vectors in x, y and z directions respectively; Ω is the x component of the rotational velocity; u, v and w are the x, y and z components of the velocity vector ($\vec{V}$) respectively.

Expanding $-2\vec{\omega}\times\vec{V}$ term, the Coriolis acceleration can be found to be:

$$-2\vec{\omega}\times\vec{V}=-2\begin{vmatrix}\vec{i} & \vec{j} & \vec{k}\\ \Omega & 0 & 0\\ u & v & w\end{vmatrix} \tag{3-11}$$

$$d\vec{f}_{Coriolis}=0\vec{i}+2\Omega w\vec{j}-2\Omega v\vec{k}$$

Substituting the expressions found for the centrifugal acceleration (equation (3-9)) and Coriolis acceleration (equation (3-11)) into the expression given for the body forces (equation (3-5)), final form of the body forces can be found out to be:

$$d\vec{f}_{body}=g_x\vec{i}+\left[g_y+\Omega^2(y-y_c)+2\Omega w\right]\vec{j}+\left[g_z+\Omega^2(z-z_c)-2\Omega v\right]\vec{k} \tag{3-12}$$

In equation (3-12), g_x, g_y and g_z are x, y and z components of gravitational acceleration respectively; Ω is the x component of rotational velocity; y_c and z_c are the coordinates of the axis of rotation; and finally x, y and z are the coordinates of the fluid element.

3.3.4 Surface Forces

Surface forces are divided into two types, i.e.; pressure and friction forces.

$$d\vec{F}_{surface}=d\vec{F}_{pressure}+d\vec{F}_{friction} \tag{3-13}$$

These forces are not inertial forces, hence they act on the surfaces of the element shown in Figure 11.

3.3.5 Pressure Forces

In Figure 12 the pressure forces acting on the very same infinitesimal element are shown. It is assumed that the pressure at the center of the element is P and pressure values on the 6 faces can be approximated by a Taylor series expansion of the value at the center. Since the element is

infinitesimally small, second and higher order terms in the Taylor series expansion are neglected.

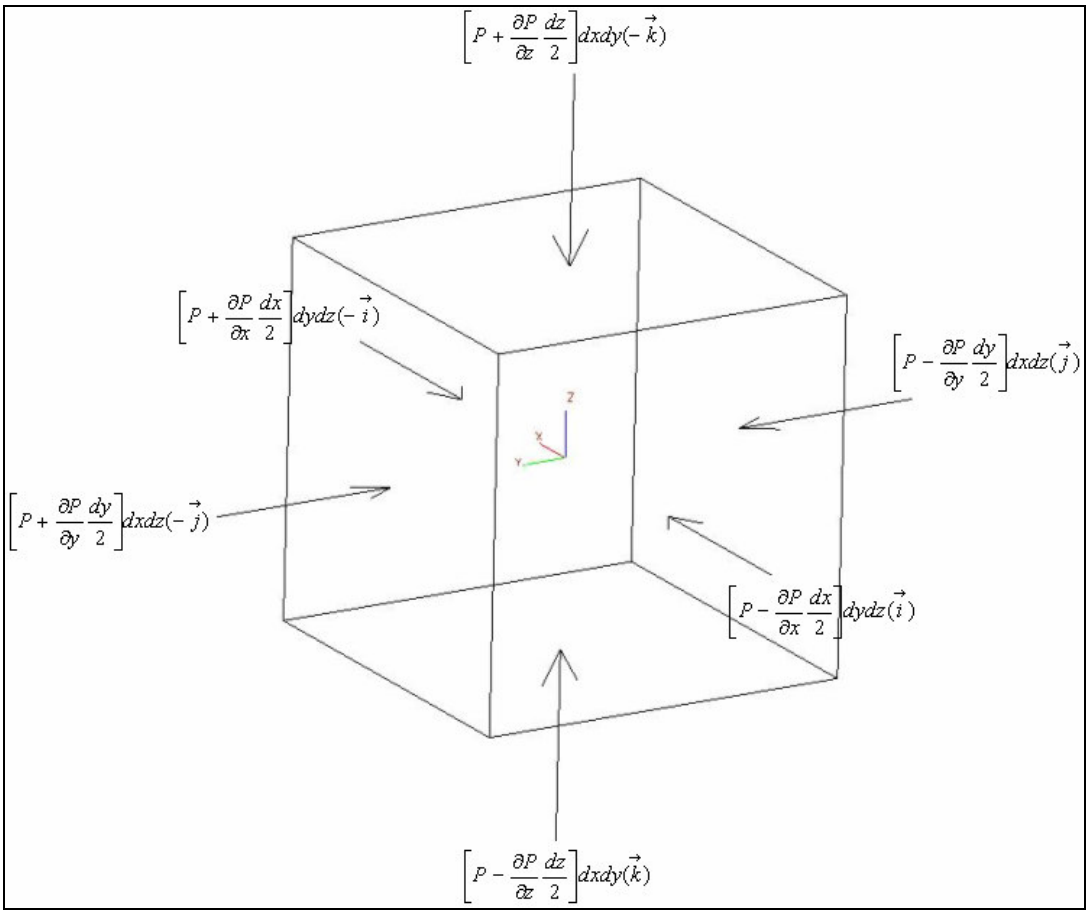

Figure 12 Pressure forces acting on the surfaces of an infinitesimal fluid element

Summing up the pressure forces in x, y and z directions:

$$\begin{aligned} d\vec{F}_{pressure} = & \left[P - \frac{\partial P}{\partial x}\frac{dx}{2} \right] dydz\vec{i} - \left[P + \frac{\partial P}{\partial x}\frac{dx}{2} \right] dydz\vec{i} \\ & + \left[P - \frac{\partial P}{\partial y}\frac{dy}{2} \right] dxdz\vec{j} - \left[P + \frac{\partial P}{\partial y}\frac{dy}{2} \right] dxdz\vec{j} \\ & + \left[P - \frac{\partial P}{\partial z}\frac{dz}{2} \right] dxdy\vec{k} - \left[P + \frac{\partial P}{\partial z}\frac{dz}{2} \right] dxdy\vec{k} \end{aligned} \tag{3-14}$$

Rearranging similar terms in equation (3-14), the final expression for the pressure forces is found out to be:

$$d\vec{F}_{pressure} = -\frac{\partial P}{\partial x} dxdydz\vec{i} - \frac{\partial P}{\partial y} dxdydz\vec{j} - \frac{\partial P}{\partial z} dxdydz\vec{k} \tag{3-15}$$

3.3.6 Friction Forces

In Figure 13, the friction forces acting on the 6 faces of the infinitesimal fluid element are depicted. It is assumed that the stress tensor at the center of the element is $\begin{bmatrix} \tau_{xx} & \tau_{xy} & \tau_{xz} \\ \tau_{yx} & \tau_{yy} & \tau_{yz} \\ \tau_{zx} & \tau_{zy} & \tau_{zz} \end{bmatrix}$ and the stresses acting on the surfaces of the element can be determined by using a Taylor series expansion of the stresses about the center of the element.

In order not to have any resultant torque moment around the centroidal axes of the fluid element, the off-diagonal terms must be symmetrical. Again since the element is infinitesimally small, second and higher order terms in the Taylor series expansion are neglected.

Summing up frictional forces in x, y and z directions:

$$
\begin{aligned}
d\vec{F}_{friction} = & \left[\tau_{xx} + \frac{\partial \tau_{xx}}{\partial x}\frac{dx}{2}\right] dydz\vec{i} + \left[\tau_{yx} + \frac{\partial \tau_{yx}}{\partial y}\frac{dy}{2}\right] dxdz\vec{i} + \left[\tau_{zx} + \frac{\partial \tau_{zx}}{\partial z}\frac{dz}{2}\right] dxdy\vec{i} \\
& - \left[\tau_{xx} - \frac{\partial \tau_{xx}}{\partial x}\frac{dx}{2}\right] dydz\vec{i} - \left[\tau_{yx} - \frac{\partial \tau_{yx}}{\partial y}\frac{dy}{2}\right] dxdz\vec{i} - \left[\tau_{zx} - \frac{\partial \tau_{zx}}{\partial z}\frac{dz}{2}\right] dxdy\vec{i} \\
& + \left[\tau_{xy} + \frac{\partial \tau_{xy}}{\partial x}\frac{dx}{2}\right] dydz\vec{j} + \left[\tau_{yy} + \frac{\partial \tau_{yy}}{\partial y}\frac{dy}{2}\right] dxdz\vec{j} + \left[\tau_{zy} + \frac{\partial \tau_{zy}}{\partial z}\frac{dz}{2}\right] dxdy\vec{j} \\
& - \left[\tau_{xy} - \frac{\partial \tau_{xy}}{\partial x}\frac{dx}{2}\right] dydz\vec{j} - \left[\tau_{yy} - \frac{\partial \tau_{yy}}{\partial y}\frac{dy}{2}\right] dxdz\vec{j} - \left[\tau_{zy} - \frac{\partial \tau_{zy}}{\partial z}\frac{dz}{2}\right] dxdy\vec{j} \\
& + \left[\tau_{xz} + \frac{\partial \tau_{xz}}{\partial x}\frac{dx}{2}\right] dydz\vec{k} + \left[\tau_{yz} + \frac{\partial \tau_{yz}}{\partial y}\frac{dy}{2}\right] dxdz\vec{k} + \left[\tau_{zz} + \frac{\partial \tau_{zz}}{\partial z}\frac{dz}{2}\right] dxdy\vec{k} \\
& - \left[\tau_{xz} - \frac{\partial \tau_{xz}}{\partial x}\frac{dx}{2}\right] dydz\vec{k} - \left[\tau_{yz} - \frac{\partial \tau_{yz}}{\partial y}\frac{dy}{2}\right] dxdz\vec{k} - \left[\tau_{zz} - \frac{\partial \tau_{zz}}{\partial z}\frac{dz}{2}\right] dxdy\vec{k}
\end{aligned}
\tag{3-16}
$$

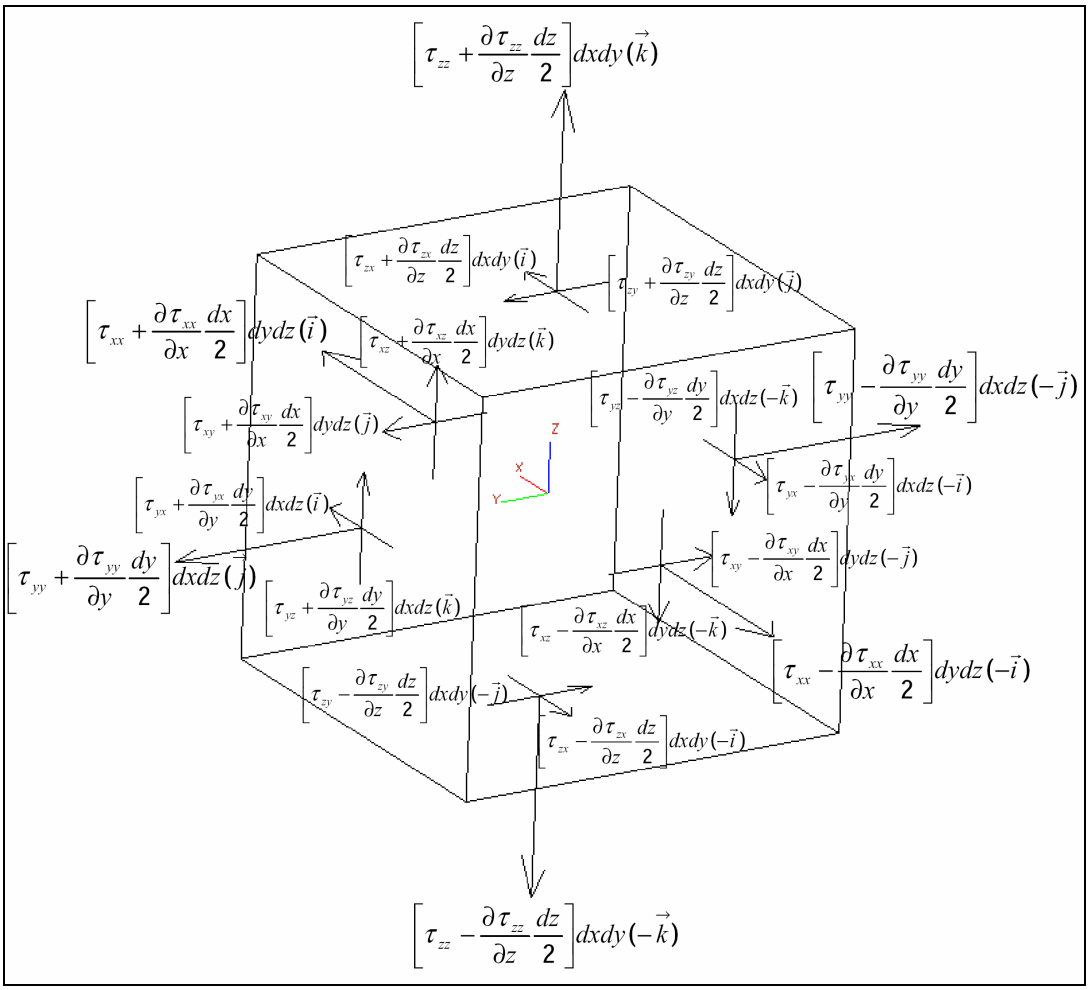

Figure 13 Friction forces acting on the surfaces of an infinitesimal fluid element

Rearranging similar terms in equation (3-16):

$$d\vec{F}_{friction}=\left(\frac{\partial\tau_{xx}}{\partial x}+\frac{\partial\tau_{yx}}{\partial y}+\frac{\partial\tau_{zx}}{\partial z}\right)dxdydz\vec{i}+\left(\frac{\partial\tau_{xy}}{\partial x}+\frac{\partial\tau_{yy}}{\partial y}+\frac{\partial\tau_{zy}}{\partial z}\right)dxdydz\vec{j}+\left(\frac{\partial\tau_{xz}}{\partial x}+\frac{\partial\tau_{yz}}{\partial y}+\frac{\partial\tau_{zz}}{\partial z}\right)dxdydz\vec{k} \quad (3\text{-}17)$$

At this stage making Newtonian fluid assumption, the shear and normal stresses can be expressed in terms of velocity gradients and fluid properties (Aksel M. H., 2003):

$$\tau_{xx} = \lambda\left(\vec{\nabla}\cdot\vec{V}\right) + 2\mu\frac{\partial u}{\partial x}$$

$$\tau_{yy} = \lambda\left(\vec{\nabla}\cdot\vec{V}\right) + 2\mu\frac{\partial v}{\partial y}$$

$$\tau_{zz} = \lambda\left(\vec{\nabla}\cdot\vec{V}\right) + 2\mu\frac{\partial w}{\partial z} \qquad (3\text{-}18)$$

$$\tau_{xy} = \tau_{yx} = \mu\left(\frac{\partial u}{\partial y} + \frac{\partial v}{\partial x}\right)$$

$$\tau_{xz} = \tau_{zx} = \mu\left(\frac{\partial u}{\partial z} + \frac{\partial w}{\partial x}\right)$$

$$\tau_{yz} = \tau_{zy} = \mu\left(\frac{\partial v}{\partial z} + \frac{\partial w}{\partial y}\right)$$

In equation (3-18), $\vec{\nabla}$ is the gradient operator; $\vec{V}$ is the velocity vector of the fluid element; u, v and w are x, y and z components of velocity vector $\vec{V}$ respectively; λ and μ are the first and second viscosity constants of the fluid respectively. For Newtonian fluids, first and second viscosity constants are related as follows (Aksel M. H., 2003):

$$\lambda = -\frac{2}{3}\mu \qquad (3\text{-}19)$$

Substituting equation (3-19) into equation (3-18) and then substituting equation (3-18) back into equation (3-17) one obtains:

$$\begin{aligned} d\vec{F}_{friction} = &\left\{\mu\frac{\partial}{\partial x}\left[-\frac{2}{3}\left(\vec{\nabla}\cdot\vec{V}\right) + 2\frac{\partial u}{\partial x}\right] + \mu\frac{\partial}{\partial y}\left[\frac{\partial u}{\partial y} + \frac{\partial v}{\partial x}\right] + \mu\frac{\partial}{\partial z}\left[\frac{\partial u}{\partial z} + \frac{\partial w}{\partial x}\right]\right\}dxdydz\vec{i} \\ &+ \left\{\mu\frac{\partial}{\partial x}\left[\frac{\partial u}{\partial y} + \frac{\partial v}{\partial x}\right] + \mu\frac{\partial}{\partial y}\left[-\frac{2}{3}\left(\vec{\nabla}\cdot\vec{V}\right) + 2\frac{\partial v}{\partial y}\right] + \mu\frac{\partial}{\partial z}\left[\frac{\partial v}{\partial z} + \frac{\partial w}{\partial y}\right]\right\}dxdydz\vec{j} \\ &+ \left\{\mu\frac{\partial}{\partial x}\left[\frac{\partial u}{\partial z} + \frac{\partial w}{\partial x}\right] + \mu\frac{\partial}{\partial y}\left[\frac{\partial v}{\partial z} + \frac{\partial w}{\partial y}\right] + \mu\frac{\partial}{\partial z}\left[-\frac{2}{3}\left(\vec{\nabla}\cdot\vec{V}\right) + 2\frac{\partial w}{\partial z}\right]\right\}dxdydz\vec{k} \end{aligned} \qquad (3\text{-}20)$$

Expanding the derivative terms in equation (3-20):

$$\begin{aligned} d\vec{F}_{friction} &= \left\{ \mu \frac{\partial}{\partial x}\left[-\frac{2}{3}\left(\vec{\nabla}\cdot\vec{V}\right)\right] + 2\mu\frac{\partial^2 u}{\partial x^2} + \mu\frac{\partial^2 u}{\partial y^2} + \mu\frac{\partial^2 v}{\partial y \partial x} + \mu\frac{\partial^2 u}{\partial z^2} + \mu\frac{\partial^2 w}{\partial z \partial x} \right\} dxdydz\vec{i} \\ &+ \left\{ \mu\frac{\partial^2 u}{\partial x \partial y} + \mu\frac{\partial^2 v}{\partial x^2} + \mu\frac{\partial}{\partial y}\left[-\frac{2}{3}\left(\vec{\nabla}\cdot\vec{V}\right)\right] + 2\mu\frac{\partial^2 v}{\partial y^2} + \mu\frac{\partial^2 v}{\partial z^2} + \mu\frac{\partial^2 w}{\partial z \partial y} \right\} dxdydz\vec{j} \\ &+ \left\{ \mu\frac{\partial^2 u}{\partial x \partial z} + \mu\frac{\partial^2 w}{\partial x^2} + \mu\frac{\partial^2 v}{\partial y \partial z} + \mu\frac{\partial^2 w}{\partial y^2} + \mu\frac{\partial}{\partial z}\left[-\frac{2}{3}\left(\vec{\nabla}\cdot\vec{V}\right)\right] + 2\mu\frac{\partial^2 w}{\partial z^2} \right\} dxdydz\vec{k} \end{aligned} \quad (3\text{-}21)$$

Rearranging equation (3-21):

$$\begin{aligned} d\vec{F}_{friction} &= \left\{ \mu \frac{\partial}{\partial x}\left[-\frac{2}{3}\left(\vec{\nabla}\cdot\vec{V}\right)\right] + \mu\frac{\partial^2 u}{\partial x^2} + \mu\frac{\partial^2 u}{\partial y^2} + \mu\frac{\partial^2 u}{\partial z^2} + \mu\frac{\partial}{\partial x}\left[\frac{\partial u}{\partial x} + \frac{\partial v}{\partial y} + \frac{\partial w}{\partial z}\right] \right\} dxdydz\vec{i} \\ &+ \left\{ \mu \frac{\partial}{\partial y}\left[-\frac{2}{3}\left(\vec{\nabla}\cdot\vec{V}\right)\right] + \mu\frac{\partial^2 v}{\partial x^2} + \mu\frac{\partial^2 v}{\partial y^2} + \mu\frac{\partial^2 v}{\partial z^2} + \mu\frac{\partial}{\partial y}\left[\frac{\partial u}{\partial x} + \frac{\partial v}{\partial y} + \frac{\partial w}{\partial z}\right] \right\} dxdydz\vec{j} \\ &+ \left\{ \mu \frac{\partial}{\partial z}\left[-\frac{2}{3}\left(\vec{\nabla}\cdot\vec{V}\right)\right] + \mu\frac{\partial^2 w}{\partial x^2} + \mu\frac{\partial^2 w}{\partial y^2} + \mu\frac{\partial^2 w}{\partial z^2} + \mu\frac{\partial}{\partial z}\left[\frac{\partial u}{\partial x} + \frac{\partial v}{\partial y} + \frac{\partial w}{\partial z}\right] \right\} dxdydz\vec{k} \end{aligned} \quad (3\text{-}22)$$

In equation (3-22) realizing that the term $\frac{\partial u}{\partial x}+\frac{\partial v}{\partial y}+\frac{\partial w}{\partial z}$ is nothing but $\vec{\nabla}\cdot\vec{V}$ and rearranging similar terms:

$$\begin{aligned} d\vec{F}_{friction} &= \left\{ \mu \frac{\partial}{\partial x}\left[\frac{1}{3}\left(\vec{\nabla}\cdot\vec{V}\right)\right] + \mu\frac{\partial^2 u}{\partial x^2} + \mu\frac{\partial^2 u}{\partial y^2} + \mu\frac{\partial^2 u}{\partial z^2} \right\} dxdydz\vec{i} \\ &+ \left\{ \mu \frac{\partial}{\partial y}\left[\frac{1}{3}\left(\vec{\nabla}\cdot\vec{V}\right)\right] + \mu\frac{\partial^2 v}{\partial x^2} + \mu\frac{\partial^2 v}{\partial y^2} + \mu\frac{\partial^2 v}{\partial z^2} \right\} dxdydz\vec{j} \\ &+ \left\{ \mu \frac{\partial}{\partial z}\left[\frac{1}{3}\left(\vec{\nabla}\cdot\vec{V}\right)\right] + \mu\frac{\partial^2 w}{\partial x^2} + \mu\frac{\partial^2 w}{\partial y^2} + \mu\frac{\partial^2 w}{\partial z^2} \right\} dxdydz\vec{k} \end{aligned} \quad (3\text{-}23)$$

For incompressible flows, using equation of continuity, it can be shown that $\vec{\nabla}\cdot\vec{V}=0$ (Batchelor G. K., 1967).

Finally friction forces $d\vec{F}_{friction}$ can be expressed as follows:

$$d\vec{F}_{friction} = \left\{ \begin{array}{l} \left[\mu \frac{\partial^2 u}{\partial x^2} + \mu \frac{\partial^2 u}{\partial^2 y} + \mu \frac{\partial^2 u}{\partial^2 z} \right] \vec{i} + \left[\mu \frac{\partial^2 v}{\partial^2 x} + \mu \frac{\partial^2 v}{\partial^2 y} + \mu \frac{\partial^2 v}{\partial^2 z} \right] \vec{j} \\ + \left[\mu \frac{\partial^2 w}{\partial^2 x} + \mu \frac{\partial^2 w}{\partial^2 y} + \mu \frac{\partial^2 w}{\partial^2 z} \right] \vec{k} \end{array} \right\} dxdydz \qquad (3\text{-}24)$$

Substituting the expressions found for pressure forces $d\vec{F}_{pressure}$ and friction forces $d\vec{F}_{friction}$ (i.e. equations (3-15) and (3-24)) back into the expression given above for the surface forces (3-13) one gets the final form of the surface forces:

$$d\vec{F}_{surface} = d\vec{F}_{pressure} + d\vec{F}_{friction}$$

$$d\vec{F}_{surface} = \left\{ \begin{array}{l} \left[-\frac{\partial P}{\partial x} + \mu \frac{\partial^2 u}{\partial x^2} + \mu \frac{\partial^2 u}{\partial^2 y} + \mu \frac{\partial^2 u}{\partial^2 z} \right] \vec{i} \\ + \left[-\frac{\partial P}{\partial y} + \mu \frac{\partial^2 v}{\partial^2 x} + \mu \frac{\partial^2 v}{\partial^2 y} + \mu \frac{\partial^2 v}{\partial^2 z} \right] \vec{j} \\ + \left[-\frac{\partial P}{\partial z} + \mu \frac{\partial^2 w}{\partial^2 x} + \mu \frac{\partial^2 w}{\partial^2 y} + \mu \frac{\partial^2 w}{\partial^2 z} \right] \vec{k} \end{array} \right\} dxdydz \qquad (3\text{-}25)$$

Finally substituting the expressions found for the surface forces $d\vec{F}_{surface}$ and body forces $d\vec{f}_{body}$ multiplied by dm (i.e. equations (3-25) and (3-12)) back into the expression given above for the net forces acting on the fluid element (3-3):

$$d\vec{F} = d\vec{F}_{body} + d\vec{F}_{surface}$$

$$\boxed{d\vec{F} = \left\{ \begin{array}{l} \left[\rho g_x - \frac{\partial P}{\partial x} + \mu \frac{\partial^2 u}{\partial x^2} + \mu \frac{\partial^2 u}{\partial^2 y} + \mu \frac{\partial^2 u}{\partial^2 z} \right] \vec{i} \\ + \left[\rho \left[g_y + \Omega^2 (y - y_c) - 2\Omega w \right] - \frac{\partial P}{\partial y} + \mu \frac{\partial^2 v}{\partial^2 x} + \mu \frac{\partial^2 v}{\partial^2 y} + \mu \frac{\partial^2 v}{\partial^2 z} \right] \vec{j} \\ + \left[\rho \left[g_z + \Omega^2 (z - z_c) + 2\Omega v \right] - \frac{\partial P}{\partial z} + \mu \frac{\partial^2 w}{\partial^2 x} + \mu \frac{\partial^2 w}{\partial^2 y} + \mu \frac{\partial^2 w}{\partial^2 z} \right] \vec{k} \end{array} \right\} dxdydz} \qquad (3\text{-}26)$$

Having calculated the net external forces acting on the fluid element (3-26), this equation is substituted into the statement of Newton's 2nd law of motion (3-2).

It's given above that Newton's 2nd law of motion for an infinitesimal fluid element can be stated by equation (3-2):

$$d\vec{F} = dm\vec{a}$$

In equation (3-2), $d\vec{F}$ is the resultant of all external forces applied on the element (which is the resultant of body and surface forces and given by equation (3-26); dm is the mass of the infinitesimally small fluid element and is equal to ρdxdydz; and $\vec{a}$ is the acceleration of the fluid element. The acceleration $\vec{a}$ is the total derivative of the velocity vector $\vec{V}$ of the element and is given by (Aksel M. H., 2003):

$$\vec{a} = \frac{D\vec{V}}{dt} = \frac{\partial \vec{V}}{\partial t} + \left(\vec{V} \cdot \vec{\nabla}\right)\vec{V} \qquad (3\text{-}27)$$

Equation (3-27) is obtained by the application of the Reynold's Transport Theorem on the fluid element. The detail of this derivation is given in many references (Batchelor G. K., 1967), so it is not repeated here. In equation (3-27) $\vec{V}$ is the velocity vector of the fluid element and $\vec{\nabla}$ is the gradient operator. Expanding both $\vec{V}$ and $\vec{\nabla}$ to their x, y and z components and substituting into equation (3-27):

$$\vec{a} = \frac{D\vec{V}}{dt} = \frac{\partial}{\partial t}\left(u\vec{i} + v\vec{j} + w\vec{k}\right) + \left[\left(u\vec{i} + v\vec{j} + w\vec{k}\right) \cdot \left(\frac{\partial}{\partial x}\vec{i} + \frac{\partial}{\partial y}\vec{j} + \frac{\partial}{\partial z}\vec{k}\right)\right]\left(u\vec{i} + v\vec{j} + w\vec{k}\right)$$

After manipulations:

$$\vec{a} = \frac{D\vec{V}}{dt} = \frac{\partial}{\partial t}\left(u\vec{i} + v\vec{j} + w\vec{k}\right) + \left[\left(u\frac{\partial}{\partial x} + v\frac{\partial}{\partial y} + w\frac{\partial}{\partial z}\right)\right]\left(u\vec{i} + v\vec{j} + w\vec{k}\right)$$

And rearranging:

$$\vec{a} = \frac{D\vec{V}}{dt} = \left(\frac{\partial u}{\partial t} + u\frac{\partial u}{\partial x} + v\frac{\partial u}{\partial y} + w\frac{\partial u}{\partial z}\right)\vec{i} + \left(\frac{\partial v}{\partial t} + u\frac{\partial v}{\partial x} + v\frac{\partial v}{\partial y} + w\frac{\partial v}{\partial z}\right)\vec{j} + \left(\frac{\partial w}{\partial t} + u\frac{\partial w}{\partial x} + v\frac{\partial w}{\partial y} + w\frac{\partial w}{\partial z}\right)\vec{k} \tag{3-28}$$

Finally, equations (3-28) and (3-26) can be substituted back into equation (3-2) to obtain:

$$\left\{\begin{array}{l}\left[\rho g_x - \frac{\partial P}{\partial x} + \mu\frac{\partial^2 u}{\partial x^2} + \mu\frac{\partial^2 u}{\partial^2 y} + \mu\frac{\partial^2 u}{\partial^2 z}\right]\vec{i} \\ + \left[\rho\left[g_y + \Omega^2(y - y_c) - 2\Omega w\right] - \frac{\partial P}{\partial y} + \mu\frac{\partial^2 v}{\partial^2 x} + \mu\frac{\partial^2 v}{\partial^2 y} + \mu\frac{\partial^2 v}{\partial^2 z}\right]\vec{j} \\ + \left[\rho\left[g_z + \Omega^2(z - z_c) + 2\Omega v\right] - \frac{\partial P}{\partial z} + \mu\frac{\partial^2 w}{\partial^2 x} + \mu\frac{\partial^2 w}{\partial^2 y} + \mu\frac{\partial^2 w}{\partial^2 z}\right]\vec{k}\end{array}\right\} dxdydz =$$

$$\rho dxdydz\left\{\begin{array}{l}\left(\frac{\partial u}{\partial t} + u\frac{\partial u}{\partial x} + v\frac{\partial u}{\partial y} + w\frac{\partial u}{\partial z}\right)\vec{i} \\ + \left(\frac{\partial v}{\partial t} + u\frac{\partial v}{\partial x} + v\frac{\partial v}{\partial y} + w\frac{\partial v}{\partial z}\right)\vec{j} \\ + \left(\frac{\partial w}{\partial t} + u\frac{\partial w}{\partial x} + v\frac{\partial w}{\partial y} + w\frac{\partial w}{\partial z}\right)\vec{k}\end{array}\right\}$$

After cancellations and rearranging one obtains:

$$\left\{\begin{array}{l}\left(\frac{\partial u}{\partial t} + u\frac{\partial u}{\partial x} + v\frac{\partial u}{\partial y} + w\frac{\partial u}{\partial z}\right)\vec{i} \\ + \left(\frac{\partial v}{\partial t} + u\frac{\partial v}{\partial x} + v\frac{\partial v}{\partial y} + w\frac{\partial v}{\partial z}\right)\vec{j} \\ + \left(\frac{\partial w}{\partial t} + u\frac{\partial w}{\partial x} + v\frac{\partial w}{\partial y} + w\frac{\partial w}{\partial z}\right)\vec{k}\end{array}\right\} = \left\{\begin{array}{l}\left[g_x - \frac{1}{\rho}\frac{\partial P}{\partial x} + \nu\frac{\partial^2 u}{\partial x^2} + \nu\frac{\partial^2 u}{\partial^2 y} + \nu\frac{\partial^2 u}{\partial^2 z}\right]\vec{i} \\ + \left[\begin{array}{l}\left[g_y + \Omega^2(y - y_c) + 2\Omega w\right] \\ -\frac{1}{\rho}\frac{\partial P}{\partial y} + \nu\frac{\partial^2 v}{\partial^2 x} + \nu\frac{\partial^2 v}{\partial^2 y} + \nu\frac{\partial^2 v}{\partial^2 z}\end{array}\right]\vec{j} \\ + \left[\begin{array}{l}\left[g_z + \Omega^2(z - z_c) - 2\Omega v\right] \\ -\frac{1}{\rho}\frac{\partial P}{\partial z} + \nu\frac{\partial^2 w}{\partial^2 x} + \nu\frac{\partial^2 w}{\partial^2 y} + \nu\frac{\partial^2 w}{\partial^2 z}\end{array}\right]\vec{k}\end{array}\right\} \tag{3-29}$$

Equation (3-29) may be referred to as “Navier-Stokes equation with body forces due to rotational motion”.

3.4 Conservation of Energy

Conservation of energy principle may be stated simply as follows: the change in total energy of a fluid element (ΔE) is equal to the sum of the heat added to the fluid element (ΔQ) and work done on the fluid element (ΔW) (Çıray C., 2000).

$$\Delta E = \Delta Q + \Delta W \tag{3-30}$$

In equation (3-30) ΔE is the change in total energy of the fluid element. Total energy is the sum of:

i. Internal energy (e),

ii. Potential energy (gh),

iii. Kinetic energy ($\frac{V^2}{2}$) of the fluid element.

Since the fluid in the present problem is air, the potential energy term may be neglected.

ΔQ is the heat added to the fluid element. Heat added is the sum of:

i. Heat generated inside the fluid element ($\dot{q}$),

ii. Net heat flux through the faces of the element (q),

In the present problem there’s no heat generated inside the element.

ΔW is the work done on the fluid element. Work done is the sum of:

i. Work done by the external forces applied on the element ($W_{\text{external forces}}$),

ii. Shaft work inside the fluid element (W_{shaft}),

In the present problem there's no shaft work inside the element and the work done by the external forces may be found by multiplying each force's x, y or z component with the same component of the velocity vector.

Equation (3-30) is given for the whole control volume. Applying the same relation to the aforementioned infinitesimal element:

$$\rho \frac{D}{dt}\left(e + \frac{V^2}{2} \right) dxdydz = \delta Q_{heat\ flux} + \delta W_{external\ forces} \qquad (3\text{-}31)$$

The heat fluxes through the boundaries and the work done by the body and pressure forces on the aforementioned infinitesimal element is given below in Figure 14. The work done by the friction forces is not depicted in the figure for the sake of understandability of the figure.

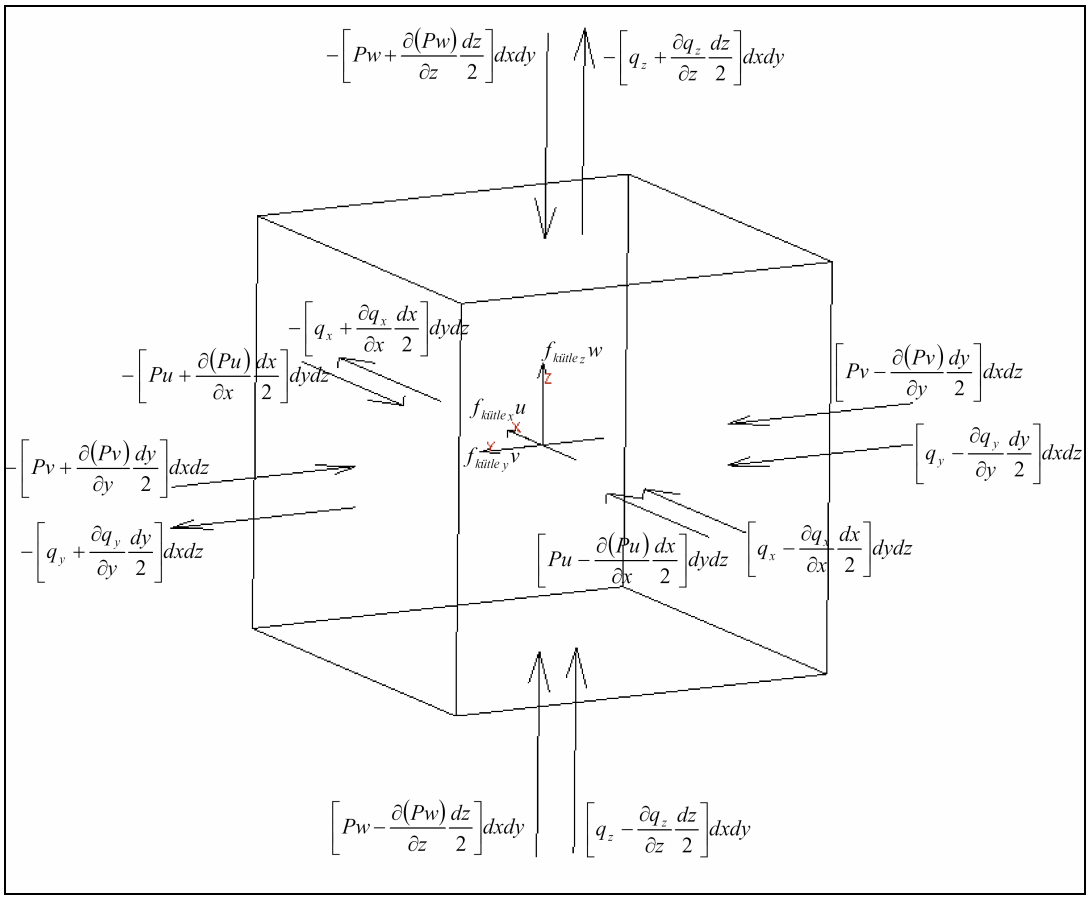

Figure 14 Heat fluxes and the work done by the body and pressure forces on the infinitesimal fluid element

Summing up heat fluxes:

$$\begin{aligned}\delta Q_{heat\ flux} &= \left[q_x-\frac{\partial q_x}{\partial x}\frac{dx}{2}\right]dydz-\left[q_x+\frac{\partial q_x}{\partial x}\frac{dx}{2}\right]dydz \\ &+\left[q_y-\frac{\partial q_y}{\partial y}\frac{dy}{2}\right]dxdz-\left[q_y+\frac{\partial q_y}{\partial y}\frac{dy}{2}\right]dxdz \\ &+\left[q_z-\frac{\partial q_z}{\partial z}\frac{dz}{2}\right]dxdy-\left[q_z+\frac{\partial q_z}{\partial z}\frac{dz}{2}\right]dxdy\end{aligned} \tag{3-32}$$

Rearranging equation (3-32) one gets:

$$\delta Q_{heat\ flux} = -\left(\frac{\partial q_x}{\partial x} + \frac{\partial q_y}{\partial y} + \frac{\partial q_z}{\partial z} \right) dxdydz \tag{3-33}$$

Summing up the work done by the body and pressure forces:

$$\begin{aligned} \delta W_{\substack{body \\ and \\ pressure \\ forces}} &= \left[Pu - \frac{\partial (Pu)}{\partial x} \frac{dx}{2} \right] dydz - \left[Pu + \frac{\partial (Pu)}{\partial x} \frac{dx}{2} \right] dydz + (g_x) u \rho dxdydz \\ &+ \left[Pv - \frac{\partial (Pv)}{\partial y} \frac{dy}{2} \right] dxdz - \left[Pv + \frac{\partial (Pv)}{\partial y} \frac{dy}{2} \right] dxdz \\ &+ \left(g_y + \Omega^2 (y - y_c) - 2\Omega w \right) v \rho dxdydz \\ &+ \left[Pw - \frac{\partial (Pw)}{\partial z} \frac{dz}{2} \right] dxdy - \left[Pw + \frac{\partial (Pw)}{\partial z} \frac{dz}{2} \right] dxdy \\ &+ \left(g_z + \Omega^2 (z - z_c) + 2\Omega v \right) w \rho dxdydz \end{aligned} \tag{3-34}$$

Rearranging equation (3-34) by ignoring gravitational terms one gets:

$$\begin{aligned} \delta W_{\substack{body \\ and \\ pressure \\ forces}} &= -\left[\frac{\partial (Pu)}{\partial x} + \frac{\partial (Pv)}{\partial y} + \frac{\partial (Pw)}{\partial z} \right] dxdydz \\ &+ \rho \Omega^2 \left[(y - y_c) v + (z - z_c) w \right] dxdydz \end{aligned} \tag{3-35}$$

Work done by the friction forces may be obtained similar to the ones due to pressure forces (Aksel M. H., 2003):

$$\delta W_{friction\ forces} = \left\{ \begin{array}{l} \left[\frac{\partial (\tau_{xx} u)}{\partial x} + \frac{\partial (\tau_{yx} u)}{\partial y} + \frac{\partial (\tau_{zx} u)}{\partial z} \right] \\ + \left[\frac{\partial (\tau_{xy} v)}{\partial x} + \frac{\partial (\tau_{yy} v)}{\partial y} + \frac{\partial (\tau_{zy} v)}{\partial z} \right] \\ + \left[\frac{\partial (\tau_{xz} w)}{\partial x} + \frac{\partial (\tau_{yz} w)}{\partial y} + \frac{\partial (\tau_{zz} w)}{\partial z} \right] \end{array} \right\} dxdydz \tag{3-36}$$

Combining work done by the friction forces (3-36) with the work done by the body and pressure forces (3-35) and adding the heat fluxes (3-33) and finally substituting all back into equation (3-31) one obtains:

$$\rho\frac{D}{dt}\left(e+\frac{V^2}{2}\right)dxdydz=\left\{\begin{array}{l}-\left(\frac{\partial q_x}{\partial x}+\frac{\partial q_y}{\partial y}+\frac{\partial q_z}{\partial z}\right)-\left[\frac{\partial(Pu)}{\partial x}+\frac{\partial(Pv)}{\partial y}+\frac{\partial(Pw)}{\partial z}\right]\\+\left[\frac{\partial(\tau_{xx}u)}{\partial x}+\frac{\partial(\tau_{xy}v)}{\partial x}+\frac{\partial(\tau_{xz}w)}{\partial x}\right]\\+\left[\frac{\partial(\tau_{yx}u)}{\partial y}+\frac{\partial(\tau_{yy}v)}{\partial y}+\frac{\partial(\tau_{yz}w)}{\partial y}\right]\\+\left[\frac{\partial(\tau_{zx}u)}{\partial z}+\frac{\partial(\tau_{zy}v)}{\partial z}+\frac{\partial(\tau_{zz}w)}{\partial z}\right]\\+\rho\Omega^2[(y-y_c)v+(z-z_c)w]\end{array}\right\}dxdydz \qquad (3\text{-}37)$$

Rearranging equation (3-37):

$$\rho\frac{D}{dt}\left(e+\frac{V^2}{2}\right)=\left\{\begin{array}{l}-\left[\frac{\partial(Pu)}{\partial x}+\frac{\partial(Pv)}{\partial y}+\frac{\partial(Pw)}{\partial z}\right]\\+\frac{\partial}{\partial x}\left[(\tau_{xx}u)+(\tau_{xy}v)+(\tau_{xz}w)-q_x\right]\\+\frac{\partial}{\partial y}\left[(\tau_{yx}u)+(\tau_{yy}v)+(\tau_{yz}w)-q_y\right]\\+\frac{\partial}{\partial z}\left[(\tau_{zx}u)+(\tau_{zy}v)+(\tau_{zz}w)-q_z\right]\\+\rho\Omega^2[(y-y_c)v+(z-z_c)w]\end{array}\right\} \qquad (3\text{-}38)$$

Equation (3-38) may be referred to as “Energy equation with terms due to rotational motion”.

Equations (3-29) (Navier-Stokes), (3-38) (Energy) and Continuity equations may be put together in non-dimensional and conservative form as follows:

$$\frac{\partial Q}{\partial t}+\frac{\partial E}{\partial x}+\frac{\partial F}{\partial y}+\frac{\partial G}{\partial z}=\frac{1}{\mathrm{Re}}\left(\frac{\partial E_v}{\partial x}+\frac{\partial F_v}{\partial y}+\frac{\partial G_v}{\partial z}\right)+H \tag{3-39}$$

This vector equation states that the time rate of change in the dependent variables Q is equal to the spatial change in the inviscid fluxes, E,F and G, and viscous fluxes, E_v, F_v and G_v. A source term, H, is included to account for the centrifugal and Coriolis force terms, which appear if the coordinate frame is rotating as in the present case. The presence of the Reynolds number, $\mathrm{Re}=\frac{\overline{\rho u L}}{\overline{\mu}}$, implies that the governing equations are non-dimensionalized; with $\overline{\rho}$ and $\overline{u}$ often chosen as the freestream density and velocity, $\overline{L}$ chosen as the reference length of the body and $\overline{\mu}$ evaluated at the freestream static temperature.

$$Q=\begin{bmatrix}\rho\\ \rho u\\ \rho v\\ \rho w\\ \rho e_t\end{bmatrix}, E=\begin{bmatrix}\rho u\\ \rho u^2+P\\ \rho uv\\ \rho uw\\ (\rho e_t+P)u\end{bmatrix}, F=\begin{bmatrix}\rho v\\ \rho vu\\ \rho v^2+P\\ \rho vw\\ (\rho e_t+P)v\end{bmatrix}, G=\begin{bmatrix}\rho w\\ \rho wu\\ \rho wv\\ \rho w^2+P\\ (\rho e_t+P)w\end{bmatrix},$$

$$H=\begin{bmatrix}0\\ 0\\ \rho\left[\Omega^2(y-y_c)-2\Omega w\right]\\ \rho\left[\Omega^2(z-z_c)+2\Omega v\right]\\ \rho\Omega^2\left[(y-y_c)v+(z-z_c)w\right]\end{bmatrix}, E_v=\begin{bmatrix}0\\ \tau_{xx}\\ \tau_{xy}\\ \tau_{xz}\\ u\tau_{xx}+v\tau_{xy}+w\tau_{xz}-q_x\end{bmatrix},$$

$$F_v=\begin{bmatrix}0\\ \tau_{yx}\\ \tau_{yy}\\ \tau_{yz}\\ u\tau_{yx}+v\tau_{yy}+w\tau_{yz}-q_y\end{bmatrix}, G_v=\begin{bmatrix}0\\ \tau_{zx}\\ \tau_{zy}\\ \tau_{zz}\\ u\tau_{zx}+v\tau_{zy}+w\tau_{zz}-q_z\end{bmatrix}$$

In the present study 3D Euler solver is used. So it may be appropriate at this point to drop viscous terms from the governing equations and to see the equations in a more compact form.

$$\frac{\partial Q}{\partial t}+\frac{\partial E}{\partial x}+\frac{\partial F}{\partial y}+\frac{\partial G}{\partial z}=H \tag{3-40}$$

Where, Q is the vector of dependent variables; E,F and G are inviscid fluxes in x,y and z directions respectively and H is the source term that comes from centrifugal and Coriolis forces:

$$Q=\begin{bmatrix}\rho\\ \rho u\\ \rho v\\ \rho w\\ \rho e_t\end{bmatrix}, E=\begin{bmatrix}\rho u\\ \rho u^2+P\\ \rho uv\\ \rho uw\\ (\rho e_t+P)u\end{bmatrix}, F=\begin{bmatrix}\rho v\\ \rho vu\\ \rho v^2+P\\ \rho vw\\ (\rho e_t+P)v\end{bmatrix}$$

$$G=\begin{bmatrix}\rho w\\ \rho wu\\ \rho wv\\ \rho w^2+P\\ (\rho e_t+P)w\end{bmatrix} \quad H=\begin{bmatrix}0\\ 0\\ \rho\left[\Omega^2(y-y_c)-2\Omega w\right]\\ \rho\left[\Omega^2(z-z_c)+2\Omega v\right]\\ \rho\Omega^2\left[(y-y_c)v+(z-z_c)w\right]\end{bmatrix} \tag{3-41}$$

The pressure, p, which appears in the inviscid flux terms, is related to the dependent variables through an appropriate equation of state. The local pressure is expressed in terms of the dependent variables by applying the ideal gas law.

$$p=(\gamma-1)\left[e_t-\tfrac{1}{2}\rho\left(u^2+v^2+w^2\right)\right] \tag{3-42}$$

In many CFD applications, it is desirable to solve the governing equations in a domain, which has surfaces that conform to the body rather in a Cartesian coordinate system. A transformation is applied to the original set of equations to obtain a “generalized geometry” form of the governing

equations. This allows the irregular shaped physical domain to be transformed into a rectangular shaped computational domain that allows the numerical methods to be simplified. A more detailed information on coordinate transformations is given below.

3.5 Generalized Curvilinear Coordinate Transformations

Usually, before solution algorithms are implemented, the governing equations of motion have to be transformed from Cartesian domain to the computational domain. This is required to enhance the efficiency and accuracy of a numerical scheme and to simplify the implementation of boundary conditions.

In order to solve the equations of motion in the computational space, a transformation of the equations from physical domain to the computational domain is required. This transformation is depicted in Figure 15 below.

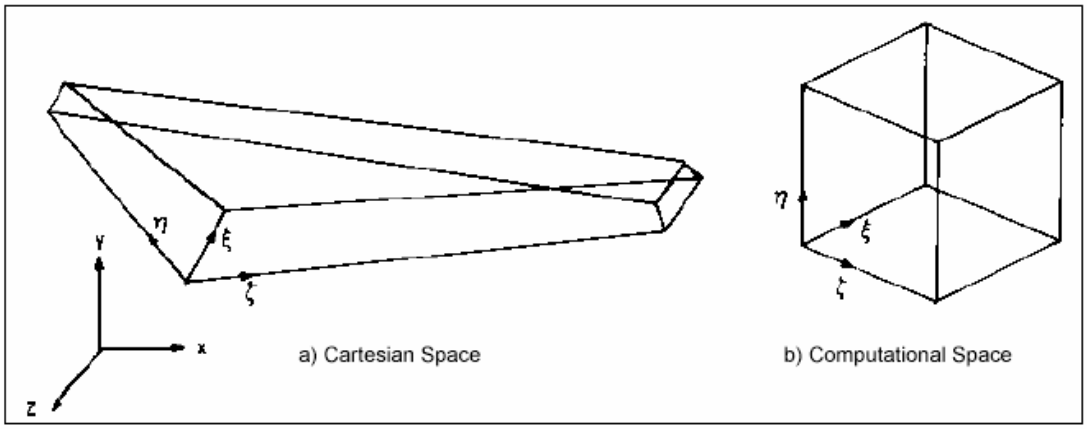

Figure 15 Generalized coordinate transformation from physical to computational space.

Typically the physical domain is oriented in such a way that the coordinate directions in the computational domain,ξ , η and ζ , correspond to

directions relative to the body. In the applications discussed similar to the present study, ξ corresponds to the direction along the body (axial direction), η corresponds to the circumferential direction and ζ corresponds to the outward direction from the body surface (Şen T. S., 2001).

The equations of motion are transformed from physical space (x, y, z) to the computational space (ξ ,η, ζ) by the following relations:

$$\begin{aligned} \tau &= t \\ \xi &= \xi(x, y, z, t) \\ \eta &= \eta(x, y, z, t) \\ \varsigma &= \varsigma(x, y, z, t) \end{aligned} \tag{3-43}$$

Writing the derivatives in both coordinate systems:

$$dt = d\tau$$

$$\begin{aligned} dx &= x_\tau d\tau + x_\xi d\xi + x_\eta d\eta + x_\zeta d\zeta \\ dy &= y_\tau d\tau + y_\xi d\xi + y_\eta d\eta + y_\zeta d\zeta \\ dz &= z_\tau d\tau + z_\xi d\xi + z_\eta d\eta + z_\zeta d\zeta \end{aligned} \tag{3-44}$$

Where x_ξ represents partial derivative of x with respect to ξ.

Re-writing equation (3-44) in matrix form:

$$\begin{bmatrix} dt \\ dx \\ dy \\ dz \end{bmatrix} = \begin{bmatrix} 1 & 0 & 0 & 0 \\ x_\tau & x_\xi & x_\eta & x_\zeta \\ y_\tau & y_\xi & y_\eta & y_\zeta \\ z_\tau & z_\xi & z_\eta & z_\zeta \end{bmatrix} \begin{bmatrix} d\tau \\ d\xi \\ d\eta \\ d\zeta \end{bmatrix} \tag{3-45}$$

Reversing the independent variables:

$$d\tau = dt$$

$$\begin{aligned} d\xi &= \xi_t dt + \xi_x dx + \xi_y dy + \xi_z dz \\ d\eta &= \eta_t dt + \eta_x dx + \eta_y dy + \eta_z dz \\ d\zeta &= \zeta_t dt + \zeta_x dx + \zeta_y dy + \zeta_z dz \end{aligned} \tag{3-46}$$

Equation (3-46) can also be written in matrix form:

$$\begin{bmatrix} d\tau \\ d\xi \\ d\eta \\ d\zeta \end{bmatrix} = \begin{bmatrix} 1 & 0 & 0 & 0 \\ \xi_t & \xi_x & \xi_y & \xi_z \\ \eta_t & \eta_x & \eta_y & \eta_z \\ \zeta_t & \zeta_x & \zeta_y & \zeta_z \end{bmatrix} \begin{bmatrix} dt \\ dx \\ dy \\ dz \end{bmatrix} \tag{3-47}$$

Comparing equations (3-46) and (3-47) one can see that:

$$\begin{bmatrix} 1 & 0 & 0 & 0 \\ \xi_t & \xi_x & \xi_y & \xi_z \\ \eta_t & \eta_x & \eta_y & \eta_z \\ \zeta_t & \zeta_x & \zeta_y & \zeta_z \end{bmatrix} = \begin{bmatrix} 1 & 0 & 0 & 0 \\ x_\tau & x_\xi & x_\eta & x_\zeta \\ y_\tau & y_\xi & y_\eta & y_\zeta \\ z_\tau & z_\xi & z_\eta & z_\zeta \end{bmatrix}^{-1} \tag{3-48}$$

All partial derivative terms (like ζ_t, ξ_x, etc.) are evaluated using equation (3-48). These terms are referred to as the metric terms. They are the result of the transformation and contain purely geometric information that relates the physical space to the computational space. The metric terms and the Jacobian of the transformation matrix can be calculated to be:

$$\begin{aligned} \xi_x &= J\left(y_\eta z_\zeta - y_\zeta z_\eta\right) & \eta_x &= J\left(z_\xi y_\zeta - y_\xi z_\zeta\right) \\ \xi_y &= J\left(z_\eta x_\zeta - x_\eta z_\zeta\right) & \eta_y &= J\left(x_\xi z_\zeta - x_\zeta z_\xi\right) \\ \xi_z &= J\left(x_\eta y_\zeta - y_\eta x_\zeta\right) & \eta_z &= J\left(y_\xi x_\zeta - x_\xi y_\zeta\right) \\ \zeta_x &= J\left(y_\xi z_\eta - z_\xi y_\eta\right) & \xi_t &= -x_\tau \xi_x - y_\tau \xi_y - z_\tau \xi_z \\ \zeta_y &= J\left(z_\xi x_\eta - x_\xi z_\eta\right) & \eta_t &= -x_\tau \eta_x - y_\tau \eta_y - z_\tau \eta_z \\ \zeta_z &= J\left(x_\xi y_\eta - y_\xi x_\eta\right) & \zeta_t &= -x_\tau \zeta_x - y_\tau \zeta_y - z_\tau \zeta_z \end{aligned} \tag{3-49}$$

$$J^{-1} = \frac{\partial(x,y,z)}{\partial(\xi,\eta,\zeta)} = x_\xi y_\eta z_\zeta + x_\zeta y_\xi z_\eta + x_\eta y_\zeta z_\xi - x_\xi y_\zeta z_\eta - x_\eta y_\xi z_\zeta - x_\zeta y_\eta z_\xi$$

Inside the code used in the present study, the metrics are evaluated using second-order, central difference formulas for interior points and three-point, one-sided formulas at the boundaries.

Having said that, one can write the Euler equations in computational domain as follows:

$$\frac{\partial \hat{Q}}{\partial \tau}+\frac{\partial \hat{E}}{\partial \xi}+\frac{\partial \hat{F}}{\partial \eta}+\frac{\partial \hat{G}}{\partial \zeta}=\hat{H} \tag{3-50}$$

where

$$\hat{\mathrm{Q}}=\frac{1}{J}\begin{bmatrix}\rho\\ \rho u\\ \rho v\\ \rho w\\ e_t\end{bmatrix},\hat{E}=\frac{1}{J}\begin{bmatrix}\rho U\\ \rho uU+\xi_x p\\ \rho vU+\xi_y p\\ \rho wU+\xi_z p\\ (e_t+p)U-\xi_t p\end{bmatrix},\hat{F}=\frac{1}{J}\begin{bmatrix}\rho V\\ \rho uV+\eta_x p\\ \rho vV+\eta_y p\\ \rho wV+\eta_z p\\ (e_t+p)V-\eta_t p\end{bmatrix},$$
$$\hat{G}=\frac{1}{J}\begin{bmatrix}\rho W\\ \rho uW+\zeta_x p\\ \rho vW+\zeta_y p\\ \rho wW+\zeta_z p\\ (e_t+p)W-\zeta_t p\end{bmatrix},\ \hat{H}=\frac{1}{J}\begin{bmatrix}0\\ 0\\ \rho\left[\Omega^2(y-y_c)-2\Omega w\right]\\ \rho\left[\Omega^2(z-z_c)+2\Omega v\right]\\ \rho\Omega^2\left[(y-y_c)v+(z-z_c)w\right]\end{bmatrix} \tag{3-51}$$

In equation (3-51) the velocities in ξ ,η, ζ coordinates are U, V and W respectively. They are referred to as the contravariant velocity components and are given by:

$$\begin{aligned}U&=\xi_t+\xi_x u+\xi_y v+\xi_z w\\ V&=\eta_t+\eta_x u+\eta_y v+\eta_z w\\ W&=\zeta_t+\zeta_x u+\zeta_y v+\zeta_z w\end{aligned} \tag{3-52}$$

CHAPTER 4

NUMERICAL METHOD

4.1 Introduction

The flow solver used in the CFD analysis is TAINS_103. TAINS is a multi-block structured Euler/Navier-Stokes finite difference compressible flow solver developed at TAI. The solution of the three-dimensional equations is implemented by an approximate factorization that allows the system of equations to be solved in three coupled one-dimensional steps. The approximate factorization method used in the solver is Beam and Warming's (Beam R. M., Warming R. F., 1978). The LU-ADI factorization (Fujii K., 1986) is one of those schemes that simplify inversion works for the left-hand side operators of the Beam and Warming's. Each ADI operator is decomposed to the product of the lower and upper bi-diagonal matrices by using the flux vector splitting technique (Steger J. L., Warming R.F., 1981). Since the time integration is implicit, its solution is accurate and quickly obtained.

4.2 Finite Differences Method, Numerical Algorithm

In order to develop numerical methods using finite differences to solve appearing partial differential equation sets, solution algorithms must be selected as either explicit or implicit methods. Explicit methods are in general easier to program and apply. Derivation and application are simpler when compared to implicit methods. Implicit methods are more-often have unconditional stability. So it becomes possible to take large steps through time using implicit methods. Although each iteration lasts longer, they

converge faster and they use larger time steps in unsteady flows compared leading faster solutions compared to explicit ones. They use less memory due to data structure and above all solutions are trustworthy since they are usually convergent.

Since small grid intervals are chosen to satisfy numerical sensitivity in solutions, using implicit methods, commitment of time step to satisfy stability condition in explicit methods is removed. Hence implicit methods are usually used in numerical solutions of Euler/thin-layer Navier-Stokes equations.

Starting point to derivation of used numerical algorithm is the result acquired by application of implicit time difference equation with three points by Beam & Warming to Euler equations given in equation (3-50) can be given as:

$$\Delta\tilde{Q}^n + h\left(\tilde{E}_\xi^{\,n+1} + \tilde{F}_\eta^{\,n+1} + \tilde{G}_\varsigma^{\,n+1} - \tilde{H}^{n+1}\right) = 0 \tag{4-1}$$

Where, n is the current time step and:

$$\begin{aligned} &\Delta\tilde{Q}^n = \tilde{Q}^{n+1} - \tilde{Q}^n \\ &\tilde{Q}^n = \tilde{Q}(n\Delta t) \qquad , \qquad h = \Delta t \end{aligned} \tag{4-2}$$

In equation (4-1), H source terms may be assumed to be constant. Moreover; *E*, *F* and *G* flux vectors are non-linear functions of Q and can be linearized using Taylor series as follows:

$$\begin{aligned} \tilde{E}^{n+1} &= \tilde{E}^n + \tilde{A}^n\Delta\tilde{Q}^n + O(h^2) \\ \tilde{F}^{n+1} &= \tilde{F}^n + \tilde{B}^n\Delta\tilde{Q}^n + O(h^2) \\ \tilde{G}^{n+1} &= \tilde{G}^n + \tilde{C}^n\Delta\tilde{Q}^n + O(h^2) \end{aligned} \tag{4-3}$$

Where,

$$\tilde{A} = \frac{\partial \tilde{E}}{\partial \tilde{Q}}, \quad \tilde{B} = \frac{\partial \tilde{F}}{\partial \tilde{Q}}, \quad \tilde{C} = \frac{\partial \tilde{G}}{\partial \tilde{Q}} \tag{4-4}$$

The terms in equation (4-4) are called the *Flux Jacobians*.

Substituting equation (4-4) into equation (4-3) and then substituting the resulting expression into equation (4-1), one gets the so-called *Delta Algorithm* as follows:

$$\left[I + h\partial_\xi \tilde{A}^n + h\partial_\eta \tilde{B}^n + h\partial_\varsigma \tilde{C}^n\right]\Delta\tilde{Q}^n = \ldots - h\left[\partial_\xi \tilde{E}^n + \partial_\eta \tilde{F}^n + \partial_\varsigma \tilde{G}^n - \tilde{H}^n\right] \tag{4-5}$$

Where higher order terms in equation (4-5) are neglected.

Partial derivatives in space are estimated with second-degree central differences. Hence the algorithm has first order sensitivity in time and second order sensitivity in space.

Approximate factorization (Beam R. M., Warming R. F., 1978) is applied in equation (4-5) to simplify numerical calculations. Afterwards numerical algorithm is developed using LU-ADI (Fujii K., 1986). Also to satisfy stability during solution of numerical method especially in non-linear flows (like flows with shocks), artificial dissipation terms are added to the algorithm.

4.3 Boundary Conditions

In any CFD analysis, assessment of boundary conditions is as important as solving the governing equations because the equations that govern the fluid flow are differential equations. Solution of any differential equation depends on the boundary conditions imposed at the boundaries.

Given below are the boundary conditions used and their explanations used in the present study. Some of the parameters regarding both the solver and boundary conditions are given at the and in Table 8.

4.3.1 Wall Boundary Condition

There are two important operations in this boundary condition which are velocity calculation and pressure calculation. In fact pressure calculation is not directly as a boundary condition; total energy term is used in boundary condition calculations.

$$e_t = \frac{p}{\gamma - 1} + \frac{1}{2}\rho\left(u^2 + v^2 + w^2\right) \tag{4-6}$$

Velocity calculation does not pose a problem in Navier-Stokes solutions because velocities are directly equated to zero regarding the “no-slip” condition. But in Euler solutions velocities are imposed on the wall according to the “flow tangency” condition. That is, locally the velocity components in the normal and perpendicular directions are equated to zero. However the tangential components are kept unchanged.

The velocity vector is first decomposed into local tangential and normal components, then the tangential components are distributed to Cartesian velocity components and pressure is calculated. The calculations are given below. Local normal and tangential directions are given in Figure 16

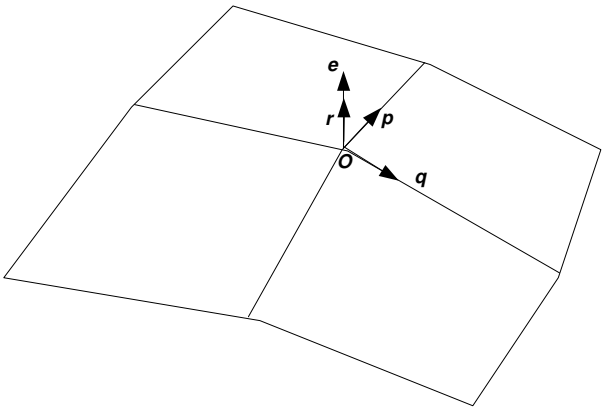

Figure 16 Vector representations on grid surfaces

First velocities are extrapolated from velocities in *P, Q, R* directions and r is set to zero:

$$
\begin{aligned}
&P_p = \begin{bmatrix} x_p & y_p & z_p \end{bmatrix}, \quad P_q = \begin{bmatrix} x_q & y_q & z_q \end{bmatrix}, \\
&e = \frac{P_p \times P_q}{\sqrt{(P_p \times P_q)^2}} = \frac{1}{\sqrt{r_x^{\,2} + r_y^{\,2} + r_z^{\,2}}} \begin{bmatrix} r_x & r_y & r_z \end{bmatrix} \\
&P = u \cdot x_p + v \cdot y_p + w \cdot z_p \quad ; \text{tangent velocity in p direction} \\
&Q = u \cdot x_q + v \cdot y_q + w \cdot z_q \quad ; \text{tangent velocity in q direction} \\
&\mathrm{R} = u \cdot x_r + v \cdot y_r + w \cdot z_r \quad ; \text{tangent velocity in r direction} \\
&V_n = u \cdot e_x + v \cdot e_y + w \cdot e_z \quad ; \text{Normal velocity of surface}
\end{aligned}
\tag{4-7}
$$

Then transformation is applied from *P, Q, R* tangent velocities to *u, v and w* Cartesian velocities as follows:

$$
\begin{aligned}
u &= P \cdot p_x + Q \cdot q_x + R \cdot r_x \\
v &= P \cdot p_y + Q \cdot q_y + R \cdot r_y \\
w &= P \cdot p_z + Q \cdot q_z + R \cdot r_z
\end{aligned}
\tag{4-8}
$$

Finally pressure is calculated by solving the normal momentum equation:

$$\left\{\frac{p_x \cdot r_x + p_y \cdot r_y + p_z \cdot r_z}{r_x^{\,2} + r_y^{\,2} + r_z^{\,2}}\right\} P'_p + \left\{\frac{q_x \cdot r_x + q_y \cdot r_y + q_z \cdot r_z}{r_x^{\,2} + r_y^{\,2} + r_z^{\,2}}\right\} P'_q + P'_r =$$
$$\cdots \quad \cdots \qquad -\frac{\rho P\left(r_x \cdot u_p + r_y \cdot v_p + r_z \cdot w_p\right) + \rho Q\left(r_x \cdot u_q + r_y \cdot v_q + r_z \cdot w_q\right)}{r_x^{\,2} + r_y^{\,2} + r_z^{\,2}} \tag{4-9}$$

This equation can be written in simpler form as follows:

$$\begin{aligned}
&D_1 \cdot P'_p + D_2 \cdot P'_q + P'_r = R \\
&D_1 \cdot P'_p + D_2 \cdot P'_q + \frac{(P'(r+1) - P'(r))}{\Delta r} = R \\
&D_1 \cdot \Delta r \cdot P'_p + D_2 \cdot \Delta r \cdot P'_q - P'(r) = R \cdot \Delta r - P'(r+1) \\
&-\hat{D}_1 \cdot P'_p - \hat{D}_2 \cdot P'_q + P'(r) = \hat{R} \\
&\textit{where} \quad \hat{D}_1 = D_1 \cdot \Delta r, \quad \hat{D}_1 = D_1 \cdot \Delta r, \quad \hat{R} = -R \cdot \Delta r + P'(r+1)
\end{aligned} \tag{4-10}$$

As a result, formulation is converted to approximate factorization with equations below and consecutive closed solution with pressure solutions are obtained in two directions.

$$(I - \hat{D}_1 \delta_p) \cdot (I - \hat{D}_2 \delta_q) \cdot P'(r) \cong \hat{R} \tag{4-11}$$

4.3.2 Symmetry Boundary Condition

Symmetry boundary condition is used when the 3D flow solver is used for 2D test cases. The idea of using the symmetry boundary condition is *to tell* the solver that at these types of boundaries, all flow and geometric properties are the same from this boundary on. This is just like having 2D airfoil experiments in a real 3D wind tunnel. There, one uses the same airfoil geometry from one wall to the other.

Symmetry boundary condition is imposed on a boundary that's depicted in Figure 17. Symmetry condition implies equality in all scalar values:

$$\rho_1 = \rho_3, \quad e_1 = e_3, \quad P_1 = P_3 \tag{4-12}$$

Velocity vectors are evaluated as follows:

$$\begin{aligned} u_1 &= u_3 - 2 \cdot \hat{r}_x \cdot \overline{U}_3 \\ v_1 &= v_3 - 2 \cdot \hat{r}_y \cdot \overline{U}_3 \\ w_1 &= w_3 - 2 \cdot \hat{r}_z \cdot \overline{U}_3 \\ where \quad \overline{U}_3 &= \vec{U}_3 \cdot \vec{n} = \vec{U}_3 \cdot \frac{\nabla r}{|\nabla r|} \end{aligned} \tag{4-13}$$

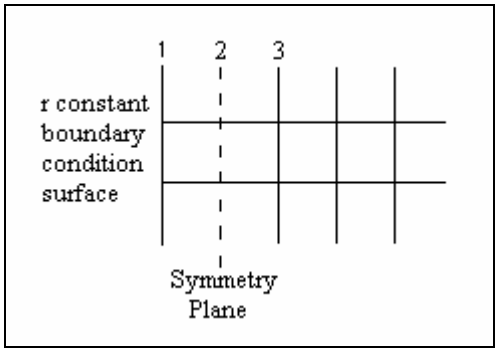

Figure 17 Symmetry plane

4.3.3 Periodic (Matching) Boundary Condition

In analyzing the flow through an entire blade row it is usually assumed that the flow fields in all of the passages between the blades are identical. In this way one can compute the flow through a single passage, rather then through the entire annulus. In computing the flow through only a single passage one must apply periodic (matching) boundary condition on those portions of the boundary of the grid that lie in the interface between adjacent passages.

In TAINS-103, periodic boundary condition can be given using a special form of the existing matching boundary condition. The variations of the matching boundary condition are obtained by the various use of the parameters given in Table 7.

Table 7 Parameters of matching boundary condition

IEXTRP	Extrapolation type 0 → Data transfer only 1 → Interpolation with both surface inners and one point each 2 → Interpolation with both surface inners and 5 points each 3 → Interpolation with both surface inners and 9 points each Interpolation types are displayed in Figure 18.
ITKGV	A parameter that specifies active, passive and data transfer of this boundary condition. 0 → Declares that this boundary type is fully passive and defines only regions to the cross boundary condition. 1 → Receives data only from region across. 2 → Receives data from region across and returns calculating cross-value also.

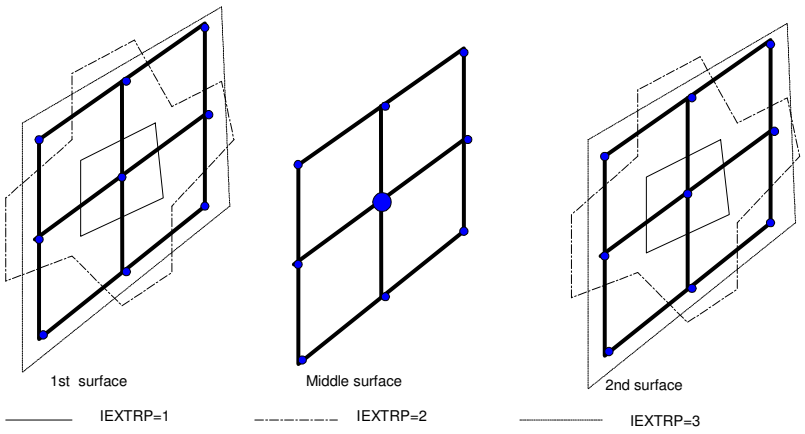

Figure 18 Interpolation types

Inverse distance method is used between these points for interpolation. Interpolation formulation of inverse distance method with m points is given below:

$$f(A,B)=\frac{1}{\overline{A}\overline{B}^{\alpha}} \quad \Rightarrow \quad g_i(A)=\frac{\sum_{n=1}^{m} f(A,B_n)\cdot g(B_n)}{\sum_{n=1}^{m} f(A,B_n)} \tag{4-14}$$

4.3.4 Inlet Boundary Condition

At the inlet boundary all variables are given. The velocity distribution at the inlet is known from design. These variables are kept constant at each time step in order the flow field to converge to the given velocity distribution.

4.3.5 Outlet Boundary Condition

Generally speaking, the value of the velocity and pressure are not known at the outflow boundary. So for most applications, specification of the velocity vector is not quite possible. However, for some applications (including the present study) where the outlet is known to be subsonic, static pressure may be given at the outlet boundary. This must be done regarding the physics of the flow.

In the present study, one-dimensional characteristics are used in the normal direction to the outlet boundary. The idea is to extrapolate the velocity field from the interior without losing the physics by making use of the characteristics of the governing equations and the static pressure distribution given externally.

The method is described below. The outlet boundary is depicted in Figure 19.

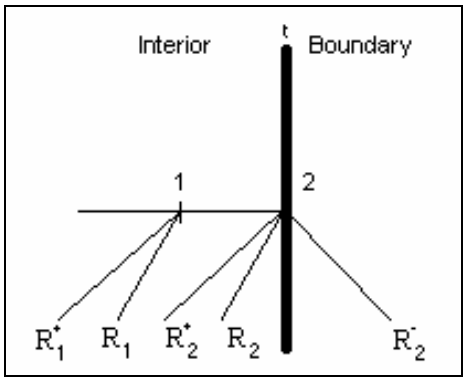

Figure 19 Outlet boundary

As can be seen in Figure 19 the notation that will be used throughout this section is as follows:

1: interior point

2: boundary point

All variables at 1 are known (ρ_1, u_1, v_1, w_1, e_{t1}).

From the known variables pressure is calculated:

$$p_1 = (\gamma - 1)\left[e_{t,1} - \tfrac{1}{2}\rho_1\left(u_1^{\,2} + v_1^{\,2} + w_1^{\,2}\right)\right] \tag{4-15}$$

Also speed of sound at the interior point is calculated:

$$a_1 = \sqrt{\gamma \frac{p_1}{\rho_1}} \tag{4-16}$$

Next, the Riemann invariants (characteristics) that run from point 1 to point 2 are calculated:

$$R_1 = \frac{p_1}{\rho_1^{\gamma}}$$
$$R_1^{+} = u_1 + \frac{2a_1}{\gamma - 1} \tag{4-17}$$

It is given in detail in (Hirsch Ch., 1990) that R_1 and R_1^+ are constant on their characteristic lines. So,

$$R_1 = R_2$$
$$R_1^{+} = R_2^{+} \tag{4-18}$$

So now one can find ρ_2 or p_2, by specifying the other and using equations (4-17) and (4-18). In the present study static pressure (p_2) is specified externally.

Once the density at point 2 is found, speed of sound can be found using equation (4-16).

Then using the definition of speed of sound in terms of Riemann invariants at point 2, and using equation (4-18) one can find the third Riemann invariant as follows:

$$R_2^{-} = R_1^{+} - 2a_2 \frac{2}{\gamma - 1} \tag{4-19}$$

Then the velocity at point 2 can be extracted using the definition of R_1^- as follows:

$$u_2 = R_2^{-} + \frac{2}{\gamma - 1} a_2 \tag{4-20}$$

Since one-dimensional characteristics method is used here, the velocities in the other two directions are taken to be the same.

4.3.6 Boundary Conditions Input File

Input file is considered to be systematic and flexible suitable again for the general purposes. First of all, in account for flexible file location definition, a constant name file (“INITIAL”) points out the name and location of the main input file. That input file has a higher order language structure so that it requires command code definitions. It consists three main parts (NAMELIST structure of FORTRAN) in which the first part contains definitions of general parameters under title (“GENEL”); the second part contains general block parameters (“BLGENEL”). Also physical definitions of flow can be given separately for each block. The parameters in this part, can be listed as block numbers, flow conditions, parameters of time integration, alternative formulae, solution control parameters and grid dimensions. The third part (“BOCN”) is the region where boundary conditions are defined one by one. In this part, inputs can be classified into the two: general information namely, block number, boundary condition number, boundary condition type and flow region location; and parameters specialized for that boundary conditions. All parameters are displayed in Table 8. Detailed information about these parameters are given in the following sections.

Table 8 Definitions of input parameters

GENEL	
TITLE	Project name
NBL, NMAX, NP	Block number iteration number and record interval respectively
IREAD, IWRIT	Parameters of reading and writing types
BLGENEL	
NoBL, MxNBC	Block number and maximum boundary condition number
BLKNM, GRDFNAMES	Block name and grid filename
FSMACH, RE, ALP,BET, PR	Free-stream values (Mach, Reynolds, attack angle, side-slip angle, Prandtl number).
INVISC, LAMIN	Inviscid or viscous and Laminar or turbulent selections
CNBR, DT	Values related with time integration (Courant number, time step)
ILHS,IRHS, IROE, ISTD,SMU	Alternative solution selection parameters
JMAX,KMAX,LMAX,CR,SREF	Grid dimensions (Max. number of points in J,K,L index directions, reference location and area
BOCN	
IBCTYPE	Boundary condition type selection parameter
LB, NDIR	Definition of indexes and position and
NoBL, NoBC	Block number where the boundary condition belongs to and boundary condition number
IBLOPT, IBLTYPE, UINLET	Flow input parameters
UOUTLET	Flow output parameters
UWALL,VWALL,WWALL	Velocities at wall
IEXTRP,ITKGV,NoBLC,NoBCC LOCOPT	Matching boundary condition parameters (Interpolation type, transfer definition, block number and boundary condition number of matched boundary condition respectively…)

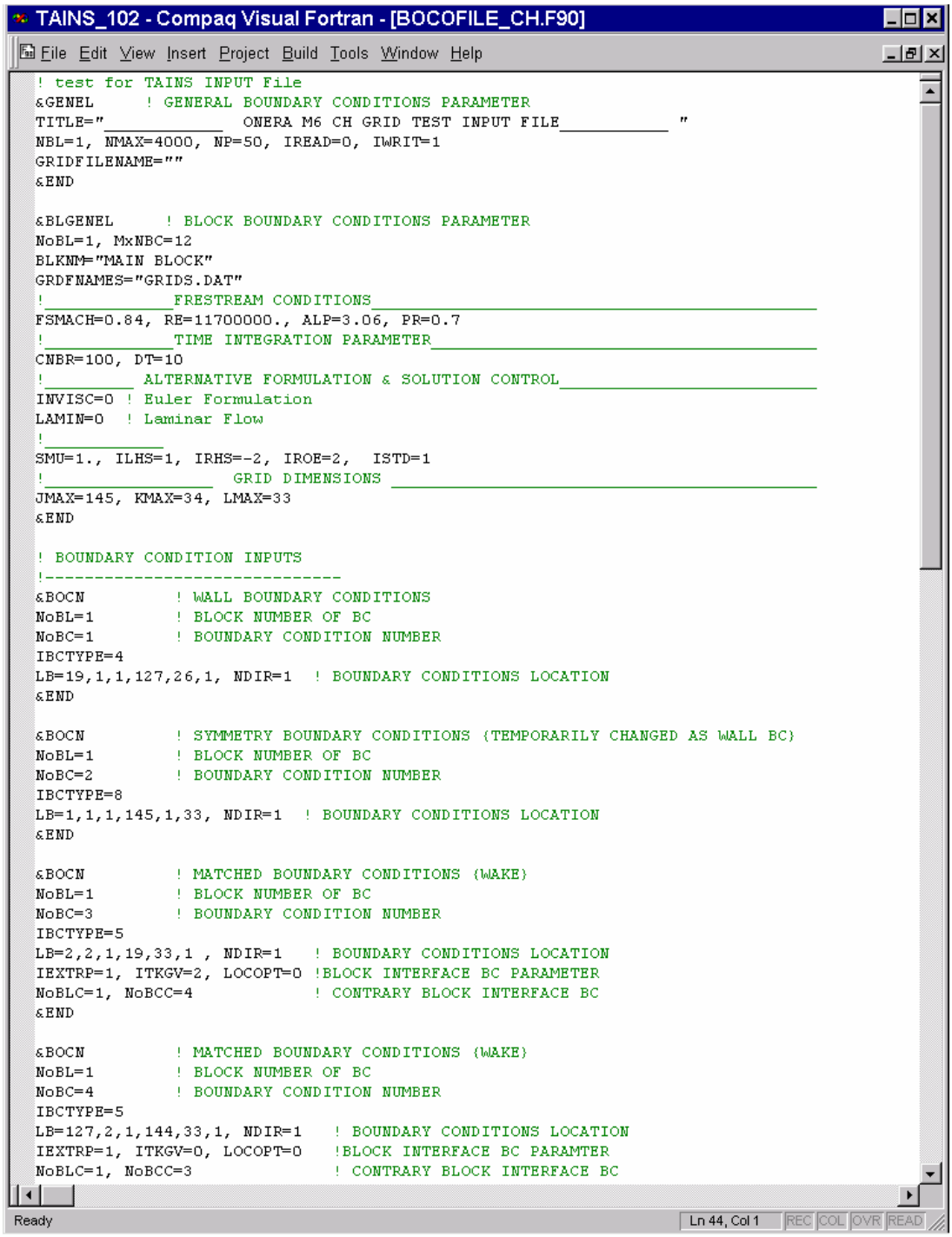

Figure 20 An example boundary condition input file

4.3.7 Boundary Condition Set Used in the Present Study

In the present study the boundary condition set used for 3D applications includes:

i. Inlet

ii. Wall

iii. Periodic

iv. Outlet

Boundary conditions.

However, for 2D applications, in addition to wall, periodic, inlet and outlet boundary conditions; symmetry boundary condition is also applied.

The boundaries on which wall and periodic boundary conditions applied are depicted in Figure 21 below.

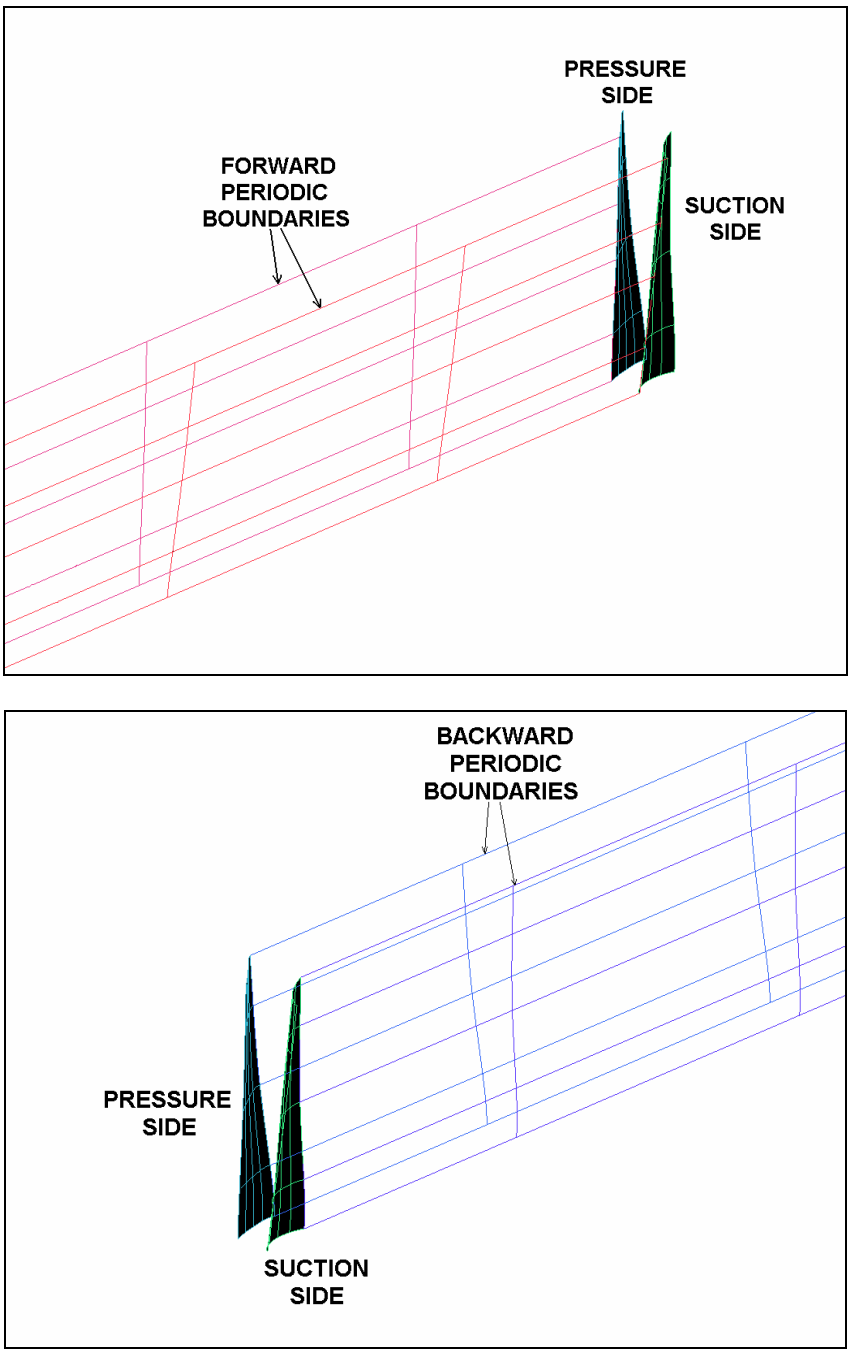

Figure 21 Regions of the solution domain where periodic boundary condition is applied. Top: Forward periodic boundaries. Bottom: Backward periodic boundaries.

4.4 Grid Generation

Before generating a numerical solution to the partial differential equations that govern the fluid flow, the physical domain must be discretized. That is, a grid should be generated around a body to resolve the necessary flow gradients. The discretization may be based on structured or unstructured concepts. In a structured grid, points are arranged so that their relative positioning in physical space is preserved in their computational storage; i.e., points adjacent to a given point in physical space are also adjacent in computational space. On the other hand, there is not necessarily any correspondence between a points physical and computational neighbors in unstructured grids.

The finite difference method, using discrete points, is associated historically with rectangular Cartesian grids, since such a regular lattice structure provides easy identification of neighboring points to be used in the representation of derivatives. It is not, however, limited to rectangular grids and has long been applied on other analytical coordinate systems (i.e. cylindrical, spherical, elliptical etc.) that still form a regular lattice. These special curvilinear coordinate systems are all orthogonal, as are the rectangular Cartesian systems, and they also can exactly cover special regions in the same way that a Cartesian grid fills a rectangular region.

In the present study, a grid generation program is used to generate structured grids. The details of the program package and grid generation process are given below.

As stated above, the solver used in the present study is a finite difference based one. So the grid used is a structured one. The program is a 3D, object-based, multi-block, structured, surface and volume grid generator. The block topology model is generated directly on the underlying CAD geometry. The user has access on two types of entities during the grid generation process: block topology and geometry. After creating a 3D block

topology model equivalent to the geometry, that block topology may be further refined through the splitting of edges, faces and blocks. In addition, there are tools for moving the block vertices, individually or in groups, onto associated curves or CAD surfaces. One may also associate specific block edges with important CAD curves to capture important geometric features in the grid. Moreover, for models where the user can take advantage of symmetry conditions, topology transformations such as translate, rotate, mirror and scaling are available.

The grid generation program provides a projection based grid generation environment where, by default, all block faces between different materials are projected to closest CAD surfaces. Block faces within the same material may also be associated with specific CAD surfaces to allow for definitions of internal walls.

The grid generation strategy followed in the present study is given below:

1. Import the geometry file created with computer aided design (CAD) code, in IGES format.
2. Group and name related curve and surface families (i.e. like the pressure side of the blade).
3. Run structured grid generation tool.
4. Interactively define the block model through split, projection, edge/face modifications and vertex movements.
5. Assign edge meshing parameters such as number of elements on edges, initial element sizes and expansion ratios.
6. Generate the mesh with projection parameters specified.
7. Check mesh quality to ensure that the intended grid quality criteria are met.

8. If the grid quality to do not meet the intended quality criteria or the grid does not capture certain geometry features, then go back and manipulate the block via further splitting, projection and/or smoothing.
9. Repeat step 8 until the grid is good enough.
10. Perform grid scaling and i, j, k re-ordering if necessary.
11. Write Output files for the solver.

Even though it is hard to understand any 3D grid on a 2D paper, an example grid that's used in the present study is given in Figure 22 below.

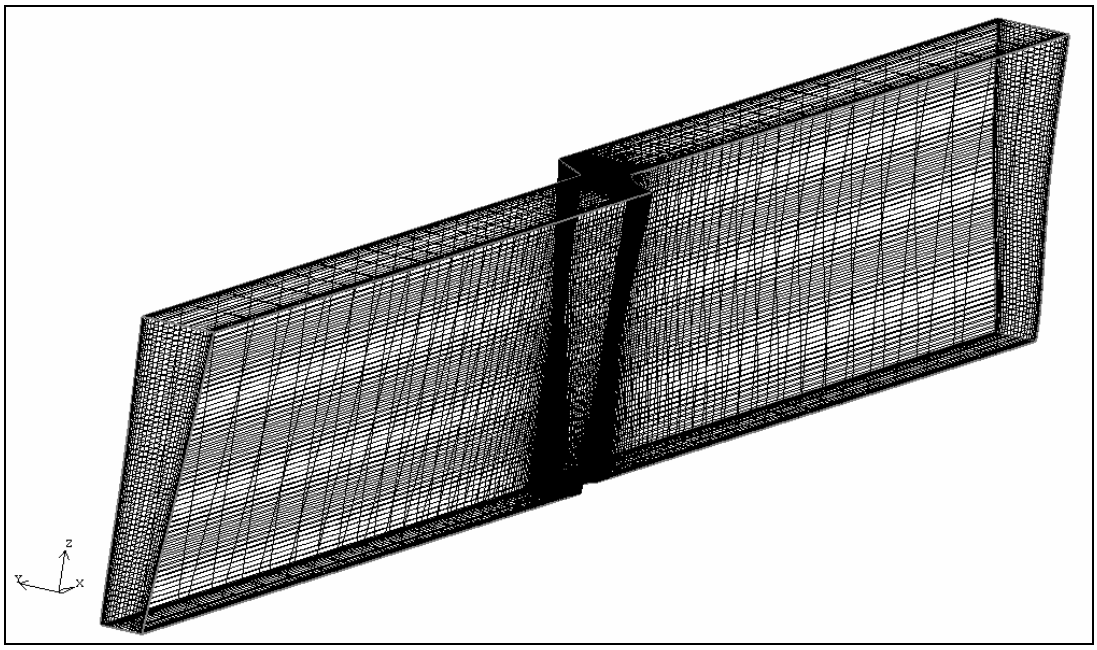

Figure 22 A perspective view of the solution domain

Another important feature of the grid structured generation is to apply smoothing on the grid. In the present study smoothing is applied on any grid that's used via manipulating the interior edges that are normal to the blade surfaces at different radial locations. What is meant can better be

understood by an example. In Figure 23, grid generated at one radial location is given with and without smoothing applied.

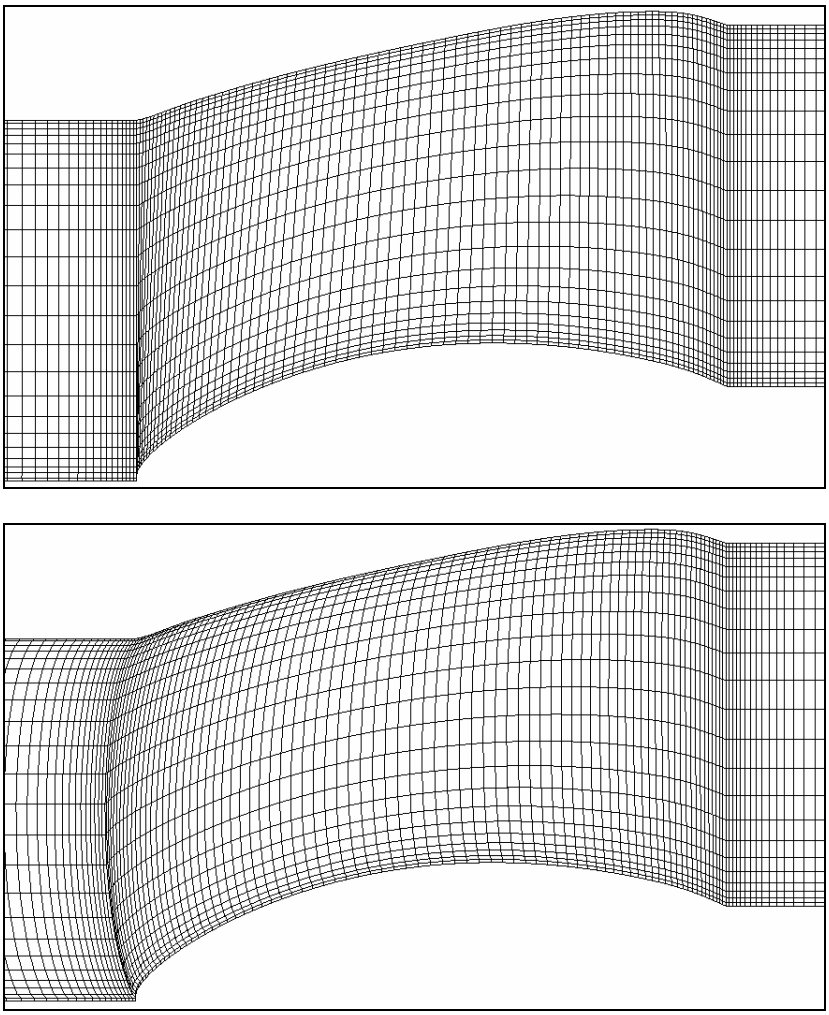

Figure 23 The effect of grid smoothing. Top: Grid before smoothing. Bottom: Grid after smoothing. Notice the difference in grid quality after the smoothing operation.

CHAPTER 5

NUMERICAL RESULTS

5.1 Introduction

The main purposes of this chapter are to present the validity of the CFD code used in the present study and to present the 3D CFD analysis results of the design made in this study.

5.2 Validation and Verification Test Cases

There are three test cases given below. The first one is an external flow application. Second is an internal flow application with high flow turning. The last one is a rotational external flow application (i.e. flow around a rotating cylinder.)

5.2.1 Test Case I – AGARD AR138 Onera M6 Wing

This test case is an external flow application. That is to say, an aircraft wing with airfoil section ONERA M6 is analyzed using the solver used in the present study originally (i.e. TAINS–103). See (Sergen Ş., et. al., 2003) for additional information on the computer program TAINS-103.

In 1972, the ONERA aerodynamics department designed a swept back wing to be used as an experimental support for basic studies of three-dimensional flows at high Reynolds number from low to transonic speeds.

In (Schmitt V. et al., 1979) experimental data obtained at ONERA S2MA wind tunnel at Mach numbers of 0.7, 0.84, 0.88 and 0.92 for angles of attack up to 6° and a Reynolds number of about 12 million is presented.

In this test case, 3D Euler solution for a flight Mach number of 0.7 and angle of attack of 3° is investigated. An C-O type grid is used as shown in Figure 24 below. This computational grid has 165x45x31 nodes (i.e. around 230000).

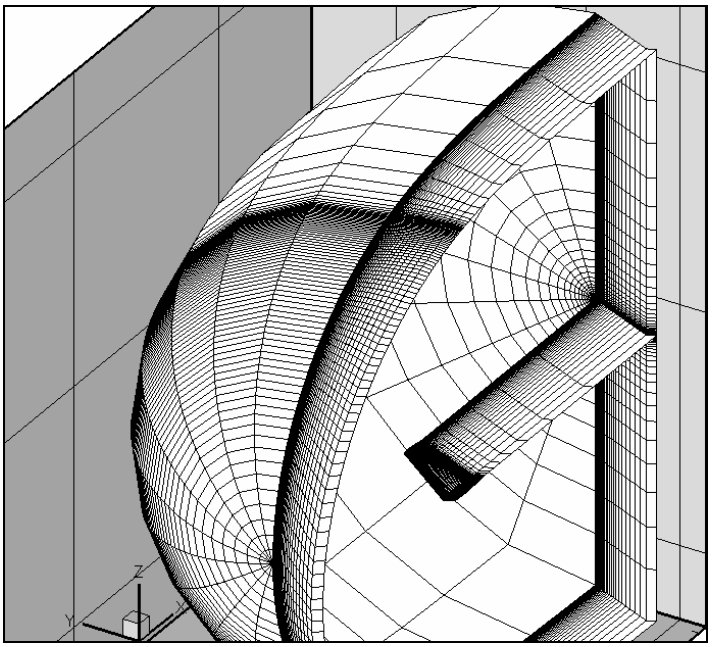

Figure 24 C-O type computational grid for the test case I.

The experimental data is given in terms of surface pressure distributions at different sections. Numerical results at three sections are compared with experimental results in Figure 25, Figure 26 and Figure 27 below. The convergence history of the solution is also given in Figure 28 at the end.

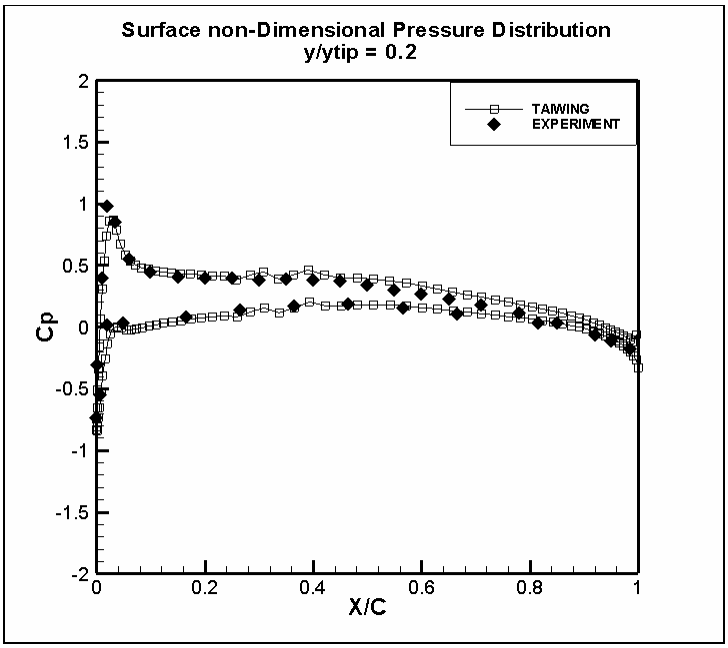

Figure 25 Numerical results vs. experiment at y/y_{tip} 0.2.

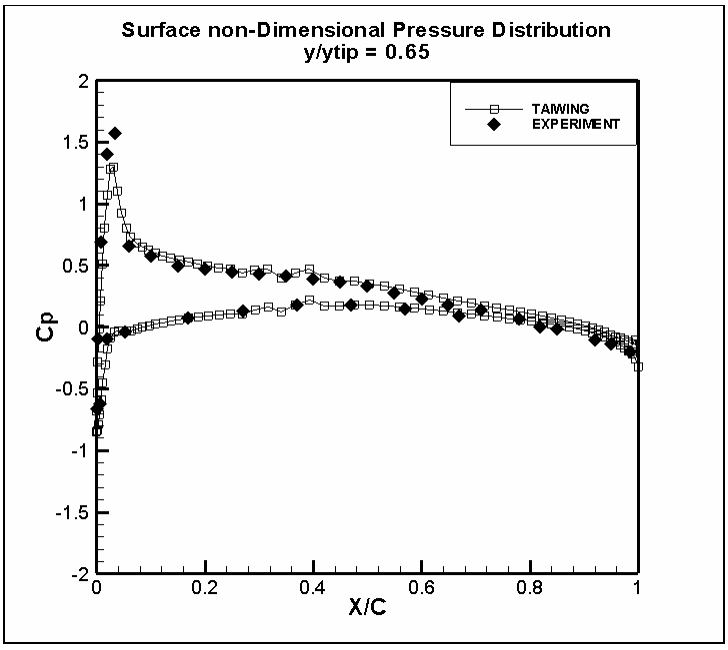

Figure 26 Numerical results vs. experiment at y/y_{tip} 0.65.

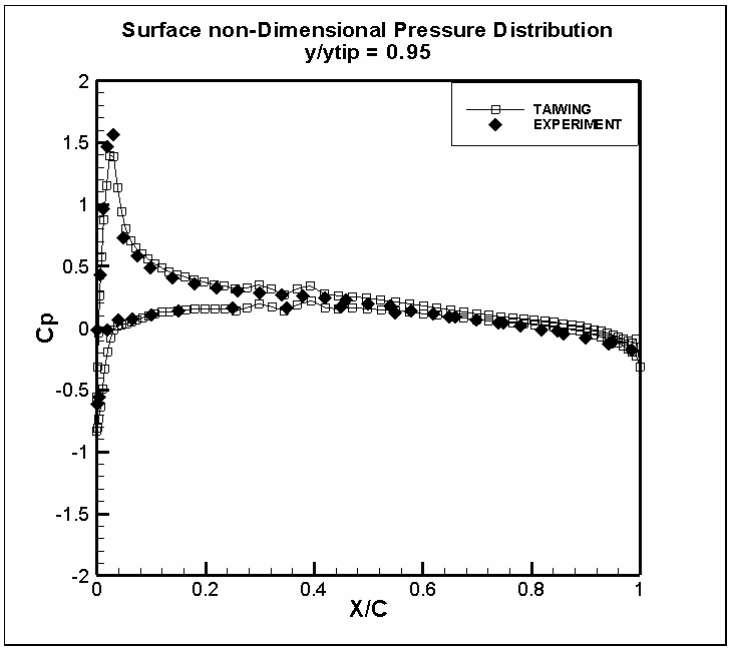

Figure 27 Numerical results vs. experiment at y/y_{tip} 0.95.

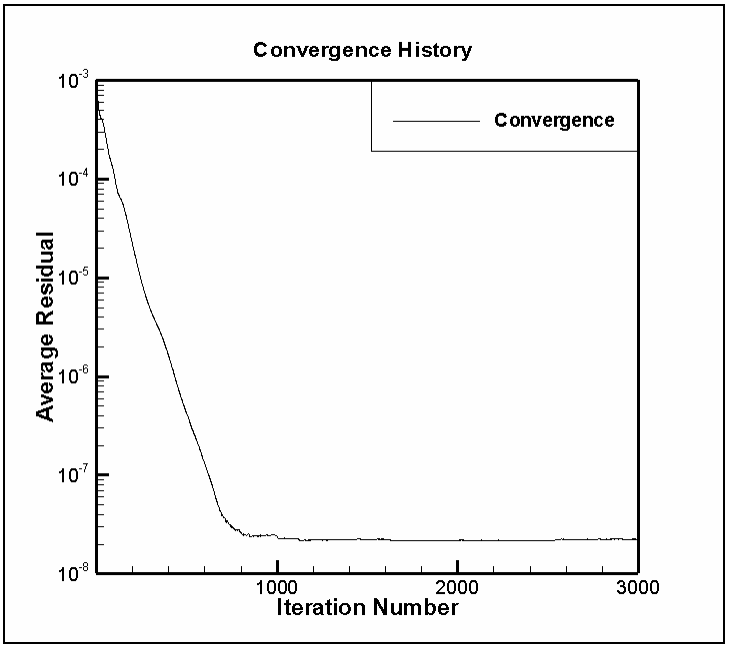

Figure 28 Convergence history of test case I.

5.2.2 Test Case II – AGARD AR 275 High Subsonic Compressor Cascade

This test case is an internal flow application. The blade geometry that is investigated experimentally, as shown in Figure 29, is analyzed by the current solver used in the present study.

The test case concerns the experimental investigation of a 2D compressor cascade at two inlet Mach numbers (i.e. 0.7 and 0.85) and four values of flow angles, β (i.e. 49°, 51°, 53° and 55°).

This blade cascade is designed to achieve a flow turning angle larger than 50° in a two-dimensional flow. The corresponding diffusion is high and the blade shapes were tailored to minimize the suction side over-expansion and to ensure a recompression without flow separation at the design conditions.

Moreover, a large number of boundary layer measurements and a few but enough static pressure - relative to inlet total pressure - distributions are given in (Meauzé G. et al., 1990). Hence, the physics of this problem needs a Navier-Stokes analysis. However, at least the static pressure distributions are attempted to be solved with the current Euler solver.

In this test case, 3D Euler solver is used as a 2D solver by making use of symmetry boundary condition described in Chapter 3 and the problem of inlet Mach number 0.7 and of incidence 49° is investigated. The blade geometry is given in Figure 29 and the corresponding computational grid used in this test case is given in Figure 30 below. This computational grid has 298x50 nodes in 2D (i.e. around 14900).

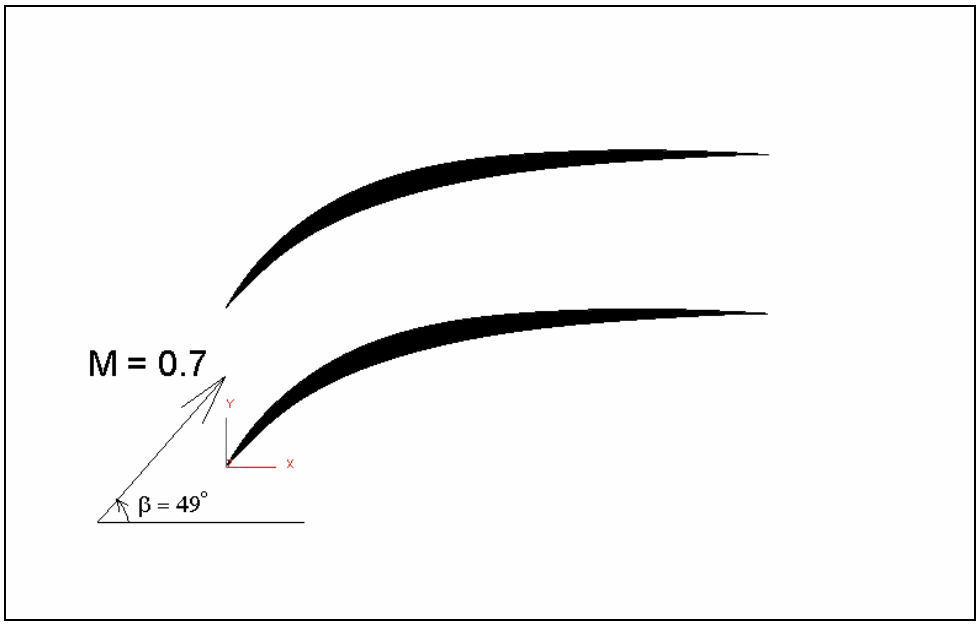

Figure 29 Blade geometry

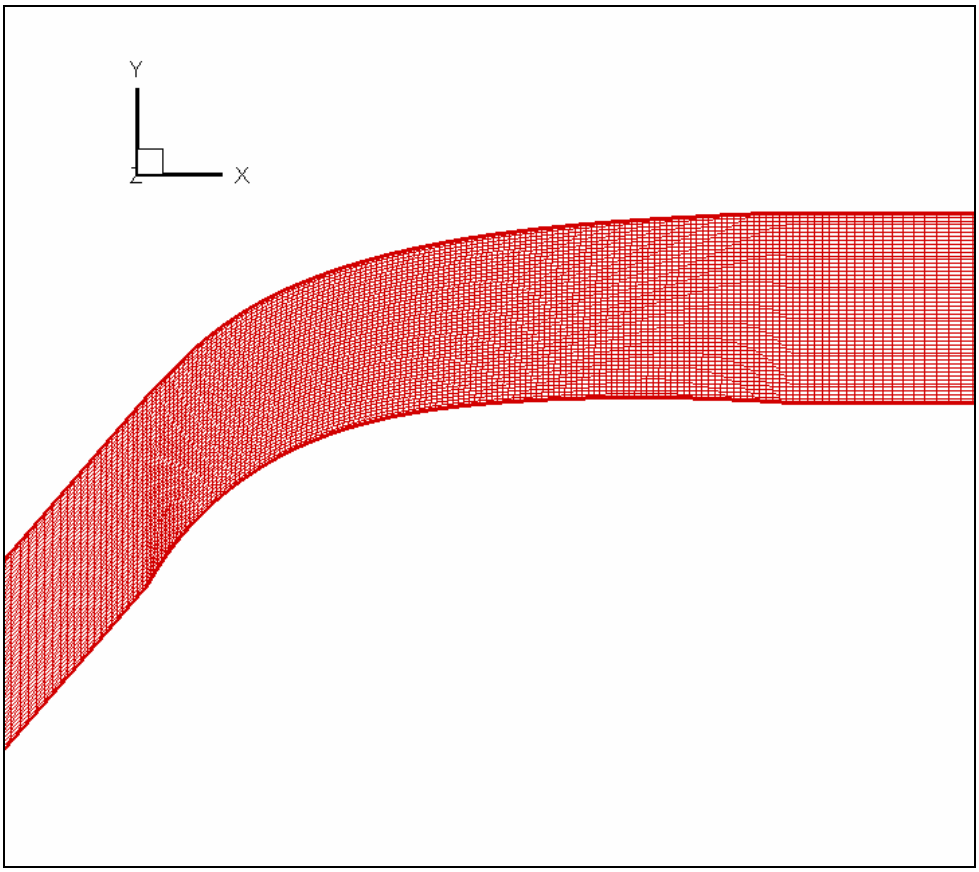

Figure 30 Computational grid 298x50

The velocity vector field and the static pressure contours of the converged solution are given in Figure 31 and Figure 32 respectively. The comparison of the non-dimensional static pressure distributions on suction and pressure sides of the converged solution with experimental data is given in Figure 33 below. Convergence history is given at the end.

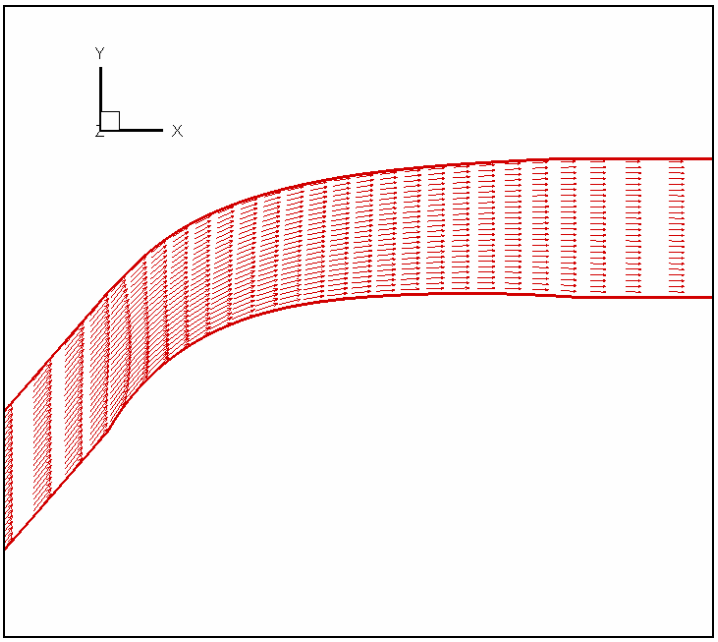

Figure 31 Velocity vector field of the converged solution.

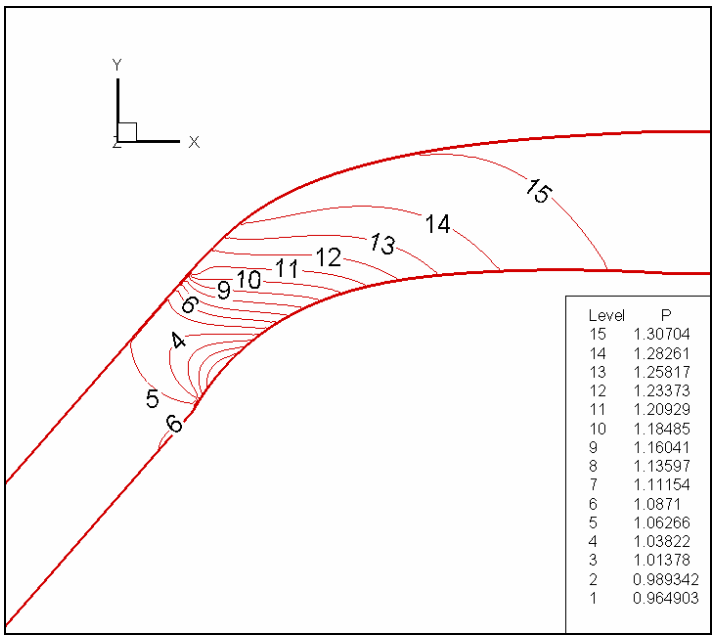

Figure 32 Static pressure contours of the converged solution

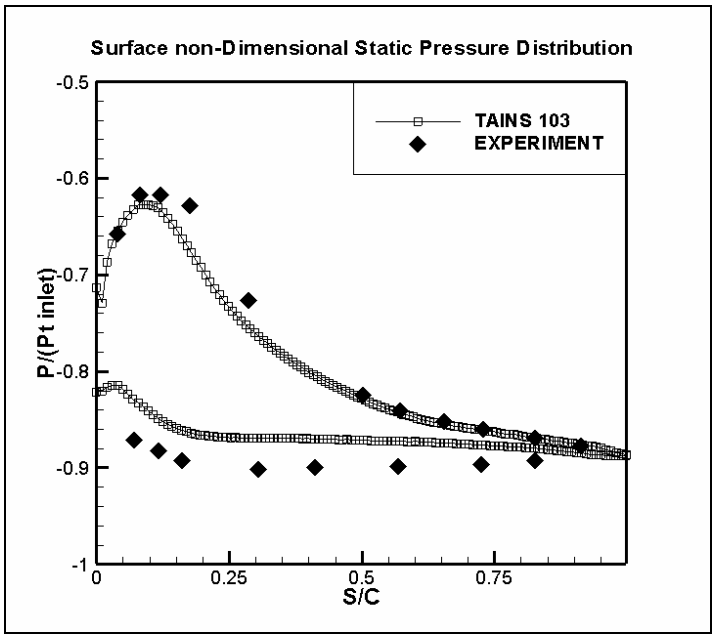

Figure 33 Comparison of the numerical results with experimental data.

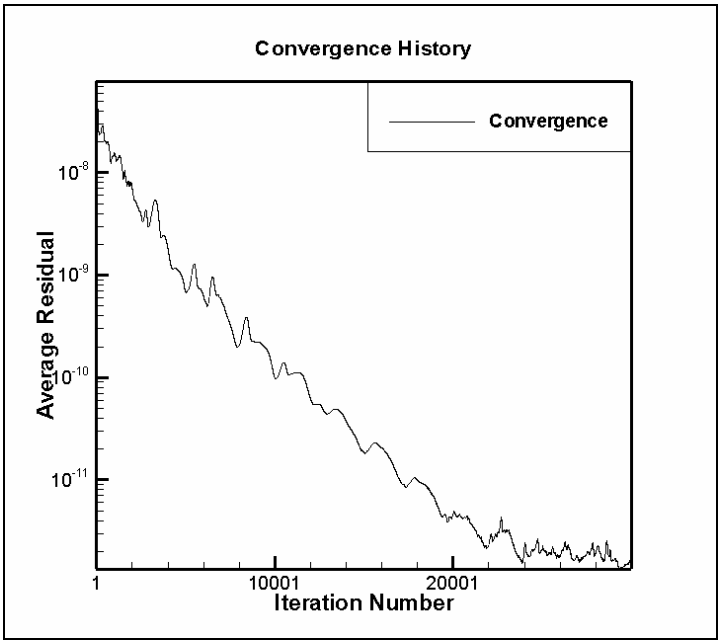

Figure 34 Convergence history of test case II.

5.2.3 Test Case III – Flow Around Rotating Cylinder (Magnus Effect)

This test case is a rotational external flow application. Flow over a rotating cylinder of radius R may be given as the superposition of a uniform flow around the cylinder with a vortex of strength Γ located at the center of it as shown in Figure 35 below.

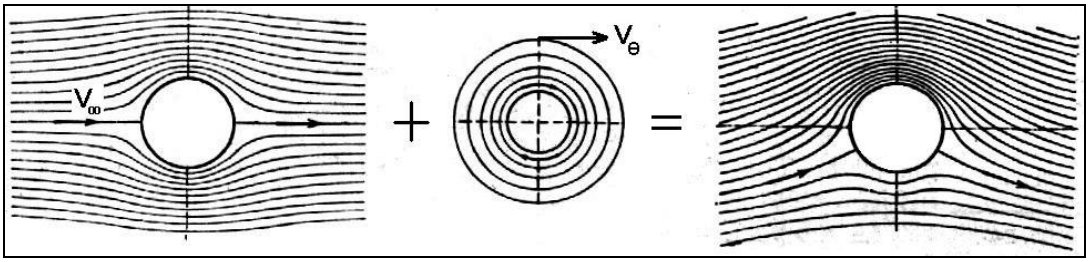

Figure 35 Flow around a rotating cylinder.

For such a case the exact solution of the flow field is possible and is given by the following stream function (Anderson J.D., 1991):

$$\psi = (V_\infty r \sin\theta)\left(1-\frac{R^2}{r^2}\right)+\frac{\Gamma}{2\pi}\ln\frac{r}{R} \tag{5-1}$$

For such a solution, the radial and tangential velocity distributions can be found:

$$V_r = \left(1-\frac{R^2}{r^2}\right)V_\infty \cos\theta \tag{5-2}$$

$$V_\theta = -\left(1+\frac{R^2}{r^2}\right)V_\infty \sin\theta - \frac{\Gamma}{2\pi r} \tag{5-3}$$

Equating both equations (5-2) and (5-3) to zero one can find the stagnation points at r=R (i.e. on the surface of the cylinder). By doing so:

$$\theta = \sin^{-1}\left(-\frac{\Gamma}{4\pi V_{\infty} R}\right) \tag{5-4}$$

In the present study, a vortex of strength 0.12π, R=0.5 and V_{∞}=0.1 are used.

The results of the CFD calculation are given below. First the computational grid used is given. Then the results are given in terms of static pressure contours together with streamline pattern and compared with the exact solution. Finally the convergence history is given.

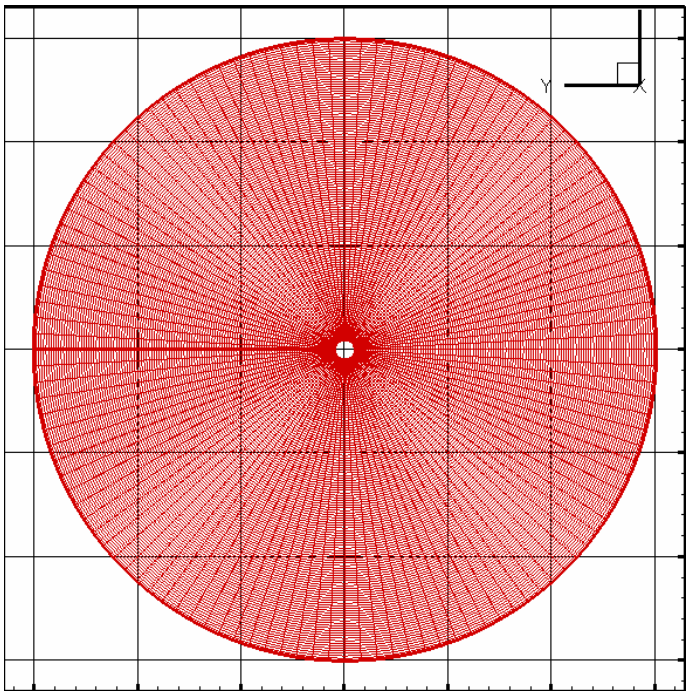

Figure 36 221x221 structured grid used in test case III.

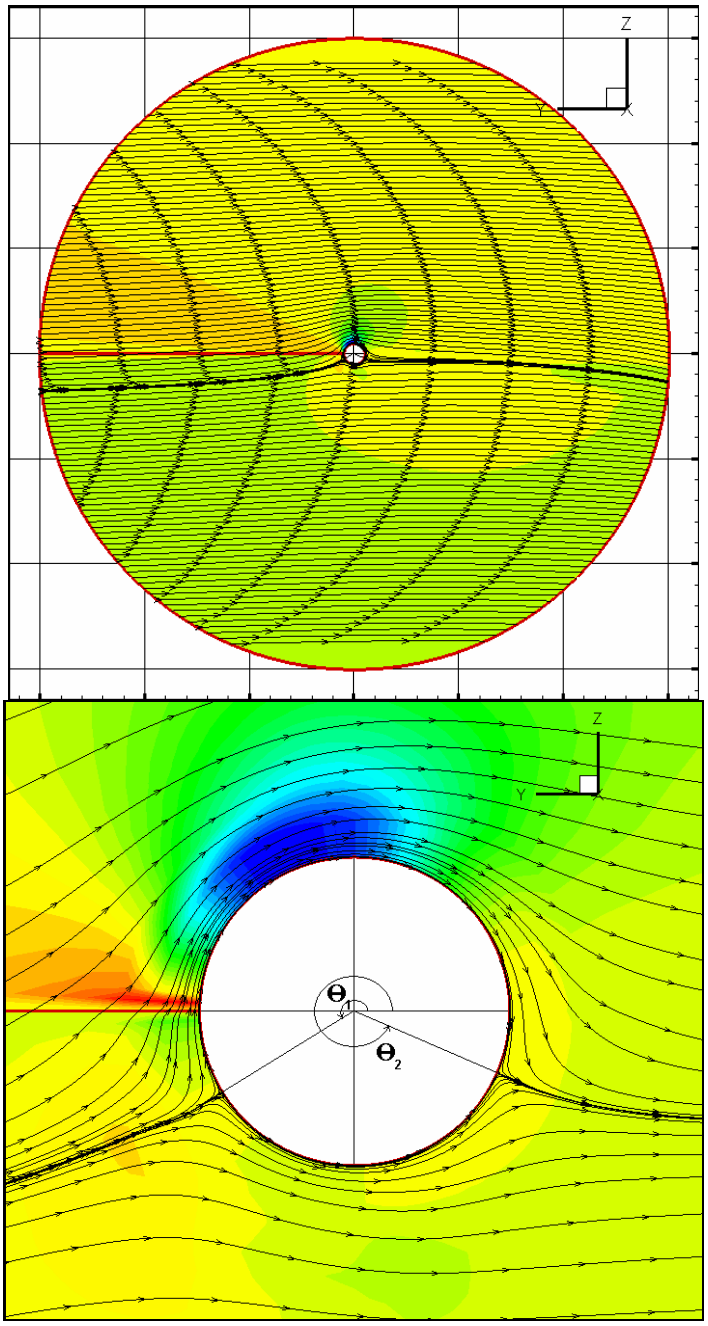

Figure 37 Flowfield around the cylinder. Top: Overview. Bottom: Zoomed view.

As can be seen from this figure, the static pressure difference (hence lift) occurs between the upper and lower parts.

The stagnation points obtained by this CFD solution can be compared by the ones computed with equation (5-4) by doing so:

Table 9 Comparison of analytical solution with CFD (stagnation points).

ANALYTICAL		COMPUTATIONAL	
θ_1=216.869898°	θ_2=323.130102°	θ_1=211.6771°	θ_2=336.4529°

Further comparisons may be applied for the analytical and computed radial and tangential velocities. To do this the velocities obtained by computation are compared by the ones obtained from equations (5-2) and (5-3) at one radius (i.e. r=0.8625) and four angles:

Table 10 Comparison of analytical solution with CFD (velocities).

	ANALYTICAL		COMPUTATIONAL	
θ=0°	V_r=0.0663936	V_θ=-0.069565	V_r=0.0140549	V_θ=-0.055988
θ=90°	V_r=0	V_θ=-0.203172	V_r=0.021643	V_θ=-0.191433
θ=180°	V_r=-0.0663936	V_θ=-0.069565	V_r=-0.1	V_θ=-0.069565
θ=270°	V_r=0	V_θ=0.0640412	V_r=0.0105857	V_θ=0.087676

The results are mostly in accordance with the exact solution. At some places there are relatively large differences however at places like θ=180° one component turns out to be exactly the same with the analytical solution.

The convergence history is given in Figure 38 below.

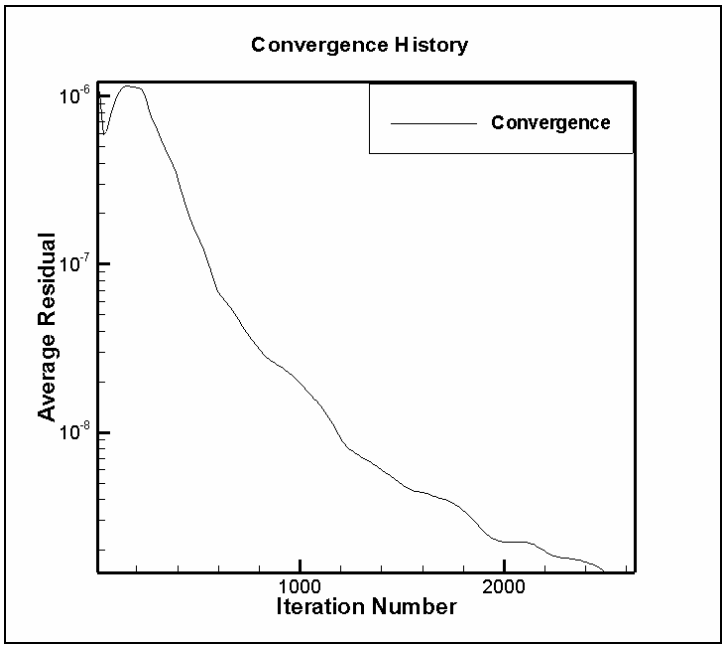

Figure 38 Convergence history of test case III.

5.3 3D CFD Analysis Results of the Present Design

In this section, the performance prediction of the design described in Appendix A and Chapter 2 using 3D Euler solver is given.

5.3.1 Grid Refinement

Given below the results of a grid refinement study carried on the grid shown in Figure 22. The grid refinement study consists of 6 grids ranging from a grid size of 98x24x30 (in x,y and z directions) to 298x60x100. All 6 grids were solved using TAINS – 103 with exactly the same boundary conditions in order to see only the effect of changing the number of grid size.

This section stands for the small loop depicted in the flowchart given in Chapter 2 (Figure 10 – lower left corner).

The results are compared in two variables, (i.e. Mach number and static pressure) at three radial locations (i.e. hub, mean and tip).

The reader may pay more attention on the last four solutions depicted by the colors black, green, purple and pink (i.e. 198x24x60, 198x48x60, 298x48x60 and 298x60x100 respectively).

The comments regarding the results are given at the end of each radial location (i.e. after giving both the Mach number and static pressure comparisons)

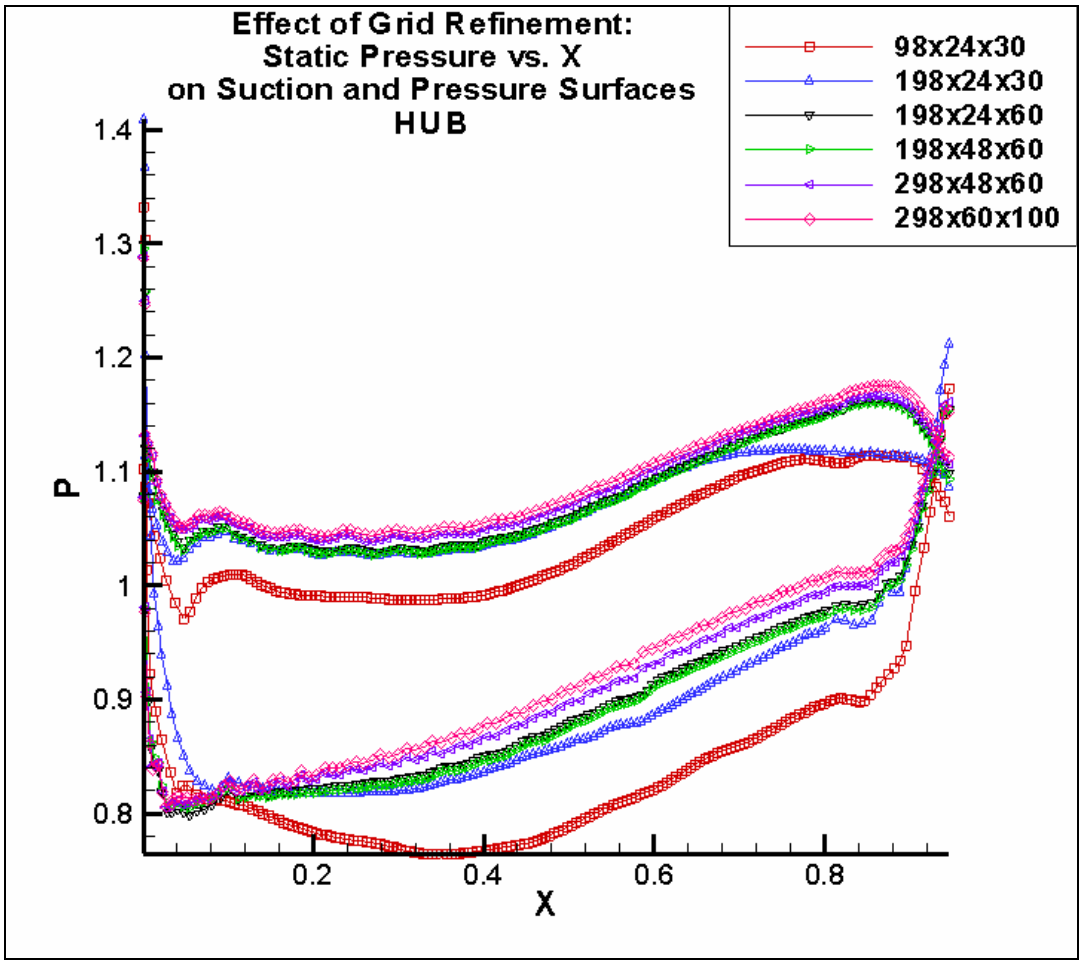

Figure 39 Effect of grid refinement 1: Comparison of static pressure on suction and pressure surfaces at hub location.

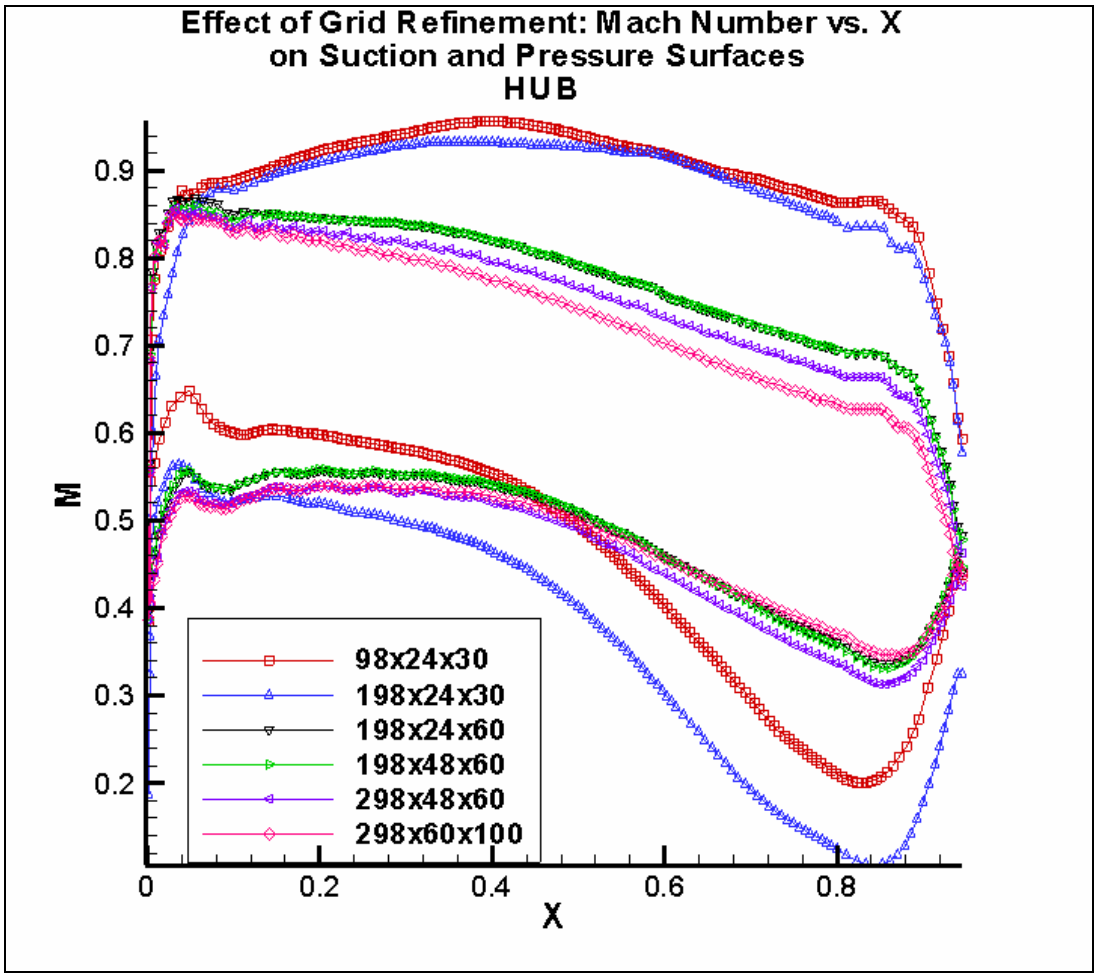

Figure 40 Effect of grid refinement 2: Comparison of Mach number on suction and pressure surfaces at hub location.

The results in hub region are in good agreement especially on the pressure side of the blade. At the suction side, there is slight variation among the last four solutions.

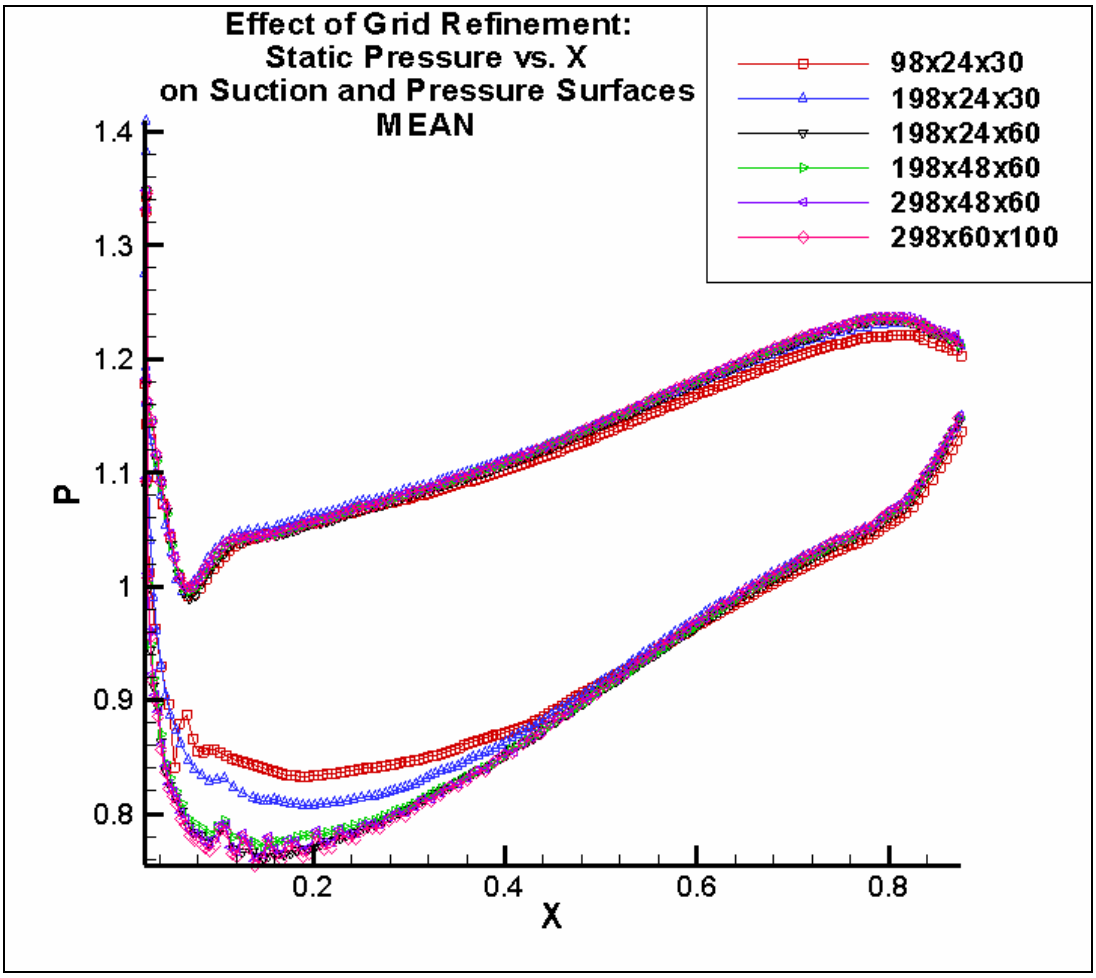

Figure 41 Effect of grid refinement 3: Comparison of static pressure on suction and pressure surfaces at mean line location.

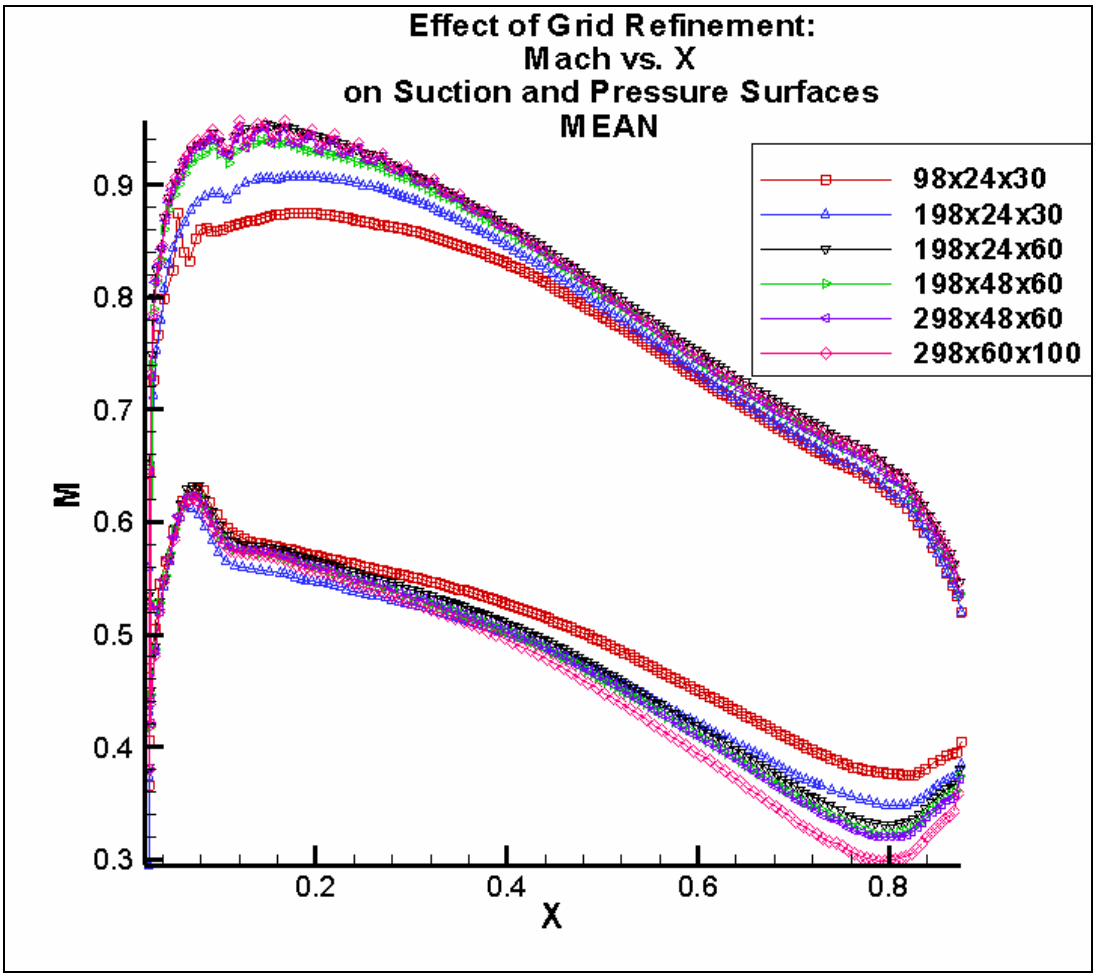

Figure 42 Effect of grid refinement 4: Comparison of Mach number on suction and pressure surfaces at mean line location.

The results in mean line region are in very good agreement on both pressure and suction sides of the blade.

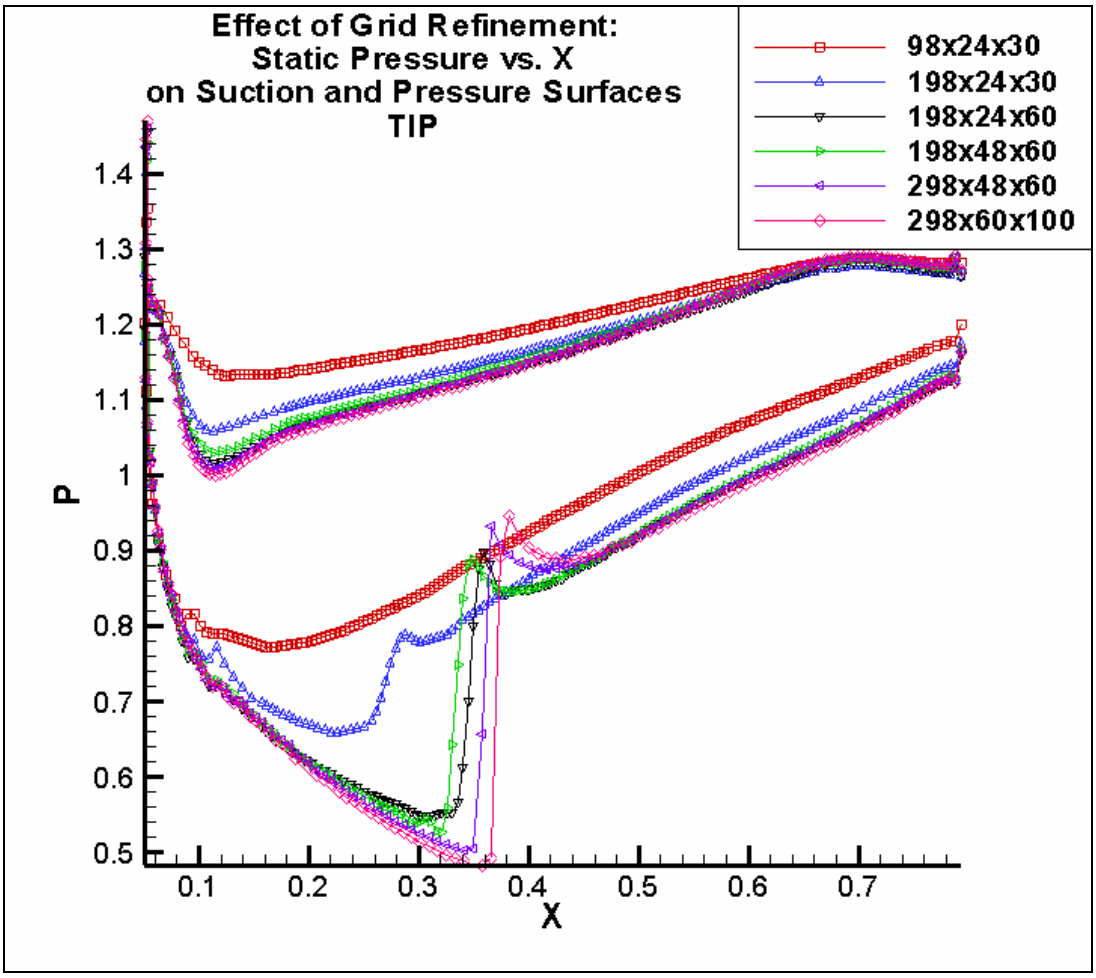

Figure 43 Effect of grid refinement 5: Comparison of static pressure on suction and pressure surfaces at tip location.

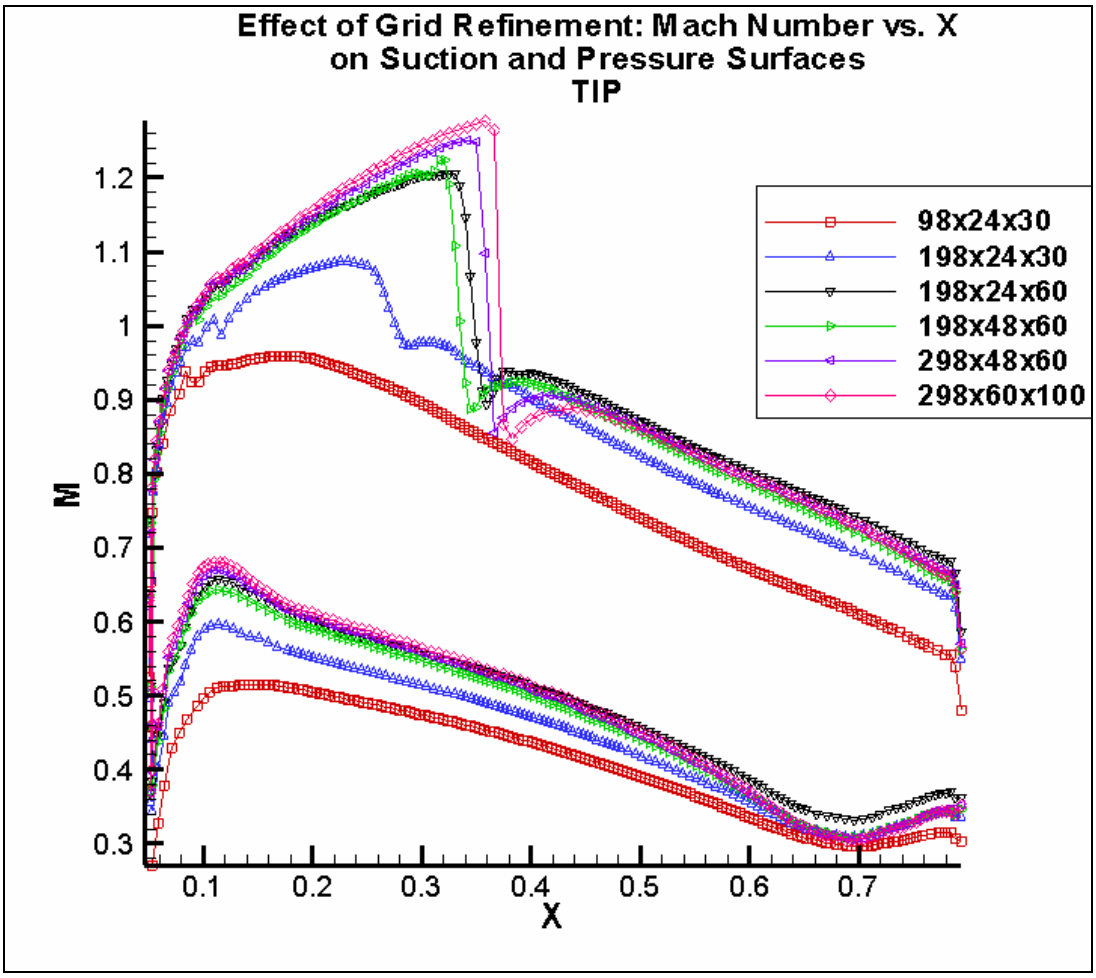

Figure 44 Effect of grid refinement 6: Comparison of Mach number on suction and pressure surfaces at tip location.

The results in tip region are also in very good agreement on the pressure side of the blade. On the suction side however, one can see the importance of this type of grid refinement work. There is a shock forming on the suction side at this radial location. However, the first solution can not capture the shock formation. Starting with the second solution, the shock formation is captured. The last four solutions have quite similar flow-field pattern before and after the shock. There is not an exact agreement on the location of the shock however.

5.3.2 Results

Having performed a grid refinement study, the results of the best solution (namely the solution of 298x60x100 grid) are presented below.

The results are presented in two parts and at three radial locations as before. The first part gives an idea about the velocity vector field by making use of Mach contours together with the streamline patterns.

The second part gives the static pressure and entropy contours.

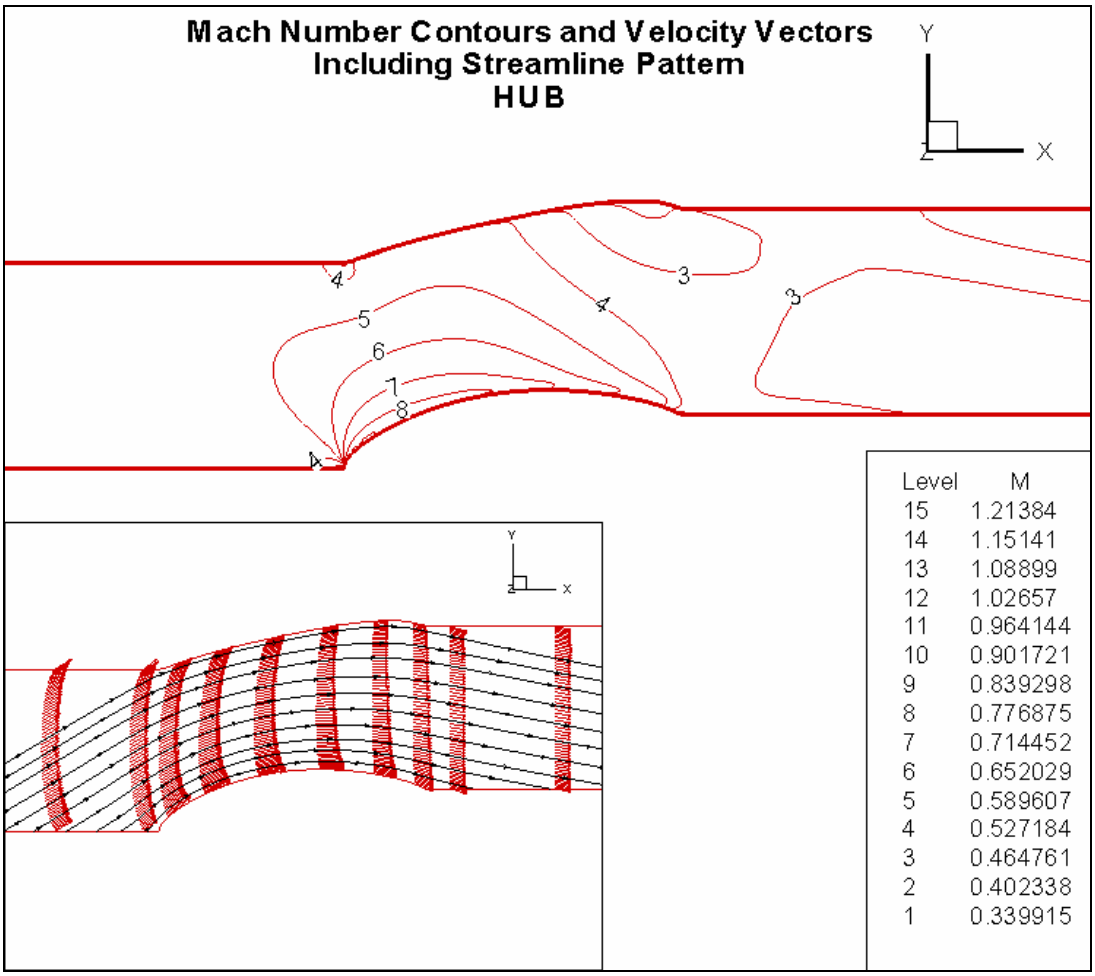

Figure 45 Results 1: Velocity vector field at hub location.

The flow pattern at hub region is as expected. The flow turning is 37.07° which is very close to the design value of 37.21°.

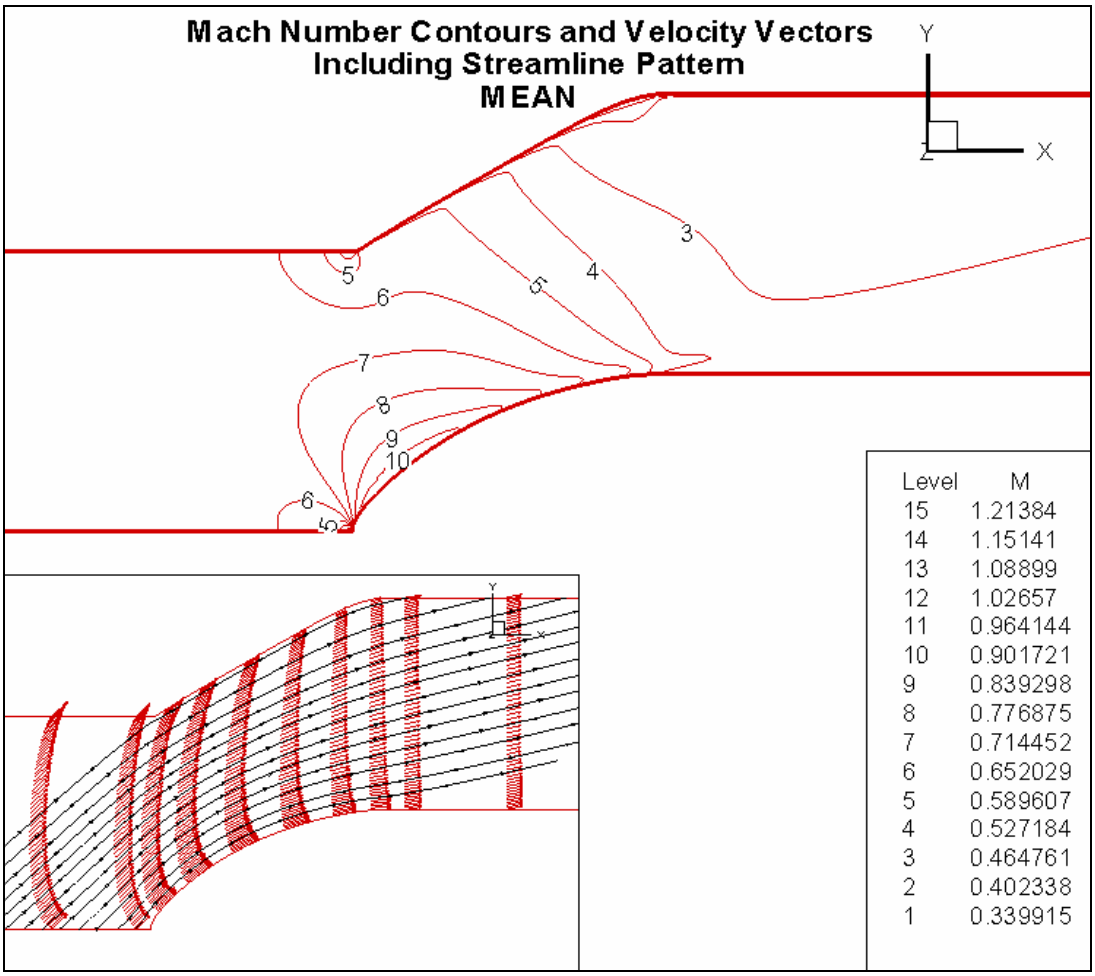

Figure 46 Results 2: Velocity vector field at mean line location.

The flow pattern at mean line region is as expected. The flow turning is 21.92° which is very close to the design value of 22.916°.

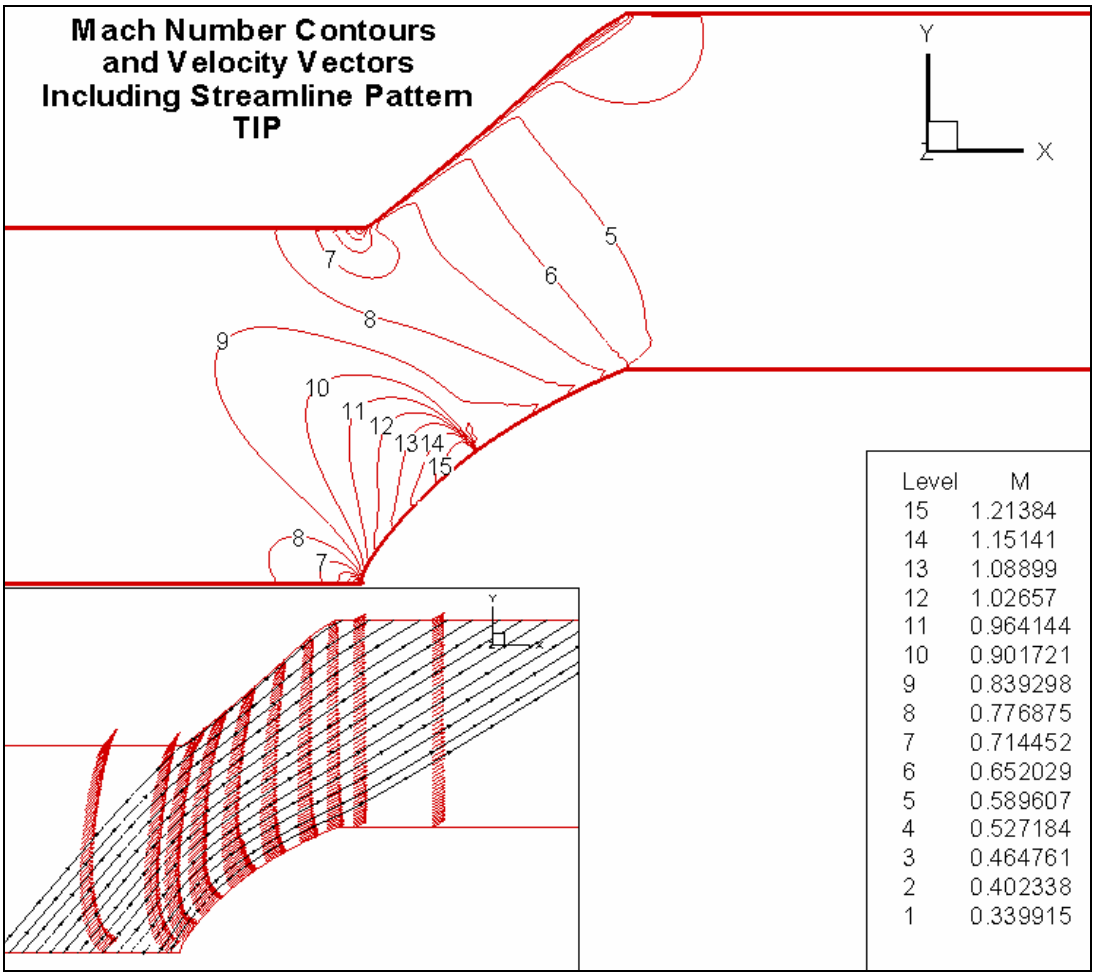

Figure 47 Result 3: Velocity vector field at tip location.

The flow pattern at tip region is as expected. The flow turning is 11.5° which is close to the design value of 9.97°.

In general, flow turning angles are estimated quite well.

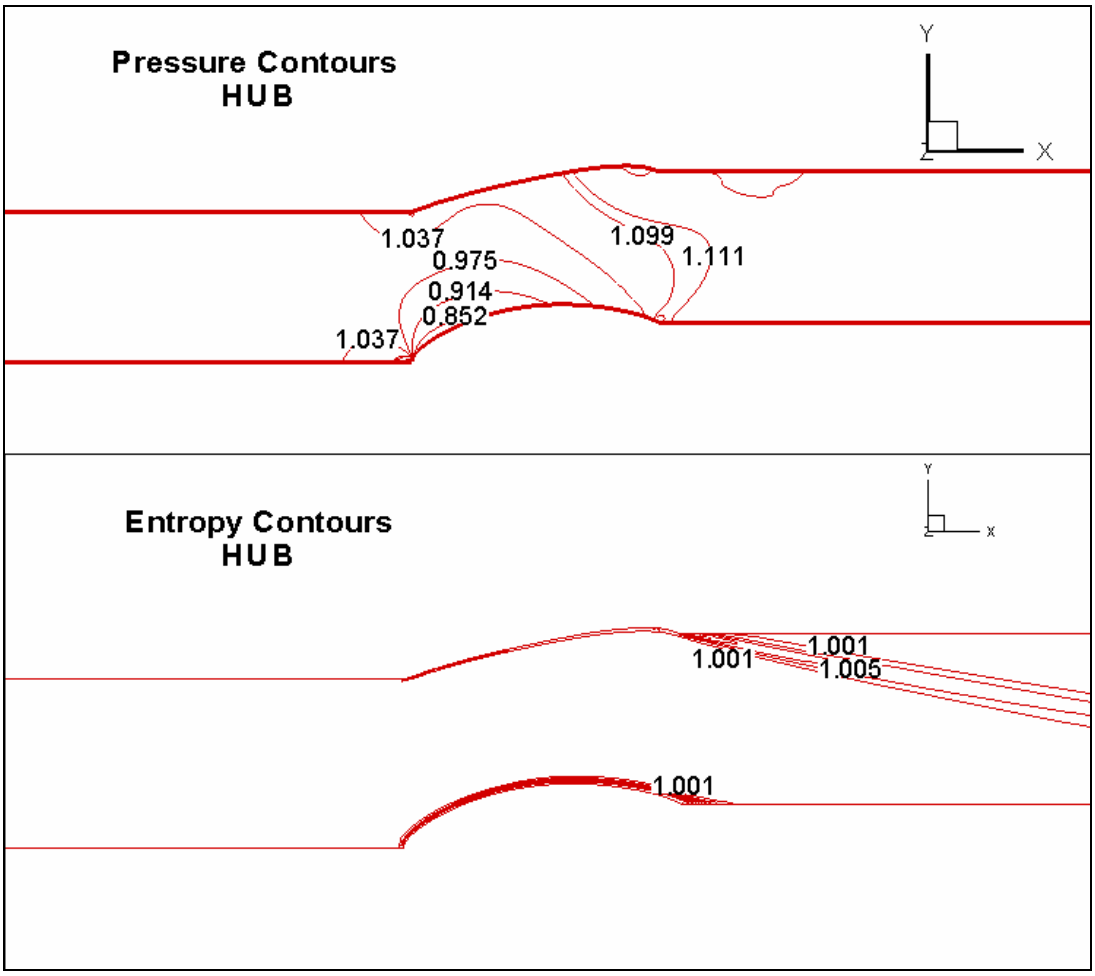

Figure 48 Result 4: Static pressure and entropy contours at hub location.

The static pressure is rising at hub region as expected. The static pressure ratio is around 1.111 which is slightly over the design value of 1.0986. The entropy field shows that very small amount of entropy is generated in the wake region.

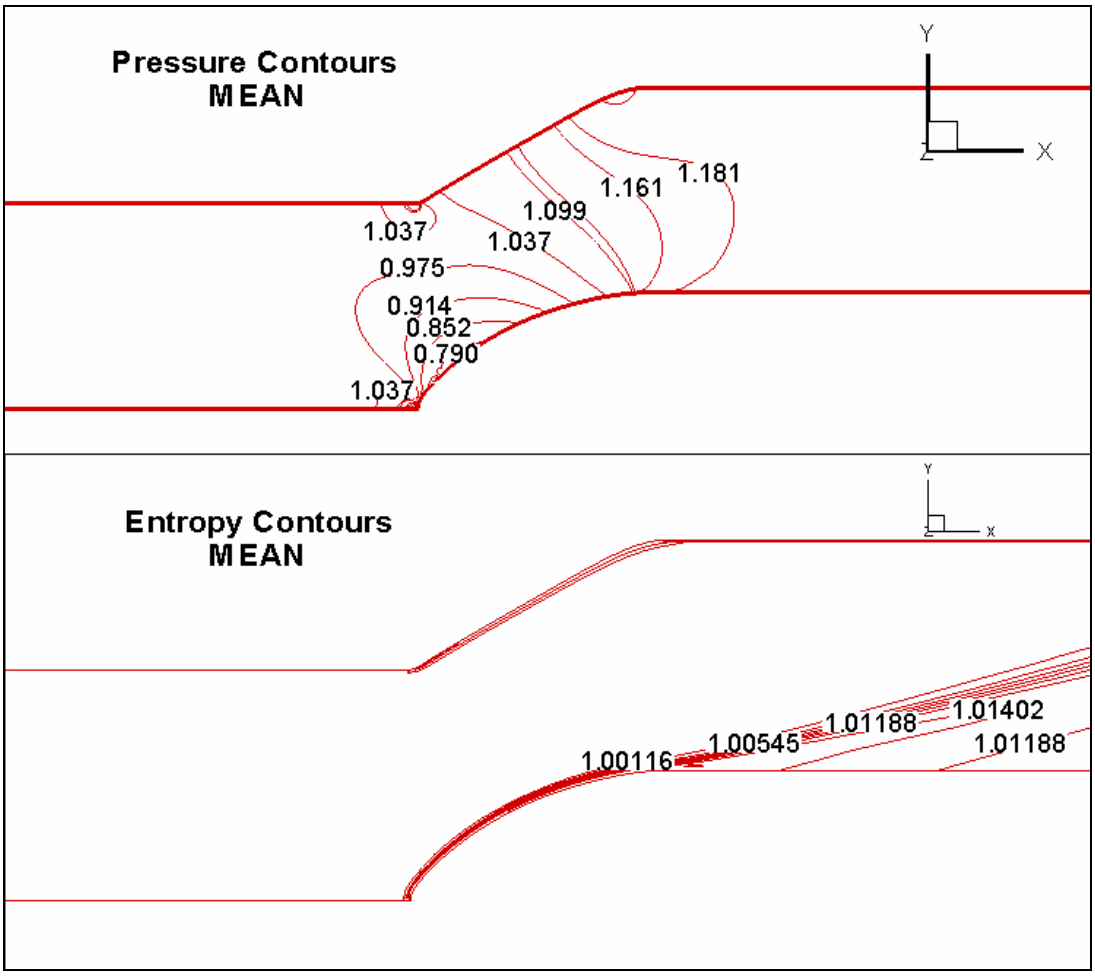

Figure 49 Result 5: Static pressure and entropy contours at mean line location.

The static pressure is rising at hub region as expected. The static pressure ratio is 1.181 which is slightly over the design value of 1.1662. The entropy field shows that relatively small amount of entropy is generated in the wake region.

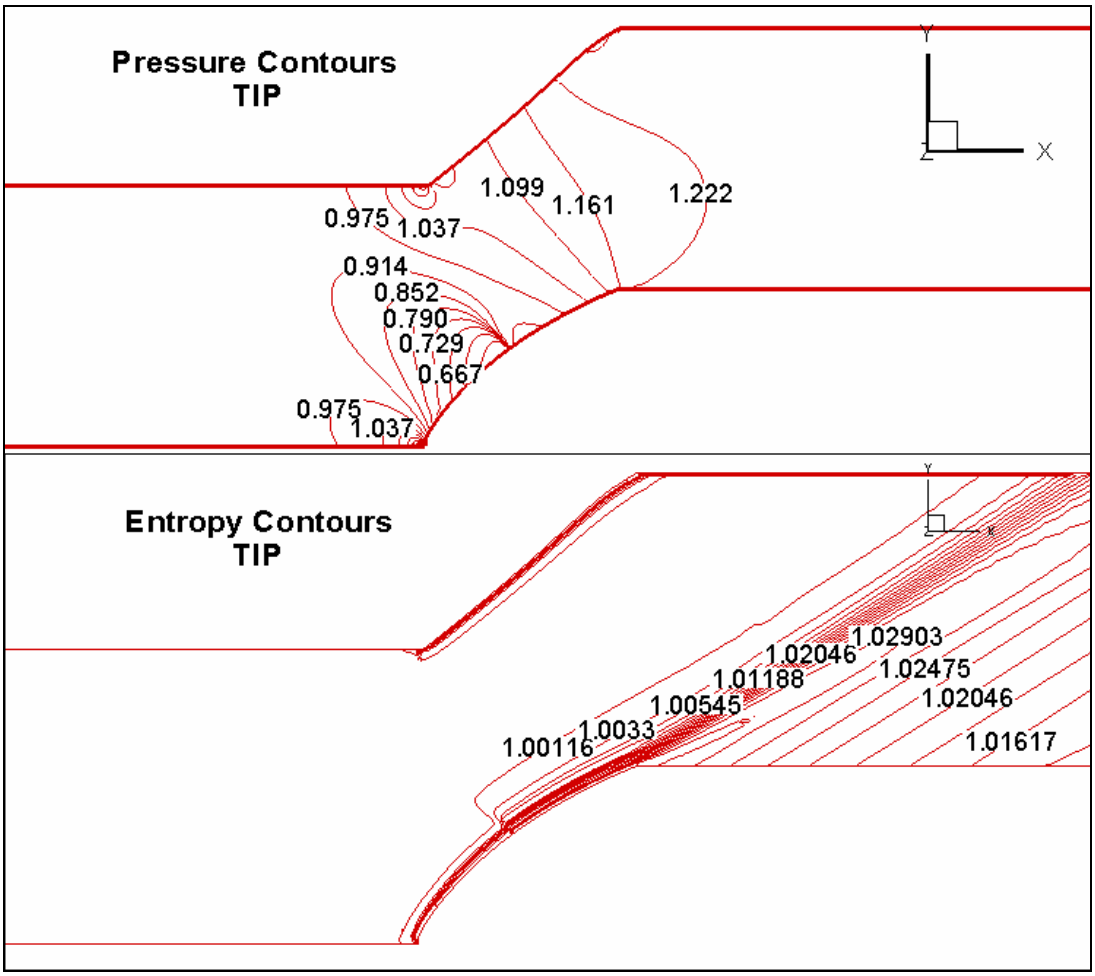

Figure 50 Result 6: Static pressure and entropy contours at tip location.

The static pressure is rising at hub region as expected. The static pressure ratio is 1.222 which is moderately over the design value of 1.1861. this may be because of the shock forming. It's known that static pressure increases after any normal shock. The entropy field shows that moderate amount of entropy is generated after the shock formation and in the wake region.

In general, static pressure rises are estimated slightly over the design values.

5.3.3 Comparison of Results with Design Conditions

Given below are the comparisons of the CFD analysis with design conditions. Two important parameters are compared in figures 51 and 52. These are flow turning (i.e. $\beta_1 - \beta_0$) and static pressure ratio (P_1/P_0).

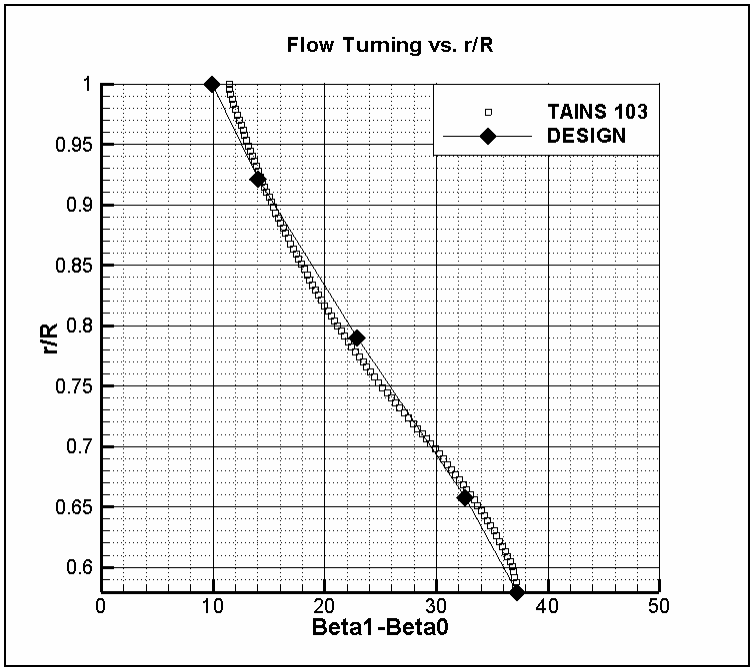

Figure 51 Comparison of flow turning angles.

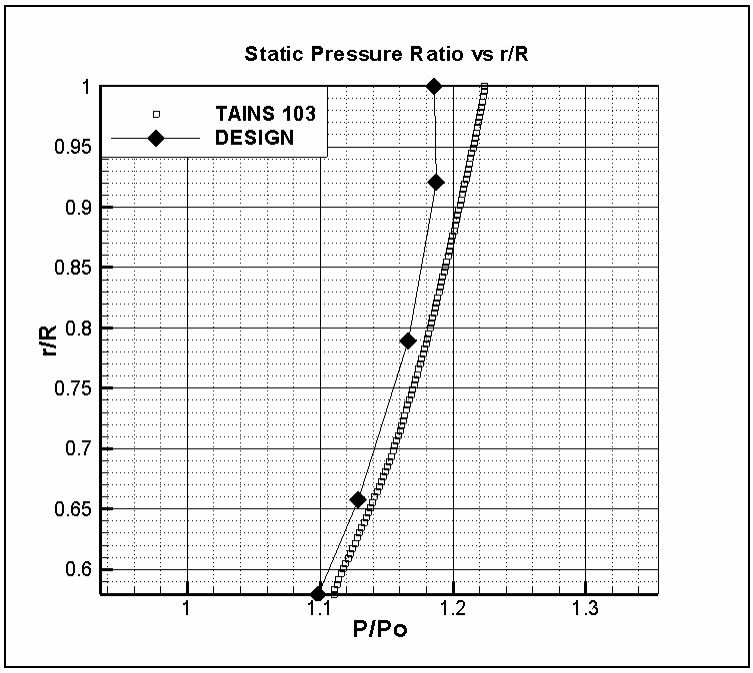

Figure 52 Comparison of static pressure ratio.

5.3.4 Convergence and Computational Time

All of the solutions mentioned above are converged ones. Convergence meaning that the solution reaching a final state in which the values of variables between each time step and one step before are minimal. Convergence criterion for the present study was to have the average of these differences (i.e. residuals) to be three orders of magnitude lower than the initial value.

The convergence histories of the solutions mentioned above are given below in figures 53 to 58.

The computational time needed for these solutions were given at the end in Table 11 including the computer configurations used.

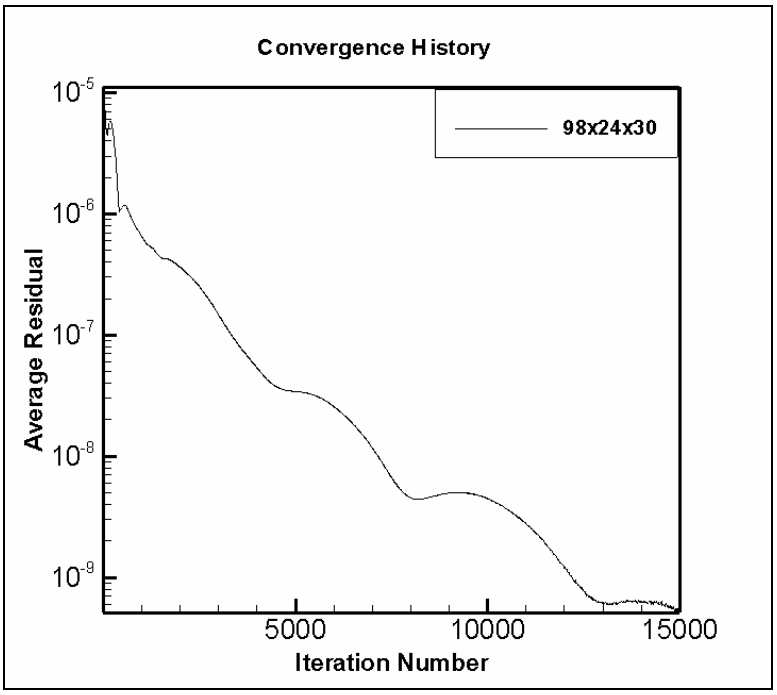

Figure 53 Convergence history of the 98x24x30 grid.

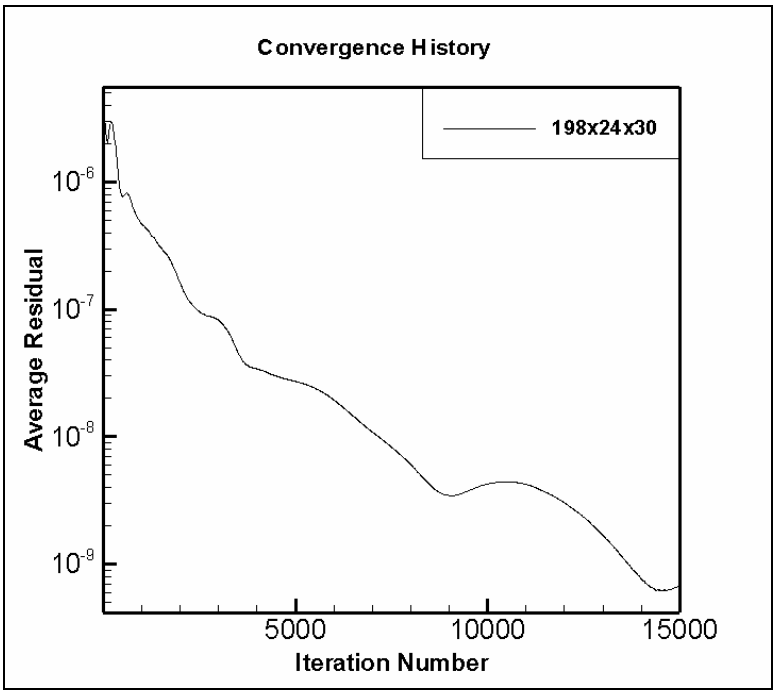

Figure 54 Convergence history of the 198x24x30 grid.

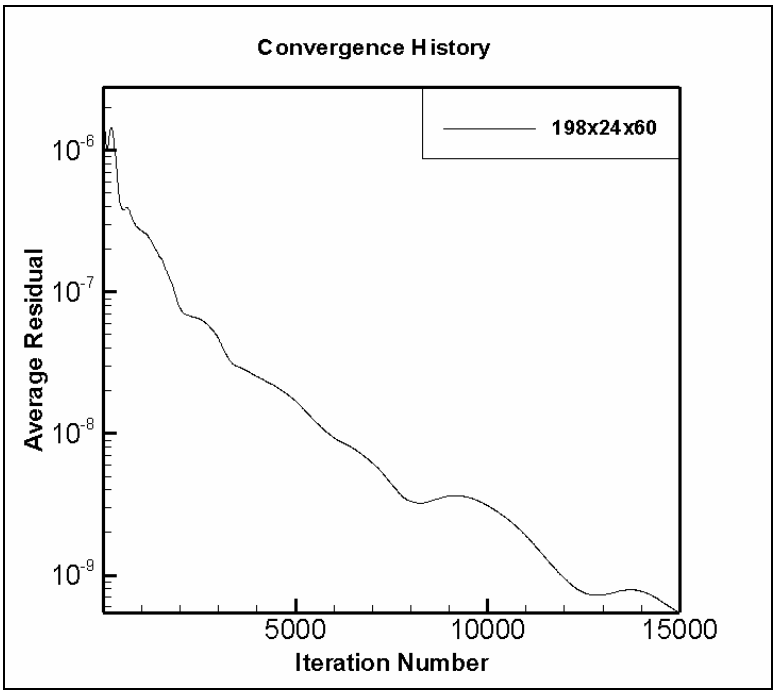

Figure 55 Convergence history of the 198x24x60 grid.

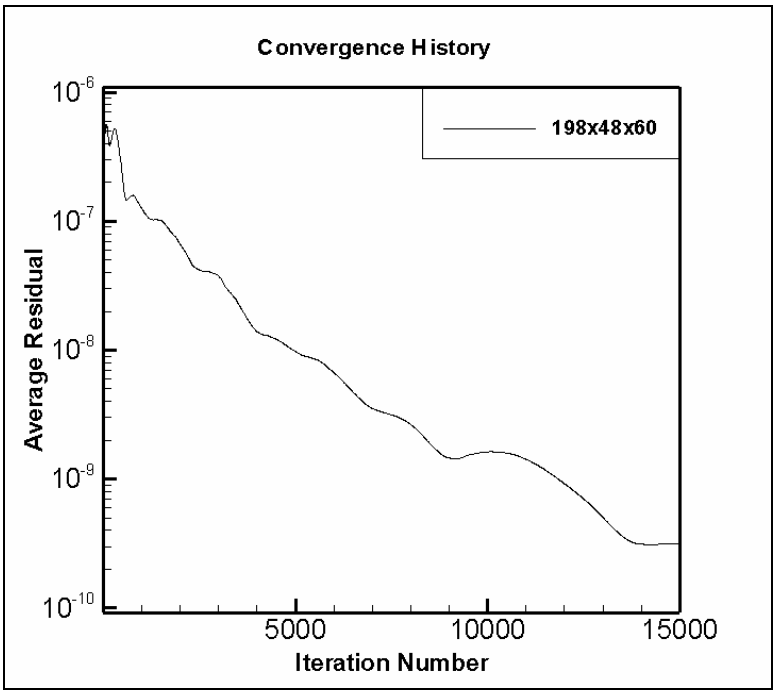

Figure 56 Convergence history of the 198x48x60 grid.

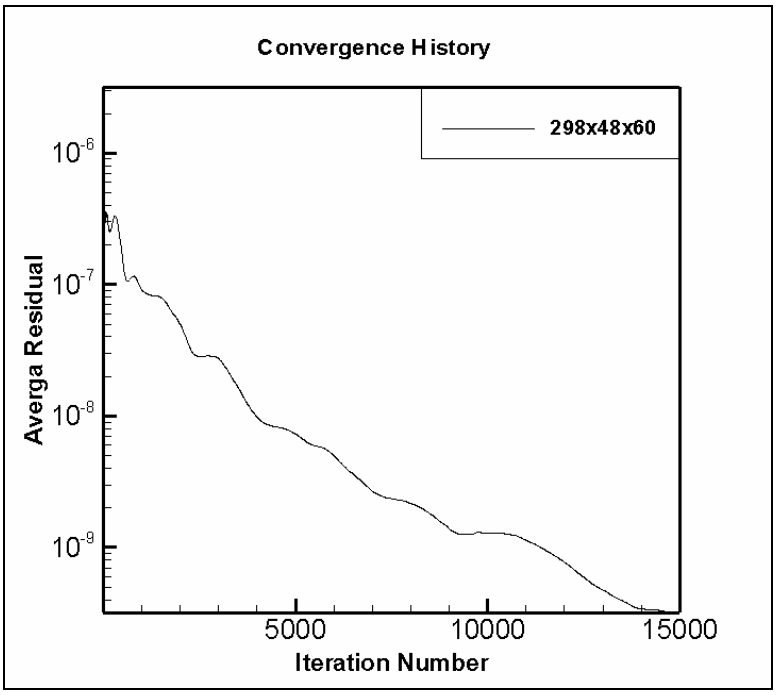

Figure 57 Convergence history of the 298x48x60 grid.

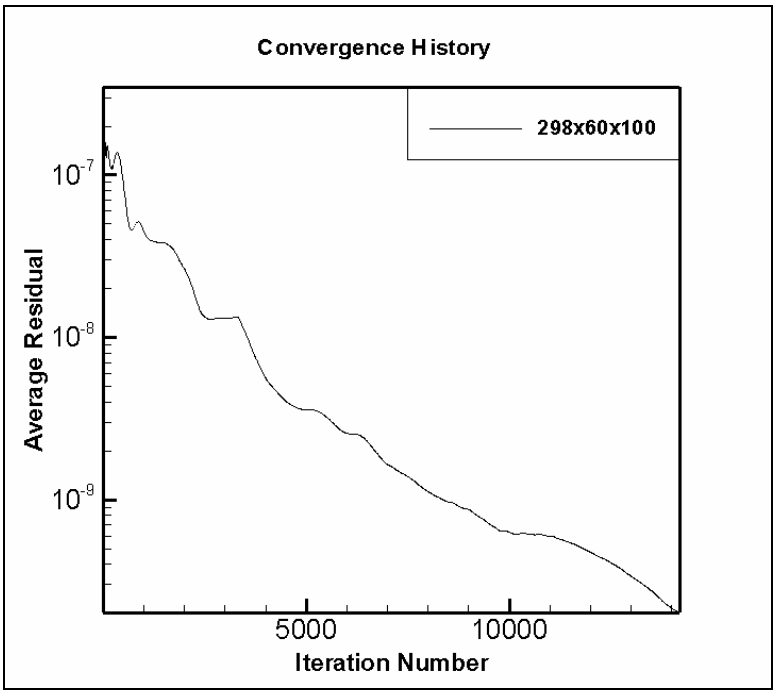

Figure 58 Convergence history of the 298x60x100 grid.

Table 11 Computational time of the six solutions mentioned above.

Grid Size	Node Number	Iteration	Comp. Time	Processor	Memory
98x24x30	70560	15000	2h 19min	P4 – 2.8Ghz	256 MB
198x24x30	142560	15000	4h 48min	P4 – 2.8Ghz	256 MB
198x24x60	285120	15000	9h 51min	P4 – 2.8Ghz	256 MB
198x48x60	570240	15000	20h 6min	P4 – 2.8Ghz	256 MB
298x48x60	858240	15000	30h 23min	P4 – 2.8Ghz	256 MB
298x60x100	1788000	14300	55h 20min	P4 – 3.2Ghz	1024 MB

The first five solutions are obtained on same type of computer configuration (i.e. PC with Pentium 4 2.8 Ghz processor, 256 MB RAM). However, the last one did not run on the same system, it needed higher computer resources (i.e. PC with Pentium 4 3.2 Ghz processor, 1 GB RAM).

The first five can be combined to see the effect of grid size on computational time. The result of such a comparison is given in Figure 59 below.

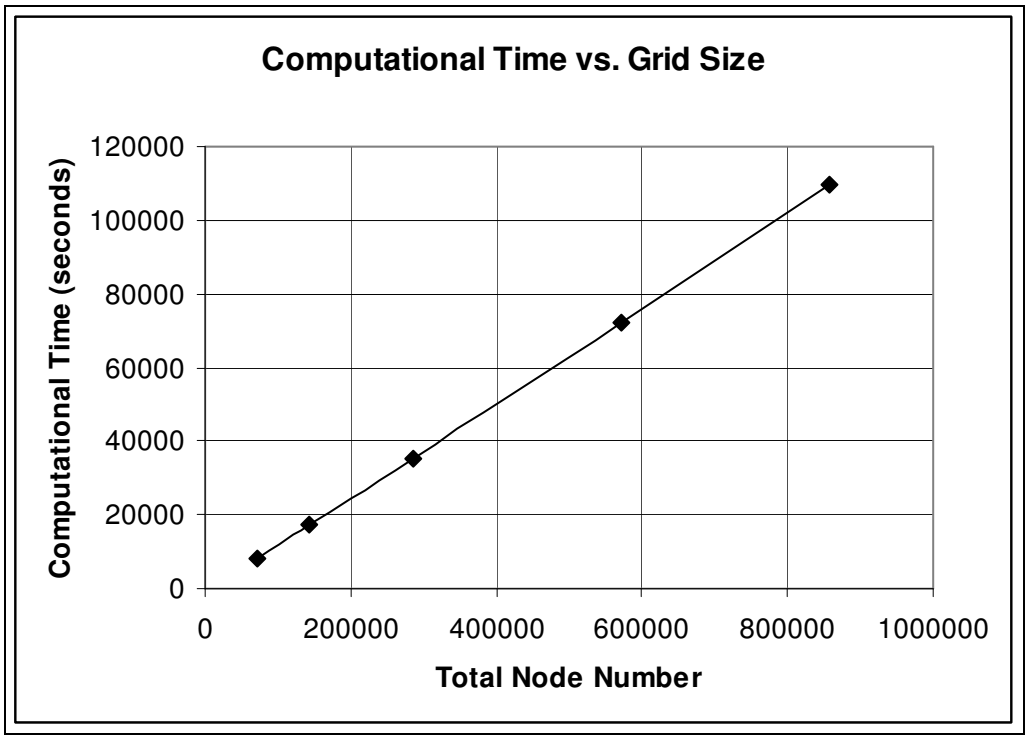

Figure 59 The effect of grid size on computational time.

CHAPTER 6

CONCLUSION AND RECOMMENDATIONS

Three-dimensional design and CFD analysis of a compressor rotor stage are performed.

This is done by starting with mean line analysis and through flow radial equilibrium. Radial equilibrium equation is satisfied at five radial locations.

Airfoils are selected and positioned using available data regarding the specific airfoil cascade family used in the present design.

Three-dimensional geometry is created by stacking airfoils using a three-dimensional computer aided design software.

Meanwhile, a three-dimensional internal flow solver is developed. This is done by modifying an existing three-dimensional solver. The solver is a multiblock, finite difference, approximately factored implicit Euler solver. In order to modify an external flow solver into an internal flow solver suitable for compressor/turbine rotor blades, three major advances were introduced: First was making use of the periodic boundary condition, second was making use of characteristics based inlet/outlet boundary conditions and the last one was the inclusion of the source terms due to rotating motion into momentum and energy equations.

Then, the results of the design study were combined with the results of the three-dimensional solver development study. Structured grids were generated around the geometry using a three-dimensional structured grid generator.

The results are obtained and compared with the design study. All the solutions converged and none had separation. The only point that is not expected was the shock formation on the suction side of the tip region. This can be overcome by changing the airfoil used in the tip region. There are other airfoils with less camber and able to provide the same flow turning.

According to the problems experienced throughout this study, some recommendations from a designer's point of view and possible future applications of the present study are stated below.

Radial equilibrium calculations are performed by hand. This is not impossible however it takes a long time to re-iterate on the design procedure. In the present study three design iterations are performed. Together with airfoil selection and other calculations regarding the airfoils, one design cycle takes about 2½ to 3 weeks. A computer program performing these calculations would have increased the speed of design iterations a lot.

Another problematic point was the grid generation. In the present study the grids are generated using three different computer programs. One to generate selected airfoil geometry in two-dimensions; one to create the three-dimensional geometry and one to generate the structured grid around the geometry created with the CAD software. Performing these required the knowledge of both CAD and grid generation programs. After acquiring a certain level of knowledge in these two programs, the grid generation may be done in one and a half days starting from scratch.

This could be overcome by writing a three-dimensional structured grid generator suitable for turbomachinery applications. Despite it sounds very hard, it is not impossible because the suction and pressure surfaces are similar in shape and dimensions. Moreover, the periodic boundaries used must be exactly the same in shape and dimensions. These make it possible to fill the volume lying between the two side boundaries with points.

Moreover if his grid generator is made parametric, then three-dimensional optimizations may be possible. Changing the setting angles of the selected airfoils or even changing the geometry of the airfoils and then creating the grid would then be very fast. The only limiting factor would then be the speed of the solver.

Even a genetic algorithm optimization would be possible together with parallelization of the solver. One of the reasons why an in-house code used is that the code is planned to be parallelized in the future. This will enable researchers to perform 3D genetic optimization on turbomachinery.

APPENDIX A

EXAMPLE DESIGN CALCULATIONS

A.1 Introduction

In this appendix, the detailed calculations of the design method described in Chapter 2 are given. In order to avoid duplication not all of the equations are re-written here. However, the necessary equations are repeated for reminding purposes.

A.2 Mean Radius

Mean radius is both the starting point and the input of the design process. As stated in Chapter 2 dimensions like hub and tip diameters are chosen to be similar to an already existing engine in the present study. Once the whirl speed is also chosen, the rotational velocity at each and every section is fixed. Selection of the whirl speed depends on the design specifications. In the present study, the whirl speed and the dimensions are chosen as follows:

Whirl Speed=14000 RPM (Revolution per Minute)

r_{hub}=0.11 m, r_{tip}=0.19 m, r_{mean}=0.15 m

The reason why these values are taken is in order to stay in high-subsonic regime even at the tip radius.

Another input is the initial axial and tangential velocities given to the flow by an inlet guide vane (IGV) before the flow enters the rotor stage. By doing so, the velocities at the inlet are fixed at mean radius.

INLET

$V_{ax,0}$=170 m/s (input), $V_{\theta,0}$=61.8749 m/s (20° IGV)

$$V_0 = \sqrt{{V_{ax,0}}^2 + {V_{\theta,0}}^2} \Rightarrow V_0=180.9102 \text{ m/s},\ \alpha_0 = \tan^{-1}\left(\frac{V_{ax,0}}{V_{\theta,0}}\right) \Rightarrow \alpha_0=70°$$

$$W_0 = \sqrt{{V_{ax,0}}^2 + (\omega r - V_{\theta,0})^2} \Rightarrow W_0=232.1 \text{ m/s},\ \beta_0 = \tan^{-1}\left(\frac{V_{ax,0}}{\omega r - V_{\theta,0}}\right) \Rightarrow \beta_0=47.1°$$

Having determined the absolute and relative velocity vectors and flow angles the inlet condition at the mean radius is fixed.

The next step is to evaluate the velocities and angles at the exit. The exit is related to the inlet by the use of “Reaction Number”. At the mean radius a reaction number of 0.5 is taken because R_n=0.5 represents symmetric velocity triangles and a modern design (Akmandor, 2001).

EXIT

$V_{ax,1}$=170 m/s (input), ωr_m=219.9115 m/s

$$R_n = 1 - \frac{V_{\theta,0} + V_{\theta,1}}{2\omega r} \Rightarrow V_{\theta,1}=158.0366 \text{ m/s } (R_n=0.5)$$

$$V_1 = \sqrt{{V_{ax,1}}^2 + {V_{\theta,1}}^2} \Rightarrow V_1=232.1111 \text{ m/s},\ \alpha_1 = \tan^{-1}\left(\frac{V_{ax,1}}{V_{\theta,1}}\right) \Rightarrow \alpha_1=47.0886°$$

$$W_1 = \sqrt{{V_{ax,1}}^2 + (\omega r - V_{\theta,1})^2} \Rightarrow W_1=180.91 \text{ m/s},\ \beta_1 = \tan^{-1}\left(\frac{V_{ax,1}}{\omega r - V_{\theta,1}}\right) \Rightarrow \beta_1=70°$$

RESULTS

$\Delta\beta$=22.9114°, $\frac{W_1}{W_0}$=0.7794, ψ_m=-0.4373, ϕ_m=0.7730, R_n=0.5

A.3 Radial Equilibrium

Radial equilibrium is achieved using simple radial equilibrium equation:

$$\frac{1}{r^2}\frac{d}{dr}\left(r^2 V_\theta{}^2\right)+\frac{d}{dr}V_{ax}{}^2=0$$

Carmichael – Lewis tangential velocity distribution is used (Wilson D.G., 1984) in simple radial equilibrium equation:

$$V_{\theta,0}=a(r)^n-\frac{b}{r},V_{\theta,1}=a(r)^n+\frac{b}{r}$$

After manipulations described in Chapter 2 are applied, one can get the following equations to find tangential and axial velocity at any radial location:

$$V_{\theta,0}'=a'(r')^n-\frac{b'}{r'},V_{\theta,1}'=a'(r')^n+\frac{b'}{r'}$$

$$\left(\frac{V_{ax,0}'}{\phi_m}\right)^2=1+\left(\frac{n+1}{n}\right)\left[\frac{1-R_{n,m}'}{\phi_m}\right]\left\{\left[1-(r')^{2n}\right]+\left(\frac{n}{n-1}\right)\left[\frac{\psi_m}{1-R_{n,m}'}\right]\left[1-(r')^{n-1}\right]\right\}$$

$$\left(\frac{V_{ax,1}'}{\phi_m}\right)^2=1+\left(\frac{n+1}{n}\right)\left[\frac{1-R_{n,m}'}{\phi_m}\right]\left\{\left[1-(r')^{2n}\right]-\left(\frac{n}{n-1}\right)\left[\frac{\psi_m}{1-R_{n,m}'}\right]\left[1-(r')^{n-1}\right]\right\}$$

a' and b' can be found by applying the primed variables at mean radius:

$$R_{n,m}'=1-a'(r')^{n-1},-\frac{\psi_m}{2}=b'$$

Remembering at mean radius $R_n=R_n'=0.5$, r'=1 and ψ_m=-0.4373

$\Rightarrow$ a'=0.5 and b'=0.21865

A.3.1 Radial Location 1 (r=0.11 m, r'=0.733)

ωr=161.1684 m/s

RADIAL EQUILIBRIUM

$R_n' = 0.25 \Rightarrow$ n=-0.3073

$\left(\frac{V_{ax,0}'}{\phi_m}\right)^2 = 1.1563 \Rightarrow V_{ax,0}$=182.0022 m/s,

$\left(\frac{V_{ax,1}'}{\phi_m}\right)^2 = 1.4561 \Rightarrow V_{ax,1}$=205.1243 m/s

$V_{\theta,0}' = 0.2518 \Rightarrow V_{\theta,0}$=55.3828 m/s,

$V_{\theta,1}' = 0.8482 \Rightarrow V_{\theta,1}$=186.52 m/s

INLET

$V_0 = \sqrt{V_{ax,0}^2 + V_{\theta,0}^2} \Rightarrow V_0$=190.2421 m/s, $\alpha_0 = \tan^{-1}\left(\frac{V_{ax,0}}{V_{\theta,0}}\right) \Rightarrow \alpha_0$=73.0751°

$W_0 = \sqrt{V_{ax,0}^2 + (\omega r - V_{\theta,0})^2} \Rightarrow W_0$=210.51 m/s, $\beta_0 = \tan^{-1}\left(\frac{V_{ax,0}}{\omega r - V_{\theta,0}}\right) \Rightarrow \beta_0$=59.8°

EXIT

$V_1 = \sqrt{V_{ax,1}^2 + V_{\theta,1}^2} \Rightarrow V_1$=277.2466 m/s, $\alpha_1 = \tan^{-1}\left(\frac{V_{ax,1}}{V_{\theta,1}}\right) \Rightarrow \alpha_1$=47.7200°

$W_1 = \sqrt{V_{ax,1}^2 + (\omega r - V_{\theta,1})^2} \Rightarrow W_1$=206.68 m/s, $\beta_1 = \tan^{-1}\left(\frac{V_{ax,1}}{\omega r - V_{\theta,1}}\right) \Rightarrow \beta_1$=7.04°

RESULTS

$\Delta\beta$ = 37.2119°, $\frac{W_1}{W_0}$ = 0.9818, ψ = -0.4373, ϕ_0 = 1.1286, R_n = 0.0383

A.3.2 Radial Location 2 (r=0.125 m, r'=0.833)

ωr=183.2596 m/s

RADIAL EQUILIBRIUM

$R_n' = 0.3528 \Rightarrow$ n=-0.4154

$\left(\frac{V_{ax,0}'}{\phi_m}\right)^2 = 1.0800 \Rightarrow V_{ax,0}$=176.6639 m/s,

$\left(\frac{V_{ax,1}'}{\phi_m}\right)^2 = 1.2176 \Rightarrow V_{ax,1}$=187.5792 m/s

$V_{\theta,0}' = 0.2769 \Rightarrow V_{\theta,0}$=60.9065 m/s,

$V_{\theta,1}' = 0.8017 \Rightarrow V_{\theta,1}$=176.3072 m/s

INLET

$V_0 = \sqrt{V_{ax,0}^2 + V_{\theta,0}^2} \Rightarrow V_0$=186.8682 m/s, $\alpha_0 = \tan^{-1}\left(\frac{V_{ax,0}}{V_{\theta,0}}\right) \Rightarrow \alpha_0$=70.9779°

$W_0 = \sqrt{V_{ax,0}^2 + (\omega r - V_{\theta,0})^2} \Rightarrow W_0$=214.89 m/s, $\beta_0 = \tan^{-1}\left(\frac{V_{ax,0}}{\omega r - V_{\theta,0}}\right) \Rightarrow \beta_0$=55.2°

EXIT

$V_1 = \sqrt{V_{ax,1}^2 + V_{\theta,1}^2} \Rightarrow V_1$=257.4300 m/s, $\alpha_1 = \tan^{-1}\left(\frac{V_{ax,1}}{V_{\theta,1}}\right) \Rightarrow \alpha_1$=46.7743°

$W_1 = \sqrt{V_{ax,1}^2 + (\omega r - V_{\theta,1})^2} \Rightarrow W_1$=187.70 m/s, $\beta_1 = \tan^{-1}\left(\frac{V_{ax,1}}{\omega r - V_{\theta,1}}\right) \Rightarrow \beta_1$=87.8°

RESULTS

Δβ=32.5829°, $\frac{W_1}{W_0}$=0.8735, ψ = -0.6297, ϕ_0=0.964, R_n=0.2588

A.3.3 Radial Location 4 (r=0.175 m, r'=1.166)

ωr=256.5634 m/s

RADIAL EQUILIBRIUM

$R_n' = 0.5970 \Rightarrow$ n=-0.3997

$\left(\frac{V_{ax,0}'}{\phi_m}\right)^2 = 0.9345 \Rightarrow V_{ax,0}$=164.3309 m/s,

$\left(\frac{V_{ax,1}'}{\phi_m}\right)^2 = 0.8403 \Rightarrow V_{ax,1}$=155.8289 m/s

$V_{\theta,0}' = 0.2827 \Rightarrow V_{\theta,0}$=62.1709 m/s,

$V_{\theta,1}' = 0.6575 \Rightarrow V_{\theta,1}$=144.6000 m/s

INLET

$V_0 = \sqrt{V_{ax,0}^2 + V_{\theta,0}^2} \Rightarrow V_0$=175.6982 m/s, $\alpha_0 = \tan^{-1}\left(\frac{V_{ax,0}}{V_{\theta,0}}\right) \Rightarrow \alpha_0$=69.2769°

$W_0 = \sqrt{V_{ax,0}^2 + (\omega r - V_{\theta,0})^2} \Rightarrow W_0$=254.54 m/s, $\beta_0 = \tan^{-1}\left(\frac{V_{ax,0}}{\omega r - V_{\theta,0}}\right) \Rightarrow \beta_0$=40.2°

EXIT

$V_1 = \sqrt{V_{ax,1}^2 + V_{\theta,1}^2} \Rightarrow V_1$=212.5836 m/s, $\alpha_1 = \tan^{-1}\left(\frac{V_{ax,1}}{V_{\theta,1}}\right) \Rightarrow \alpha_1$=47.1405°

$W_1 = \sqrt{V_{ax,1}^2 + (\omega r - V_{\theta,1})^2} \Rightarrow W_1$=191.88 m/s, $\beta_1 = \tan^{-1}\left(\frac{V_{ax,1}}{\omega r - V_{\theta,1}}\right) \Rightarrow \beta_1$=54.3°

RESULTS

Δβ=14.0929°, $\frac{W_1}{W_0}$=0.7538, ψ = -0.3213, ϕ_0=0.6405, R_n=0.6614

A.3.4 Radial Location 5 (r=0.19 m, r'=1.266)

ωr=278.5546 m/s

RADIAL EQUILIBRIUM

$R_n' = 0.6426 \Rightarrow$ n=-0.41996

$\left(\frac{V_{ax,0}'}{\phi_m}\right)^2 = 0.9050 \Rightarrow V_{ax,0}$=161.7135 m/s,

$\left(\frac{V_{ax,1}'}{\phi_m}\right)^2 = 0.7732 \Rightarrow V_{ax,1}$=149.4806 m/s

$V_{\theta,0}' = 0.2801 \Rightarrow V_{\theta,0}$=61.6036 m/s,

$V_{\theta,1}' = 0.6254 \Rightarrow V_{\theta,1}$=137.5251 m/s

INLET

$V_0 = \sqrt{V_{ax,0}^2 + V_{\theta,0}^2} \Rightarrow V_0$=173.0498 m/s, $\alpha_0 = \tan^{-1}\left(\frac{V_{ax,0}}{V_{\theta,0}}\right) \Rightarrow \alpha_0$=69.1460°

$W_0 = \sqrt{V_{ax,0}^2 + (\omega r - V_{\theta,0})^2} \Rightarrow W_0$=270.59 m/s, $\beta_0 = \tan^{-1}\left(\frac{V_{ax,0}}{\omega r - V_{\theta,0}}\right) \Rightarrow \beta_0$=36.7°

EXIT

$V_1 = \sqrt{V_{ax,1}^2 + V_{\theta,1}^2} \Rightarrow V_1$=203.1197 m/s, $\alpha_1 = \tan^{-1}\left(\frac{V_{ax,1}}{V_{\theta,1}}\right) \Rightarrow \alpha_1$=47.3853°

$W_1 = \sqrt{V_{ax,1}^2 + (\omega r - V_{\theta,1})^2} \Rightarrow W_1$=205.50 m/s, $\beta_1 = \tan^{-1}\left(\frac{V_{ax,1}}{\omega r - V_{\theta,1}}\right) \Rightarrow \beta_1$=46.6°

RESULTS

Δβ=9.9658°, $\frac{W_1}{W_0}$=0.7595, ψ = -0.2725, ϕ_0=0.5805, R_n=0.7326

A.4 All Results Together

All the results obtained so far are tabulated in Table 12 and Table 13 below:

Table 12 Velocity components and flow angles at five radial locations.

r(m)	$V_{ax,0}$ (m/s)	$V_{\theta,0}$ (m/s)	V_0 (m/s)	W_0 (m/s)	α_0 (°)	β_0 (°)
0.11	182.00	55.38	190.24	210.51	73.07	59.83
0.125	176.66	60.91	186.87	214.90	70.98	55.29
0.15	170	61.87	180.91	232.11	70	47.09
0.175	164.33	62.17	175.70	254.55	69.28	40.21
0.19	161.71	61.60	173.05	270.59	69.15	36.70
r(m)	**$V_{ax,1}$ (m/s)**	**$V_{\theta,1}$ (m/s)**	**V_1 (m/s)**	**W_1 (m/s)**	**α_1 (°)**	**β_1 (°)**
0.11	205.12	186.52	277.25	206.68	47.72	97.04
0.125	187.58	176.31	257.43	187.71	46.77	87.88
0.15	170	158.04	232.11	180.91	47.09	70
0.175	155.83	144.6	212.58	191.88	47.14	54.30
0.19	149.48	137.52	203.12	205.51	47.38	46.67

Table 13 Other important results at five radial locations.

r(m)	W_1/W_0	$\Delta\beta$	ψ	ϕ_0	ϕ_1	R_n	σ	DF
0.11	0.9818	37.21	-0.8132	1.1286	1.2719	0.0383	1.649	0.2078
0.125	0.8735	32.58	-0.6297	0.9640	1.0236	0.2588	1.451	0.3121
0.15	0.7794	22.91	-0.4373	0.7730	0.7730	0.5	1.210	0.3922
0.175	0.7538	14.09	-0.3213	0.6405	0.6074	0.6614	1.036	0.4023
0.19	0.7595	9.9658	-0.2725	0.5805	0.5366	0.7326	0.955	0.3879

A.5 Cascade Airfoil Selection

As stated in Chapter 2, NACA Mellor Charts are used to select appropriate airfoil cascades (Horlock J. H., 1958).

To do that, one needs the following:

i. Inlet flow angle α_1 (measured from axial direction).

ii. Exit flow angle α_2 (measured from axial direction).

iii. Solidity ($\sigma = \frac{spacing}{chord}$)

All inlet and exit flow angles and solidities are provided in Table 12. However one has to be careful because in the velocity triangles given above, all angles are measured from tangential direction.

Another important point to consider is that, the inlet and exit angles are β_0 and β_1 (i.e. relative flow angles) respectively for ROTOR geometries.

However are to be α_0 and α_1 (i.e. absolute flow angles) respectively for STATOR geometries.

Taking into account the two paragraphs above, one has to transform the results obtained to the ones in the form of Mellor charts. So:

i. Inlet flow angle $\alpha_1 = 90 - \beta_0$ (for rotor)

ii. Exit flow angle $\alpha_2 = 90 - \beta_1$ (for rotor)

iii. Solidity ($\sigma = \frac{spacing}{chord}$) is the same

Taking these into consideration, NACA Mellor charts are used and airfoil cascades are selected among suitable ones.

Given below are the results. In these results, $\alpha_1 - \gamma$ represents angle of attack and γ represents stagger angle. Both are measured from axial direction. So at the end, these must be converted back to present notation.

A.5.1 Radial Location 1 (r=0.11 m)

$\sigma = 1.649$, $\alpha_1 = 30.19°$, $\alpha_2 = -7.018°$

Suitable airfoil cascades:

65 – 12(10): $\sigma = 1.5$, $\alpha_1 - \gamma = 26° \Rightarrow \gamma = 4.19°$

65 – 15(10): $\sigma = 1.5$, $\alpha_1 - \gamma = 23° \Rightarrow \gamma = 7.19°$

65 – 18(10): $\sigma = 1.5$, $\alpha_1 - \gamma = 21° \Rightarrow \gamma = 9.19°$ ✓ This one is chosen.

A.5.2 Radial Location 2 (r=0.125 m)

$\sigma = 1.451$, $\alpha_1 = 34.71°$, $\alpha_2 = 2.123°$

Suitable airfoil cascades:

65 – 12(10): $\sigma = 1.5$, $\alpha_1 - \gamma = 22° \Rightarrow \gamma = 12.71°$

65 – 15(10): $\sigma = 1.5$, $\alpha_1 - \gamma = 20° \Rightarrow \gamma = 14.71°$ ✓ This one is chosen.

65 – 18(10): $\sigma = 1.5$, $\alpha_1 - \gamma = 18° \Rightarrow \gamma = 16.71°$

A.5.3 Mean Radius (r=0.15 m)

$\sigma = 1.21$, $\alpha_1 = 42.91°$, $\alpha_2 = 20°$

Suitable airfoil cascades:

65 – 12(10): $\sigma = 1.25$, $\alpha_1 - \gamma = 14° \Rightarrow \gamma = 28.91°$

65 – 15(10): $\sigma = 1.0$, $\alpha_1 - \gamma = 14° \Rightarrow \gamma = 28.91°$ ↴

65 – 15(10): $\sigma = 1.5$, $\alpha_1 - \gamma = 12° \Rightarrow \gamma = 26.91°$ ↥ Linear interpolation on σ.

$\Rightarrow \gamma = 27.91°$ ✓ This one is chosen.

65 – 18(10): × Out of range!

A.5.4 Radial Location 4 (r=0.175 m)

$\sigma = 1.036$, $\alpha_1 = 49.79°$, $\alpha_2 = 35.697°$

Suitable airfoil cascades:

65 – 8(10): $\sigma = 1.0$, $\alpha_1 - \gamma = 11° \Rightarrow \gamma = 38.79°$

65 – 12(10): $\sigma = 1.0$, $\alpha_1 - \gamma = 8° \Rightarrow \gamma = 35.79°$ ✓ This one is chosen.

65 – 15(10): × Out of range!

A.5.5 Radial Location 5 (r=0.19 m)

$\sigma = 0.955$, $\alpha_1 = 53.30°$, $\alpha_2 = 43.334°$

Suitable airfoil cascades:

65 – 4(10): $\sigma = 1.0$, $\alpha_1 - \gamma = 10° \Rightarrow \gamma = 43.30°$

65 – 8(10): $\sigma = 1.0$, $\alpha_1 - \gamma = 6° \Rightarrow \gamma = 39.30°$ ✓ This one is chosen.

65 – 12(10): × Out of range!

The results are converted to present notation and tabulated in Table 14 below:

Table 14 Cascade airfoil selection results at five radial locations.

r(m)	Airfoil	Angle of Attack	Stagger Angle (γ)	Δβ
0.11	NACA 65 – 18(10)	21°	80.81°	37.21°
0.125	NACA 65 – 15(10)	20°	75.29°	32.58°
0.15	NACA 65 – 15(10)	13°	62.09°	22.91°
0.175	NACA 65 – 12(10)	8°	54.21°	14.09°
0.19	NACA 65 – 8(10)	6°	50.70°	9.97°

APPENDIX B

AIRFOILS USED IN THE DESIGN

B.1 Introduction

In this appendix, all airfoils used in the present study are given. The airfoils are generated using the method described in Chapter 2. The accuracy of the generated airfoils are presented in Chapter 2 by a comparison on 65-(12)10 airfoil, so not repeated here. Airfoils are given directly.

B.2 Radial Location 1 (r=0.11 m, r'=0.733)

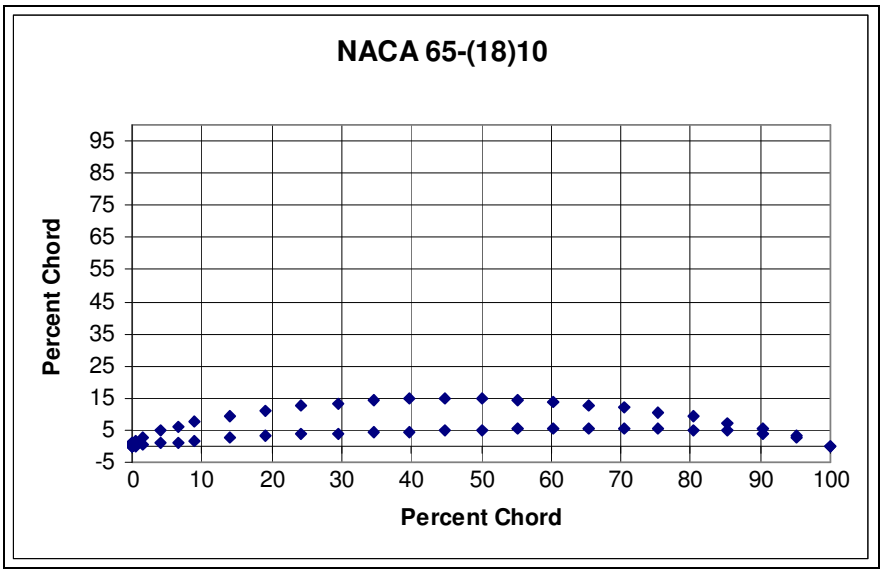

Figure 60 NACA 65-(18)10 airfoil coordinates.

B.3 Radial Location 2 (r=0.125 m, r'=0.833)

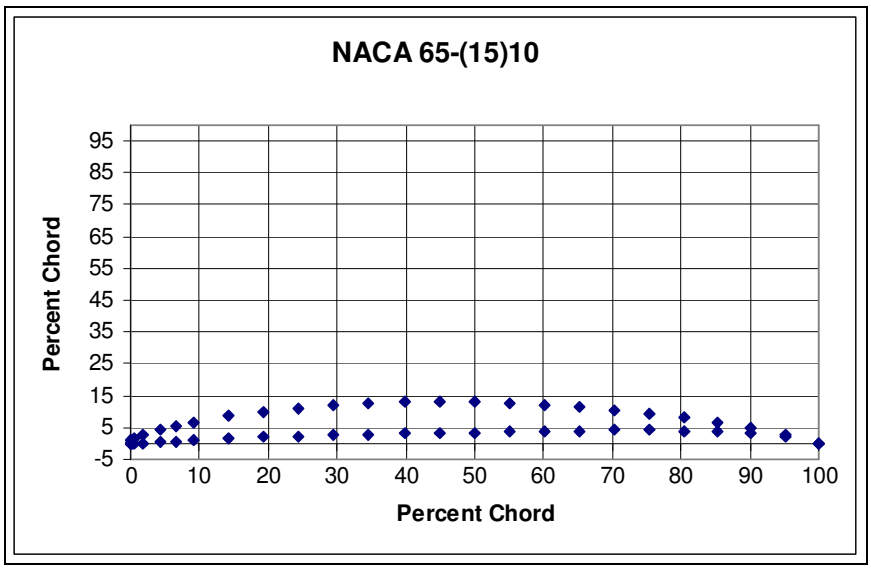

Figure 61 NACA 65-(15)10 airfoil coordinates.

B.4 Mean Radius (r=0.15 m, r'=1.0)

This section has the same airfoil with radial location 2.

B.5 Radial Location 4 (r=0.175 m, r'=1.166)

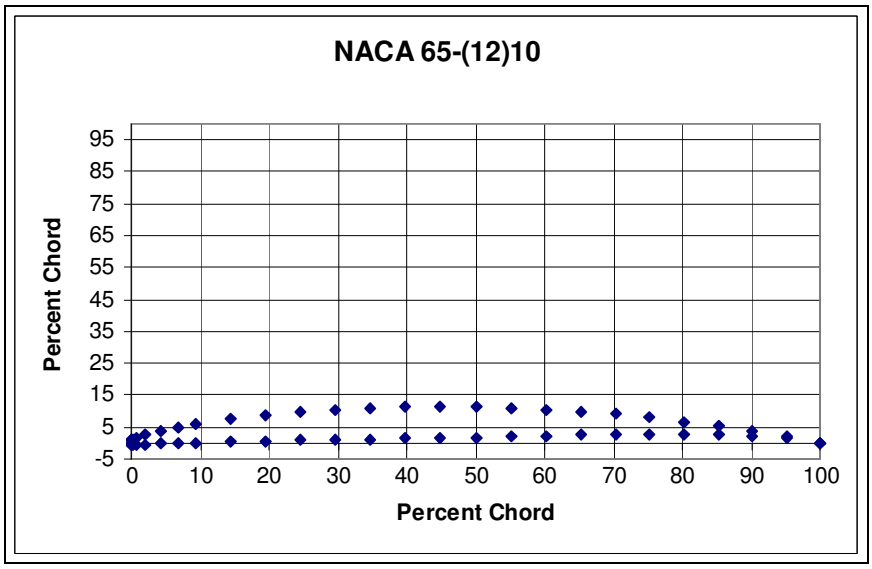

Figure 62 NACA 65-(12)10 airfoil coordinates.

B.6 Radial Location 5 (r=0.19 m, r'=1.266)

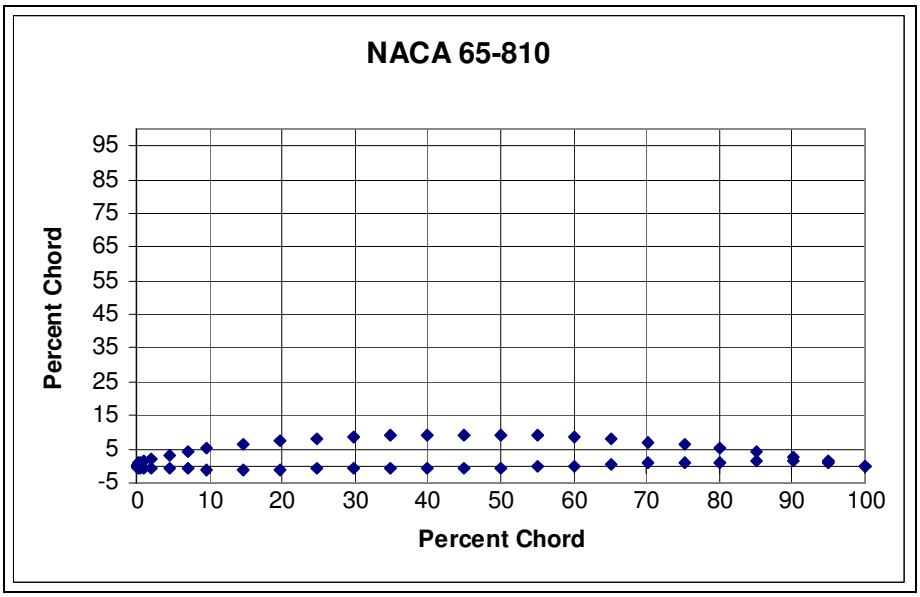

Figure 63 NACA 65-810 airfoil coordinates.

REFERENCES

Akmandor İ.S., "AE 435 Propulsion Systems II" Lecture Notes, Aerospace Engineering Department, METU, Fall 2001.

Aksel M.H., "Fluid Mechanics", Vol. 1, Department of Mechanical Engineering, METU, 2003.

Anderson Jr. J.D., "Fundamentals of Aerodynamics", McGraw-Hill Inc., Singapore, 1991.

Batchelor G.K., "An Introduction to Fluid Dynamics", Cambridge at the University Press, 1967.

Beam R.M., Warming R.F., "An Implicit Factored Scheme for the Compressible Navier-Stokes Equations" AIAA Journal, 16, 393, April 1978.

Bosman C., El-Shraawi M.A.I., "Quasi-Three-Dimensional Numerical Solution of Flow in Turbomachines", *ASME Transactions Journal of Fluids Engineering*, Vol. 99, pp. 132 – 140, 1977.

Bogdonoff S.M., Bogdonoff H.E., "Blade Design Data for Axial Flow Fans and Compressors" NACA Advance Confidential Report L5F07a, July 1945.

Cumpsty N.A., "Compressor Aerodynamics", Longman Scientific and Technical Group, Essex, 1989.

Çıray C., "AE 343 Aerodynamics II" Lecture Notes, Aerospace Engineering Department, METU, Fall 2000.

Davis W.R., Millar D.A.J., “A Comparison of the Matrix and Streamline curvature Methods of Axial Turbomachinery Analysis, from a Users Point of View”, *ASME Transactions Journal of Engineering and Power*, Vol. 97, pp. 549 – 560, 1975.

Denton J.D., “An Improved Time Marching Method for Turbomachinery Calculations”, ASME Paper 82-GT-239, 1982.

Denton J.D., “Designing in Three Dimensions”, AGARD-LS-195, May 1994.

Ekici K., “Quasi-Three Dimensional Analysis and Design of Turbomachinery Blades with Boundary Layer Coupling” M.Sc. Thesis, Department of Aeronautical Engineering, Middle East Technical University, June 1997.

Emery J.C., Herrig L.J., Erwin J.R., Felix A.R., “Systematic Two-Dimensional Cascade Tests of NACA 65-Series Compressor Blades at Low Speeds” NACA Report 1368, pp. 713 – 798, 1958.

Fujii K., “Practical Applications of New LU-ADI Scheme for the Three Dimensional Navier-Stokes Computation of Transonic Viscous Flows”, AIAA 24th Aerospace Sciences Meeting, Reno, Nevada, January 1986.

Grietzer E.M., Tan C.S., Graf M.B., “Internal Flow: Concepts and Applications” Cambridge University Press, Cambridge, 2004.

Hirsch Ch. “Numerical Computation of Internal and External Flows” Vol. 2, John Wiley and Sons, New York, 1990.

Hirsch Ch. Warzee G., “An Integrated Quasi-3D Finite Element Calculation Program for Turbomachinery Flows” *ASME Transactions Journal of Engineering for Power*, Vol. 101, pp. 141 – 148, 1979.

Holmes D.G., “Inviscid 3D Solution Methods”, von Karman Institute for Fluid Dynamics Lecture Series 1989-06, May 1989.

Horlock J.H., “Axial Flow Compressors”, Butterworths, London, UK, 1958.

Lewis R.I., “Turbomachinery Performance Analysis” Arnold Publishing, London, 1996.

Lieblein S., Schwenk F. C., Broderick R. L., “Diffusion Factor for Estimating Losses and Limiting Blade Loadings in Axial-Flow-Compressor Blade Elements”, NACA Research Memorandum , June 1953.

McDonald P., “The Computation of Transonic Flow through Two Dimensional Gas Turbine Cascades”, ASME Paper 71-GT-89, 1971.

Meauzé G., Hoorelbeke J., Gaillard R. “Test Case E/CA-3: High Subsonic Compressor Cascade 115” NATO AGARD AR 275, pp. 70 – 80, 1990.

Novak R.A., “Streamline Curvature Computing Procedures for Fluid Flow Problems”, *ASME Journal of Engineering for Power*, pp. 478 – 490, 1967.

Schmitt V., Charpin F. “Pressure Distributions on the ONERA-M6-Wing at Transonic Mach Numbers” NATO AGARD AR138 Appendix B. 1979.

Sergen Ş., Çete A.R., Ortakaya Y., “TİDEB3010088 3 Boyutlu Euler/Navier-Stokes Yapısal ve Yapısal Olmayan Akım Çözücüleri Geliştirilmesi” Projesi 2003 1. Altı Aylık Dönem Raporu Formu, TAI, 2003.

Smith D.J.L., “Computer Solution of Wu’s Equations for Compressible Flow through Turbomachines”, NASA SP-304, Part 1, 1974.

Smith L.H., “The Radial Equilibrium Equation of Turbomachinery”, *ASME Journal of Engineering for Power*, Vol. 88, pp. 1 – 12, 1966.

Steger J.L., Warming R. F., “Flux Vector Splitting of the Inviscid Gas Dynamics Equations with Application to Finite Difference Methods”, *Journal of Computational Physics*, Vol. 40, pp. 263-293, 1981.

Song B. “Experimental and Numerical Investigations of Optimized High-Turning Supercritical Compressor Blades” Ph.D. Thesis, Department of Mechanical Engineering, Virginia Polytechnic Institute and State University, November 2003.

Şen T.S., “Development of a Three Dimensional Multiblock Parallel Navier-Stokes Solver” Ph.D. Thesis, Department of Aeronautical Engineering, METU, November 2001.

Uzol O., “Quasi-Three Dimensional Numerical Design of Turbomachinery Blades”, M.Sc. Thesis, Department of Aeronautical Engineering, Middle East Technical University, July 1995.

Vuillez C., Petot B., “New Methods, New Methodology Advanced CFD in the SNECMA Turbomachinery Design Process”, AGARD-LS-195, May 1994.

Wallis R.A., “Axial Flow Fans and Ducts”, John Wiley and Sons, New York, 1983.

Wilson D.G., Korakianitis T., “The Design of High Efficiency Turbomachinery and Gas Turbines”, MIT Press, New Jersey, 1984.

Wu C.H., “A General Theory of Three Dimensional Flow in Subsonic and Supersonic Turbomachines of Axial, Radial and Mixed Flow Types”, *Transactions of the ASME*, pp. 1363 – 1380, 1952.